Autonomous Underwater Vehicle (AUV) Propulsion System Analysis and Optimization

James A. Schultz

Thesis submitted to the faculty of the
Virginia Polytechnic Institute and State University
in partial fulfillment of the requirements for the degree of

Master of Science
In
Aerospace and Ocean Engineering

Dr. Wayne L Neu
Dr. Daniel J Stilwell
Dr. Alan J Brown

May, 4, 2009

Blacksburg, Virginia

Keywords: AUV; propeller, Motor, Efficiency

Autonomous Underwater Vehicle (AUV)
Propulsion System Analysis and Optimization

James A. Schultz

Abstract

One of the largest design considerations for autonomous underwater vehicles (AUV's) that have specific mission scenarios is the propulsive efficiency. The propulsive efficiency affects the amount of power storage required to achieve a specific mission. As the efficiency increases the volume of energy being stored decreases. The decrease in volume allows for a smaller vehicle, which results in a vehicle that requires less thrust to attain a specific speed.

The process of selecting an efficient propulsive system becomes an iterative process between motor, propeller, and battery storage. Optimized propulsion systems for mission specific AUV's require costly motor and propeller fabrication which may not be available to the designer. Recent advancements in commercially available electric motors and propellers allows for cost effective propulsion systems. The design space selection of motors and propellers has recently increased due to component demand of remote control airplane and boats. The issue with such systems is how to predict small propeller and small motor performance interactions since remote control motor and propeller designers usually don't provide enough information about the performance of their product.

The mission statement is to design a propeller and motor combination that will allow an autonomous underwater vehicle to travel large distances while maintaining good efficiency. The vehicle will require 12 N of thrust with a forward velocity of 2 m/s. The propeller needs to be larger than 2.5" due to inflow velocity interaction and smaller than 4" due to loss of thrust when in surface transit due to suction.

Acknowledgements

I would sincerely like to thank my parents for helping me through school. I would have not been able to do it physically or financially without their years of support and love. They have been the wisest influence on me from the beginning to the end and continue to expect excellence in all areas of my life. I would also like to thank my advisor Dr. Neu for his countless hours of answering my questions with patience and attention that I may not have had when coming to him. I would also like to thank John Hennage for his friendship and wisdom in the areas of electronics, mechanics, and various other areas. I would also like to thank James Lambert and Bruce Stanger for making the parts that I requested and guiding me where needed. I would like to thank the committee who has helped to review my work and guide me through the years of again silly questions and much patience on their end. Not that this is the least important of my relationships, in fact it is the most important, but I would like to thank God and my church family for being there to support me and keep me from stumbling; of which I'm eternally grateful.

Table of Contents

Chapter 1 – Introduction 1
1.1 Previous Research 1
1.1 Motivation 1
1.2 Thesis Outline 1
Chapter 2 – Propeller Design 3
2.1 Propeller Sectioning 3
2.2 - Ideal Hydrodynamic Fluid Approach 4
2.3 - Experimental Approach 7
Chapter 3 – Propeller Testing Equipment 10
3.1 - Wind Tunnel 10
3.2 - Tunnel Instrumentation 12
3.3 – Propeller Test Rig and Propeller Test Stand 14
3.4 – Signal Generation, Manipulation and Acquisition 21
Chapter 4 – Propeller Analysis 28
4.1 – Propeller Selection Process 28
4.2 - Propeller Testing 33
4.3 – Jacobson Comparison 38
4.4 – Candidate propeller testing, Octura 0977 42
Chapter 5 – Motor Selection Guidelines 45
Chapter 6 – Motor testing setup 52
Chapter 7 – Motor Evaluation and Testing 54
7.1 – PWM performance prediction 55
7.2 – Motor Performance at full duty cycle 59
Chapter 8 – Optimization of Propeller and Motor combination 63
Chapter 9 – Conclusions and Future Work 65
9.1 - Results 65
9.2 - Future Work 65
Works Cited 66

Appendix A – Tabulated Small, Medium, and Large efficiency, diameter, P/D 68
Appendix B – Uncertainty Analysis of Propeller Testing 69
Appendix C – Expanded Blade Area of Octura 0977 and Octura 1462 74
Appendix D - Motor performance values as torque increases (Custom motor) 75
Appendix E – Motor performance values as torque increases (Hyperion Z2213-24) 76
Appendix F – Experimental and Empirical data from “custom” motor 76

List of Figures

Figure 2-1: Force and velocity vector illustration 3
Figure 2-2: Actuator disk control volume illustration 4
Figure 2-3: Axial pressure variation within the control volume 4
Figure 2-4: Velocity Profile along stream-tube 6
Figure 2-5: Ideal efficiency as a function of propeller loading 7
Figure 3-1: View of test section and return of the Instructional Tunnel [9] 10
Figure 3-2: Schematic of the Student 3-Foot Open Test Section Instructional Tunnel [9] 10
Figure 3-3: Pitot-static probe relative to propeller rig 11
Figure 3-4: Mean-velocity distribution across the empty test-section of the open-jet wind tunnel.[11] 12
Figure 3-5: Pitot-Static probe 12
Figure 3-6: Errors due to misalignment in velocity measurements made with a Pitot-static probe. [11] 13
Figure 3-7: Dwyer Series 475 Mark III Digital Manometer 13
Figure 3-8: Mechanism Ltd. Mk.2 precision aneroid barometer 14
Figure 3-9: Wind tunnel thermometer 14
Figure 3-10: Propeller test rig component illustration (side view) 15
Figure 3-11: Propeller test rig shaft to nose tolerance 16
Figure 3-12: Propeller test rig sealing 16
Figure 3-13: Propeller test rig and propeller test stand 17
Figure 3-14: Propeller test stand leveling 17
Figure 3-15: Honeywell, Model 31 Low, Low Range Precision Miniature Load Cell [15] 18
Figure 3-16: Propeller test rig load cell calibration process 18
Figure 3-17: Vibrac, Series I, TQ10, Torque Measuring Transducer schematic and picture [16] 19
Figure 3-18: Vibrac, Series I, TQ10, Torque Measuring Transducer calibration process 19
Figure 3-19: Hyperion 2213-24 BLDC motor [17] 20
Figure 3-20: Hyperion Titan 10A Motor Controller [17] 20
Figure 3-21: Signal Generation, Manipulation and Acquisition Architecture Schematic 21
Figure 3-22: LabVIEW front panel screenshot 22
Figure 3-23: LabVIEW block diagram screenshot 23
Figure 3-24: Wiring of DAQ box 24
Figure 3-25: Vibrac Motorized Dynamometer Instrument Model 1038 [16] 25
Figure 3-26: Sensotec In-Line Amplifier, model: Universal Bi-Polar (UBP) wiring 26
Figure 3-27: Sensotec In-Line Amplifier, model: Universal Bi-Polar (UBP) schematic [19] 26
Figure 4-1: Propeller Geometry (simplified) 28
Figure 4-2: OpenProp input screen 28
Figure 4-3: Chord to diameter ratios of small medium and large BAR's tested 29
Figure 4-4: Small Blade Area Ratio parametric efficiency output 30
Figure 4-5: Medium Blade Area Ratio parametric efficiency output 31
Figure 4-6: Large Blade Area Ratio parametric efficiency output 31
Figure 4-7: Efficiency vs. advance ratio for small, medium, and large BAR's 32
Figure 4-8: P/D vs. J for small, medium, and large BAR's 33

Figure 4-9: Dimensional Expanded Blade Area of Octura 1462 34
Figure 4-10: Dimensionless cord distribution of Octura 1462 35
Figure 4-11: Unrefined Octura 1462 propeller data 35
Figure 4-12: Torque sensor drift 36
Figure 4-13: Adjusted torque sensor drift 37
Figure 4-14: Regressed Octura 1462 propeller performance curves 38
Figure 4-15: Water tunnel testing of Octura 1462 [24] 39
Figure 4-16: Water-tunnel and Wind-tunnel propeller performance data 39
Figure 4-17: OpenProp single propeller design input screen 40
Figure 4-18: OpenProp optimized propeller geometry example 41
Figure 4-19: Dimensional Expanded Blade Area of Octura 0977 42
Figure 4-20: Dimensionless cord distribution of Octura 0977 43
Figure 4-21: Octura 0977 experimental propeller performance data 43
Figure 4-22: Regressed Octura 0977 Propeller Performance Curves 44
Figure 5-1: Inner and Outer Rotor Concept 46
Figure 5-2: Winding Terminations [27] 48
Figure 5-3: Winding Terminations (Electrically) 48
Figure 5-4: Tested wiring styles [27] 49
Figure 5-5: Winding Styles [27] 50
Figure 6-1: Motor Test Rig Setup 52
Figure 6-2: Hyperion E-meter [29] 53
Figure 7-1: DC motor torque/Speed curve[30] 55
Figure 7-2: RPM as a function of torque with varying Duty Cycle (Custom motor) 56
Figure 7-3: Current draw as torque on motor increases and PWN varies (Hyperion Z2213-24) 57
Figure 7-4: Efficiency of power input to motor, duty cycle dependent (Hyperion Z2213-24) 57
Figure 7-5: Efficiency of power input to motor, duty cycle dependent (Custom motor) 58
Figure 7-6: RPM as current increases (Experimental vs. Empirical of custom motor) 60
Figure 7-7: Torque as current increases (Experimental vs. Empirical of custom motor) 61
Figure 7-8: Efficiency as function of current for empirical, empirical including extra losses, and experimental (custom motor) 61

List of Tables

Table 1: OpenProp comparison to experimental data 41
Table 2: Comparison of Outer-Rotor and Inner-Rotor Motors [26] 45
Table 3: Inner-Rotor versus Outer-Rotor Motor Applications [26] 45
Table 4: Effects of Changing Number of Poles, Teeth, and Phases [26] 47
Table 5: Electric motor assumed efficiencies based on motor diameter [26] 47
Table 6: Proposed proportion of electric motor losses [26] 47
Table 7: Motor Constants of Motors Tested 54
Table 8: Motor Performance Characteristics 63
Table 9: RPM and Torque at maximum efficiency 63

Chapter 1 – Introduction

1.1 Previous Research

Research in the area of autonomous underwater vehicle (AUV) propulsive efficiency has been explored prior to the writing of this thesis.

Reader [1] explores the different types of propulsion systems used throughout the years of AUV development. The article deals with propulsion systems from an energy utilization standpoint. This article can be used to help guide a designer through the years of AUV development and see the designs of previous propulsion systems. Specifically this paper deals with propulsion design and power storage of AUV's and their predecessors.

Poole [2] investigates the propulsion system of AUV's from a systems approach. This paper identifies the parameters of various components and relates them through analytical modeling. This paper's emphasizes is on electric motors and screw propellers, similar to the approach taken in this paper.

A detailed study of how to select autonomous underwater vehicle energy systems depending on a specific mission can be found in Hawley [3]. This analysis is a bit outside the concepts of this paper, but gives a useful mission scenario style approach to designing an AUV propulsion system.

Standway and Stefanov-Wagner [4] explain how to optimize a small-diameter ducted propeller system for a remotely operated vehicle (ROV) that has to handle a large payload. A parametric study based on mission specific guidelines was done to evaluate the relative geometry of the propeller. The candidate custom fabricated propeller was fabricated, tested, and evaluated. A similar approach is taken in this thesis, except the propellers in this thesis are limited to commercial of the shelf components.

1.1 Motivation

A need to develop a mission specific propulsion system for Virginia Tech's 4.75 AUV research arose and this paper is a result of that need. A preliminary design of the propulsion system proved to be useful and capable of performing the tasks desired, but the efficiency of this vehicle was in question.

The process of selecting a motor and propeller combination can prove frustrating at times and tedious at best. The purpose of this report is to allow a designer to see more clearly the selection process of a specific propulsion system and the options available to gain an efficient propulsion system. The scope of this thesis does not encompass all of the aspects of propulsive efficiency, but contains many guidelines for propulsion component selection in the areas of motor and propeller optimization. The analysis of this report is also not new; it is merely retracing the steps of propeller and motor pairing for more modern propulsion systems.

1.2 Thesis Outline

The outline of this thesis is structured to help develop guidelines and methods for selecting an efficient AUV propulsion system using commercially available components. Theoretical propeller

performance is analyzed to give guidelines for propeller selection. After propeller selection is made, experimental testing of the selected propeller is conducted to evaluate the effectiveness of theoretical propeller selection and the effectiveness of meeting the mission statement. The next phase of propulsion system analysis is motor selection. Selection guidelines are developed to aid in the selection of a motor for optimum efficiency. These efficiency guidelines are used to select a series of motors that are commercially available. These motors are then tested and evaluated to help predict other commercially available motors that might meet the requirements of the propeller. Using the propeller requirements and estimated motor performance, a propeller and motor combination is evaluated to see the effectiveness of the propulsive pair. Results of propeller and motor analysis lead to the suggested design of a custom motor or reduction gear.

Chapter 2 – Propeller Design

One major objective of this thesis is to develop guidelines for selecting a commercially available propeller with good efficiency that will meet the requirements set forth by the mission statement. To help guide in the propeller selection process this chapter will go through some fundamental principles in propeller force interaction, geometry, fluid dynamics, and propeller regression analysis. One useful principle for high efficiency is a large diameter and slow spinning propeller.

2.1 Propeller Sectioning

Propellers are usually designed with a complex geometry that changes along the blades radius. This complex geometry can be broken into multiple smaller sections starting at the root and ending at the tip of the propeller. Each section can be varied to optimize the lift required at that incremental section. The number of sections along the blade is dependent on how detailed the designer wishes to investigate. A force interaction diagram helps to understand the fundamentals of a propeller section. The fundamental force vectors and their respective angles can be seen below:

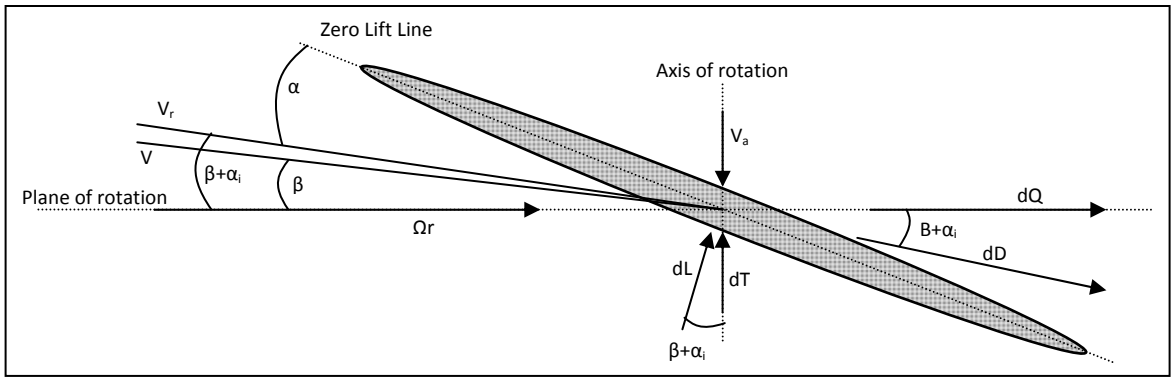

Figure 2-1: Force and velocity vector illustration

In the above figure Ω is rotational frequency and r is the radial distance away from the center of the hub. The velocity that the above foil encounters is made up of a rotational velocity vector, **Ωr**, and forward velocity vector, $\mathbf{V_a}$. Summing these two vectors together gives the propeller velocity vector, **V**. An increase in the angle of attack (AOA) of this incremental section, or pitch in the case of a propeller, will create an addition induced angle of attack, α_i. This additional induced AOA shifts the velocity vector seen by the propeller, **V**, to the vector $\mathbf{V_r}$. The result of this new velocity vector produces a change in thrust, dT, and a change in torque, dQ:

$$dT = [dLcos(\beta + \alpha_i) - dDsin(\beta + \alpha_i)] \quad (2\text{-}1)$$

$$dQ = r[dLsin(\beta + \alpha_i) + dDcos(\beta + \alpha_i)] \quad (2\text{-}2)$$

The sectional lift, dL, and sectional drag, dD, can be obtained by using the coefficients of lift, C_L, and drag, C_D, from the foils' cross-sectional geometry

$$dL = C_L[.5\rho V_R^2 c(dr)] \quad (2\text{-}3)$$

$$dD = C_D[.5\rho V_R^2 c(dr)] \quad (2\text{-}4)$$

where *c* is chord length and *dr* is the incremental span-wise length of the section. Experimental data for C_L and C_D based on the sectional geometry can be obtained from a NACA table, Abbot and Doenhoff, or other sources that use high aspect ratio wings to test two dimensional wing shapes. A two dimensional finite element method solver can also be used to solve for C_L and C_D.

2.2 - Ideal Hydrodynamic Fluid Approach

A fluid analysis approach to propeller performance allows a designer to see how changes in the fluid affect propeller performance. Momentum theory applied to an actuator disk makes it possible to get a form of ideal propeller efficiency based on propeller loading. In this approach we assume that the propeller can be represented by an actuator disk and thrust is distributed uniformly over its area. The frictional drag across the blades, shed vortices, as well as kinetic energy in the added swirl velocity and radial flow is not included in this approach. The momentum equation requires a large enough control volume that the pressure around its surface becomes free stream pressure [5].

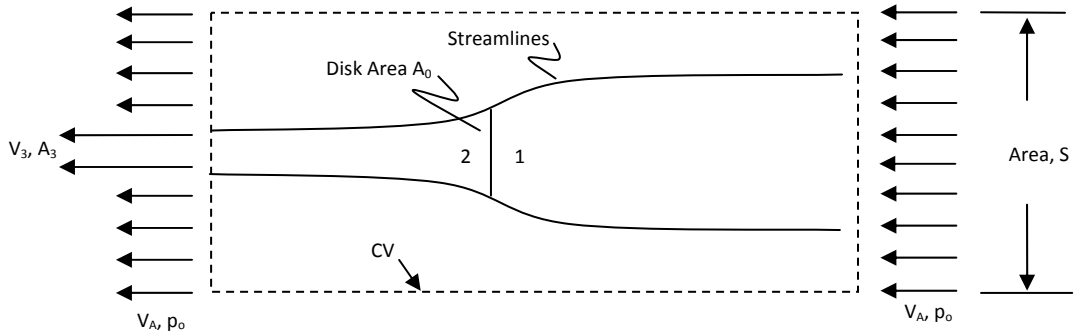

Figure 2-2: Actuator disk control volume illustration

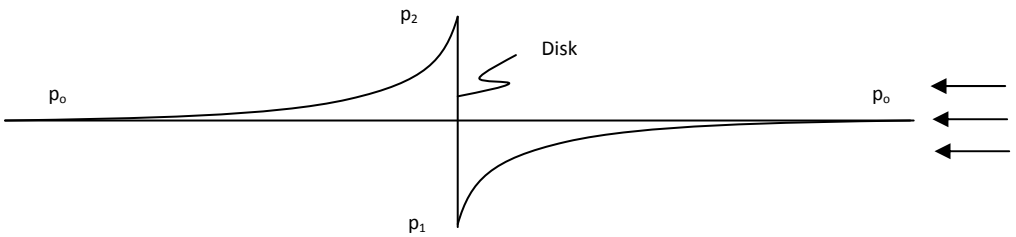

Figure 2-3: Axial pressure variation within the control volume

Applying the continuity equation to Figure 2-2 we get the following equation:

$$\frac{\partial \rho}{\partial t} + \nabla \cdot (\rho \boldsymbol{u}) = 0 \tag{2-5}$$

where ρ is density, t is time, and $\boldsymbol{u}$ is fluid velocity vector. For this analysis the propeller blade will be operating in water and this fluid can be considered incompressible. Also for this analysis a uniform flow will be assumed. Using these two assumptions the above equation can be reduced to:

$$\nabla \cdot \boldsymbol{u} = 0 \tag{2-6}$$

meaning there is no jump in velocity. Using volumetric flow rate and Figure 2-2:

$$\Delta Q = A_3 V_3 + (S - A_3)V_A - SV_A$$

$$\Delta Q = A_3(V_3 - V_A) \tag{2-7}$$

where ΔQ is volumetric flow rate. Using Figure 2-2 and the volumetric flow equation; total force, thurst (*T*), on the fluid can be represented by:

$$T = \rho[-S\,V_A^2 - \Delta Q\,V_A + A_3\,V_3^2 + (S - A_3)V_A^2]$$

$$T = \rho[-S\,V_A^2 - (A_3(V_3 - V_A))V_A + A_3\,V_3^2 + (S - A_3)V_A^2]$$

$$T = \rho A_3 V_3(V_3 - V_A) \tag{2-8}$$

where thrust is represented by mass flow rate in the stream tube, $\rho A_3 V_3$, and axial velocity increase, $(V_3 - V_A)$. Using conservation of mass:

$$\rho A_3 V_3 = \rho A_0 V_1$$

$$T = \rho A_0 V_1(V_3 - V_A) \tag{2-9}$$

Another equation is needed to find V_1**.** The force on the actuator disk is equal to the force on the fluid. The force on the actuator disk is due to the pressure difference across the disk:

$$T = A_0(p_2 - p_1)$$

$$\rho V_1(V_3 - V_A) = (p_2 - p_1) \tag{2-10}$$

where p_1 and p_2 are the pressure right before the actuator disk and right after. To put into terms of velocity we can apply Bernoulli's equation starting at the incoming flow of the stream tube to the actuator disk, and from the aft end of the actuator disk to the exit velocity of the control volume. Bernoulli's equation can't be used across the actuator disk because the added energy from the propeller blade violates Bernoulli's equation.

$$p_0 + .5\rho V_A^2 = p_1 + .5\rho V_1^2$$

$$p_0 + .5\rho V_3^2 = p_2 + .5\rho V_2^2$$

We can also use the V_1 = V_2 relationship to get:

$$p_2 - p_1 = .5\rho(V_3^2 - V_A^2) \tag{2-11}$$

Using equation 2-9 and 2-11 the velocity V_1 can be reduced to:

$$.5\rho(V_3^2 - V_A^2) = \rho V_1(V_3 - V_A)$$

$$V_1 = .5(V_3 + V_A) \tag{2-12}$$

From equation 2-12 we can state that the velocity at the disk is half the summation of the inflow velocity and the increase in velocity far down the slip stream (where the pressure has relaxed). The

relaxation in pressure far behind the disk gives an increase in velocity behind the disk. From this we can use a little algebra to get an ideal efficiency:

$$\eta_i = \frac{P_{out}}{P_{in}} = \frac{TV_A}{.5\dot{m}[V_3^2 - V_A^2]} = \frac{\rho A_0 V_1 (V_3 - V_A)V_A}{.5\rho A_0 V_1 (V_3^2 - V_A^2)} = \frac{(V_3 - V_A)V_A}{.5(V_3^2 - V_A^2)} = \frac{(V_3 - V_A)V_A}{.5(V_3 - V_A)(V_3 + V_A)}$$

$$= \frac{V_A}{V_1} \tag{2-13}$$

where the output power due to propeller thrust and inflow velocity is represented by P_{out} and power into the system due to the difference in energy flux produced by the propeller far down the slip stream is represented by P_{in}. The variable $\dot{m}$ represents the mass flow rate of the fluid. The efficiency can now be defined as the ratio of the free stream velocity to velocity at the disk. Since the notation of velocity gets a little confusing Principles of Naval Architecture [6] uses a slightly modified notation and is principally illustrated in Figure 2-4 below.

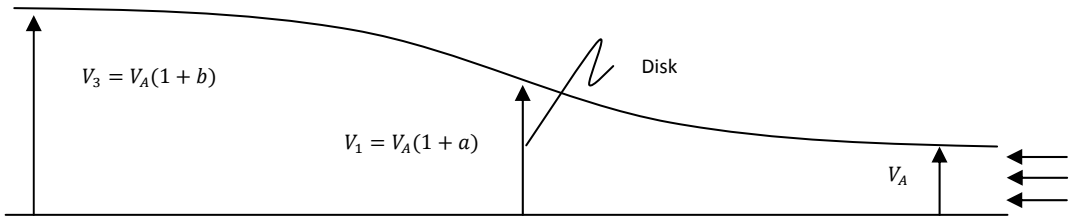

Figure 2-4: Velocity Profile along stream-tube

From the figure above it can be seen that V_1 and V_3 can be rewritten into a new form. A form that is dependent on constants a and b, as well as the incoming flow velocity V_A. The principle illustrated above is useful, but not necessary, and will not be used for this report.

It is useful to put ideal efficiency in terms of thrust coefficient, C_T, to show the effect of propeller loading on efficiency. The only energy loss using this analysis is the energy added to the axial flow. The actual efficiency is lower due to frictional drag across the blades, kinetic energy in the added swirl velocity, radial flow, and shed vortices[5].

$$\eta = \frac{2V_A}{(V_3 + V_A)} = \frac{2}{1 + {V_3}/{V_A}}$$

$$C_T = \frac{T}{.5\rho A_0 V_A^2} = \frac{\rho A_0 V_1 (V_3 - V_A)}{.5\rho A_0 V_A^2} = \frac{\rho A_0 .5(V_3 + V_A)(V_3 - V_A)}{.5\rho A_0 V_A^2} = \frac{V_A^2\left(\left({V_3}/{V_A}\right)^2 - 1\right)}{V_A^2}$$

$$\therefore \ {V_3}/{V_A} = \sqrt{C_T + 1}$$

$$\therefore \ \eta = \frac{2}{1+\sqrt{C_T+1}} \tag{2-14}$$

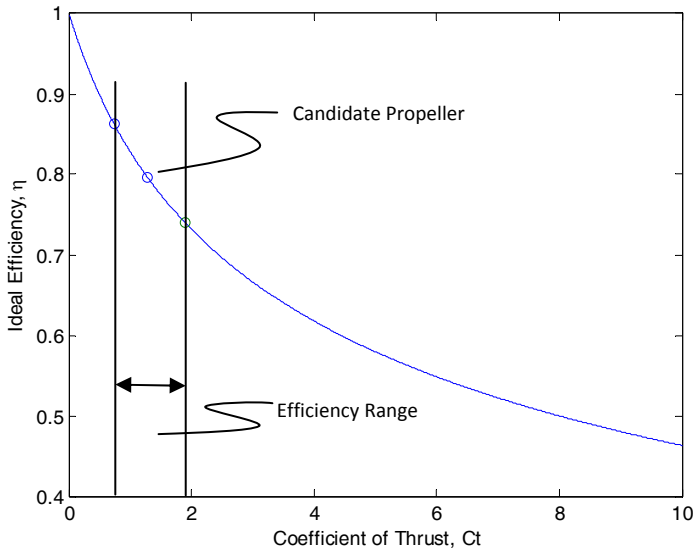

Figure 2-5: Ideal efficiency as a function of propeller loading

Given the mission statement, there is an ideal efficiency range that can be achieved based on the varying the diameter and assuming fresh water. The maximum attainable efficiency is 0.8624 with a propeller diameter of 4". The minimum ideal attainable efficiency is 0.7404 with a propeller diameter of 2.5". The candidate propeller chosen for this mission has a diameter of 0.077mm and gives an ideal efficiency of 0.7959. From this analysis it can be stated that a propeller with larger diameter will give a higher efficiency, assuming the thrust and incoming flow velocity is constant.

2.3 - Experimental Approach

The theoretical analysis above allows a propeller designer to estimate the general shape, size, and various dimensions of a propeller to meet the required performance of the blade. Experimental testing allows a designer to prove or disprove the estimated propeller effectiveness. Using the experimental data and a form of dimensional analysis a designer can see the variables that a propeller depends upon. The dimensional analysis for a propeller blade enables the rotational velocity, inflow velocity, torque, and thrust to be collapsed into a series of curves. Dimensionless quantities can help predict the performance of propeller blades over various rotational and inflow velocity ranges without actually testing those ranges. The analysis below is taken from PNA [6], section 3 and is used later in this report to test the candidate propeller.

Some values that thrust, T, and torque, Q, could depend on are:

a) Mass density of water, ρ
b) Size of propeller, represented by diameter D
c) Speed of advance, V_A
d) Acceleration due to gravity, g
e) Speed of rotation, n
f) Pressure in the fluid, p
g) Viscosity of the water, μ

$$T = f(\rho, D, V_A, g, n, p, \mu) \tag{2-15}$$

Similarly Torque, Q:

$$Q = f(\rho, D, V_A, g, n, p, \mu) \tag{2-16}$$

Putting these terms into the form of mass, length, and time (MLT), and performing a non-dimensional analysis, the quantities of thrust and torque can be put into the form:

$$K_T = \frac{T}{\rho D^4 n^2} \tag{2-17}$$

$$K_Q = \frac{Q}{\rho D^5 n^2} \tag{2-18}$$

The quantities of thrust and torque are dependent upon forward velocity, V_A, and speed of rotation, n (as seen in Figure 2-1). The non-dimensional quantity is represented by the advance ratio, J:

$$J = \frac{V_A}{nD} \tag{2-19}$$

where open-water efficiency, η_o, is represented by power out divided by power in:

$$\eta_o = \frac{TV_A}{2\pi n Q_o} = \frac{K_T}{K_Q}\frac{J}{2\pi} \tag{2-20}$$

A good example of using non-dimensional quantities to characterize propeller performance is the Wageningen B-Series. The Wageningen B-series propellers were designed at the Netherlands Ship Model Basin in Wageningen and the series consists of 120 propeller models tested in open-water[7]. Each propeller has different geometric features, such as: Blade Area Ratio (BAR; expanded blade area, A_e, relative to projected blade area, A_o), Pitch to Diameter ratio (P/D), and number of blades (Z). These propellers were later analyzed with a multiple polynomial regression analysis [8]. The dimensional analysis is similar to the one above to get K_T and K_Q, but assumes these quantities are dependent on J, P/D, BAR, Z, and t/c (where t is blade thickness and c is chord length). The t/c ratio was later removed using some assumptions of Reynolds effects [7]. This analysis allows a designer to pick from various propeller geometries and get a rough estimate of which propeller will produce enough thrust with good efficiency. For more information on the Wageningen analysis please see the paper produced by the University of Michigan [7].

The Wageningen polynomial regression produced in 1974[8] allows a designer to input four design constants (BAR, Z, J, and P/D) to get estimated performance coefficients (Kt, Kq, and efficiency). There are many limitations to this analysis, but one major one is extrapolation error. The ranges of this regression are proposed as being:

$$2 < Z < 7$$

$$0.30 < {}^{A_e}/_{A_o} < 1.05$$

$$0.5 < \frac{P}{D} < 1.40$$

Validation of the extreme ends of these ranges, such as high Z with low BAR, is of low reliability due to error in regression extrapolation. The use of the Wageningen B-series regression analysis proved to not be helpful in validating propeller efficiency in the later sections of this thesis.

Chapter 3 – Propeller Testing Equipment

3.1 - Wind Tunnel

The primary instrument used in this thesis to test propellers is a wind tunnel. The wind tunnel selected to test in is Virginia Tech's Open-Jet Wind Tunnel. This tunnel was constructed before 1937 by the Aeronautical Engineering Faculty. The following is a description of the tunnel design and dimensions, a majority of this material has been obtained by the AOE department at Virginia Tech [9]. The tunnel is an open-throat return type, with a three foot wide test section (see Figure 3-1 and Figure 3-2).

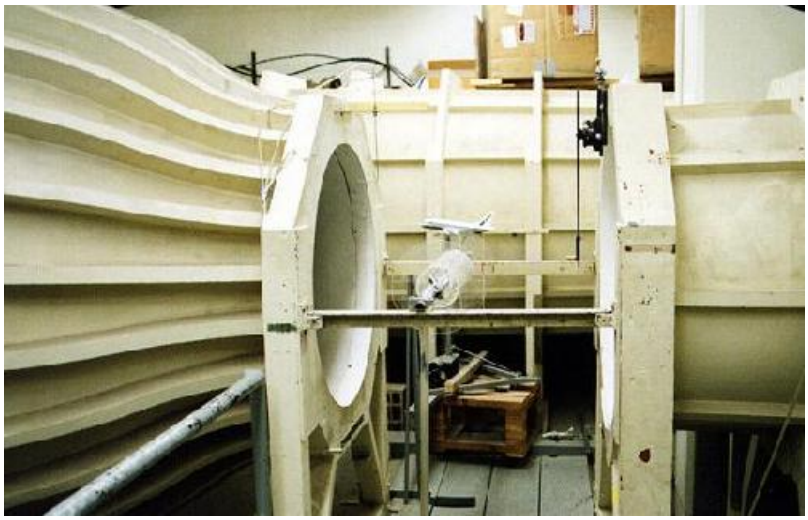

Figure 3-1: View of test section and return of the Instructional Tunnel [9]

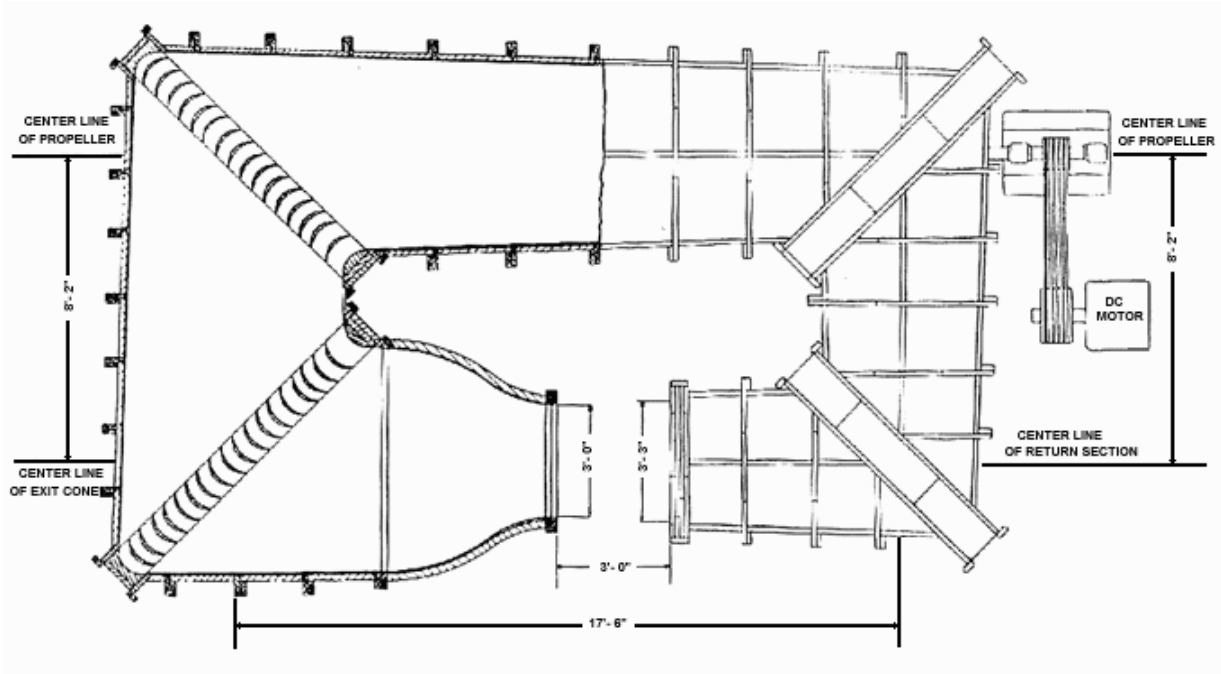

Figure 3-2: Schematic of the Student 3-Foot Open Test Section Instructional Tunnel [9]

Since this tunnel is square in form, straightening vanes at each corner are implemented to help maintain uniform air velocity at the opening of the test section. The tunnel flow velocity is estimated to operate from 0 to 150 MPH. More information about the tunnel can be found through Virginia Tech's AOE department website [9] [10].

Access to this tunnel was very convenient, but the tunnel has many undesirable characteristics. The design of the tunnel is quite large and the testing floor is connected to the tunnel structure, so vibration from the tunnel is transmitted to the testing area. The instrumentation used to test small propellers is located in the testing area of the tunnel and is very sensitive (+/- 50 grams for thrust). The wind tunnel transmits significant vibration from the tunnel to the instrumentation. This vibration appears in the data output by the sensors (most of it can be damped out with a low-pass filter). The vibration amplitude and frequency increase as the flow velocity increases. A soft rubber mat was placed on the floor of the tunnel to help alleviate these vibrations. Another undesirable characteristic of this tunnel is non-uniform cross-sectional velocity in the tunnel. The Pitot-Static tube was placed relatively close to the propeller rig due to this non-uniform cross-sectional velocity (see Figure 3-3).

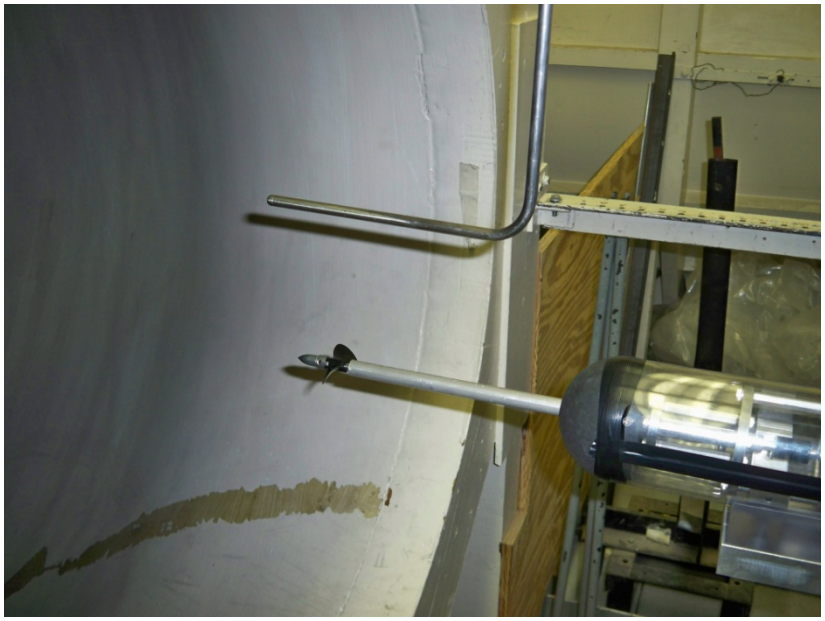

Figure 3-3: Pitot-static probe relative to propeller rig

An evaluation of the flow velocity variation in grid form was not formally tested or recorded, but variation on the order of 8-10 percent was observed by manually taking the probe and traversing it horizontally across the opening of the tunnel. According to the AOE 3054 lab manual [11] the tunnel exhibits a 5 percent velocity variation with an empty test section at about 36 m/s (see in Figure 3-4).

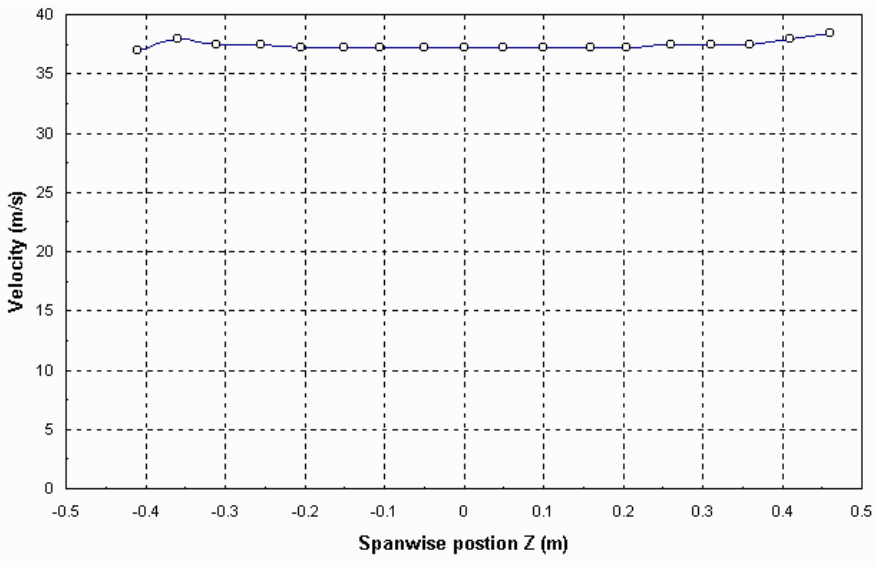

Figure 3-4: Mean-velocity distribution across the empty test-section of the open-jet wind tunnel.[11]

3.2 - Tunnel Instrumentation

3.2.1 – Pitot-Probe

A Dwyer model 160 Pitot-static probe is mounted to the front of the tunnel to measure free stream flow velocity. Pitot-static probes have been used throughout the early 1700's by the French [12] and remain one of the more reliable means to measure steady flow speed. The concept of the probe is total or stagnation pressure is measured at the front of the probe and static or total pressure is measured from the ports located perpendicular to the flow. Using these two pressure measurements we can use Bernoulli's equation to get flow speed.

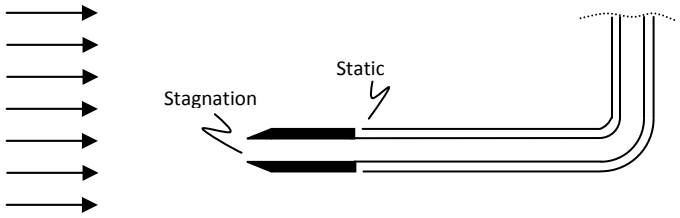

Figure 3-5: Pitot-Static probe

Though the Pitot-static tube has been around for many years and is a great way of measuring the velocity of steady flow; error arises when the probe is not properly aligned with the flow. This can be seen in the figure below:

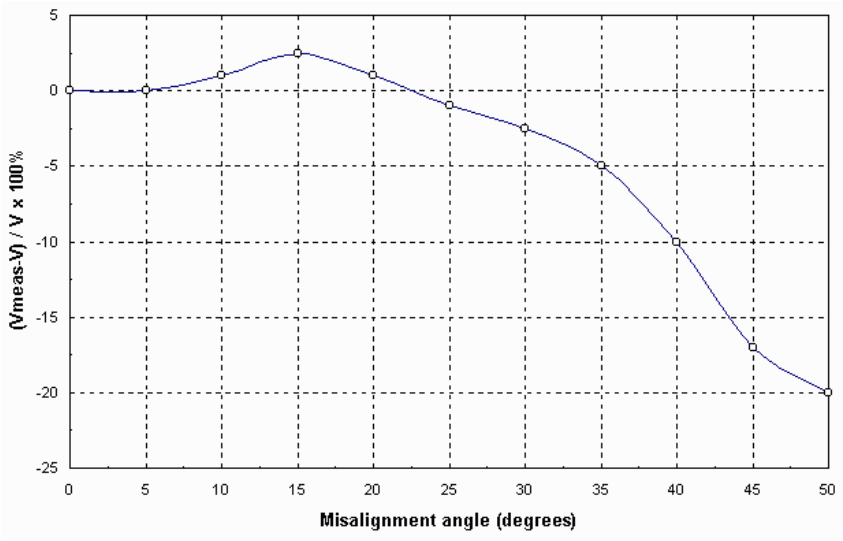

Figure 3-6: Errors due to misalignment in velocity measurements made with a Pitot-static probe. [11]

Where V is the actual velocity and Vmeas is velocity sensed by the Pitot-static probe.

3.2.2 – Digital Monometer

To measure the pressure difference in the Pitot-static probe a digital manometer was used. The digital manometer is a Dwyer, Series 475 Mark III. This digital manometer model measures pressure between 0-2.49 kPa and can handle a max pressure of 35kPa. Accuracy reported by the instrument is listed as +/- 0.5% at 60-78°F, +/- 1.5% at 32-60°F or 78-104°F. The pressure hysteresis is +/- 0.1% of full scale. A picture of this instrument can be seen below.

Figure 3-7: Dwyer Series 475 Mark III Digital Manometer

3.2.3 – Barometer

A Mechanism Ltd. Mk.2 precision aneroid barometer is used to measure ambient/atmospheric pressure. This instrument has a resolution of 5 Pa. The range is from 900-1050 mb or 90-105 kPa. This

instrument is commonly used to measure atmospheric pressure for scientific research. The aneroid barometer uses the deflection of one light, pivoted, counter-balanced electrical contact arm mounted in jeweled bearings. Electrical contact is established by manually rotating a micrometer screw. The reduction in the backlash friction to negligible proportion greatly increases the absolute accuracy of the instrument [13]. A picture of this instrument can be seen below.

Figure 3-8: Mechanism Ltd. Mk.2 precision aneroid barometer

3.2.4 – Digital Thermometer

To measure temperature a wired RadioShack indoor/outdoor thermometer was used. A specifications sheet couldn't be found for this instrument. Using contemporary models and experimental data an estimated resolution of 1°F and an estimated range of -4 to 104°F were determined. A picture of this instrument can be seen below:

Figure 3-9: Wind tunnel thermometer

3.3 – Propeller Test Rig and Propeller Test Stand

The propeller test rig is quite complicated and requires some explanation of the components used as well as the methodology behind construction. The propeller test rig and stand were designed and fabricated at Virginia Tech for the purpose of this thesis. A detailed explanation of the propeller test

rig and stand is required since no formal write-up at this time exists. The internals will be discussed generally in this section and fully explained in the later sections. It should be stated that most of the propeller test rig components were designed to reduce noise and or transmit small values of thrust and torque to their respective sensors. A general picture, not to exact proportions, but close, can be seen below:

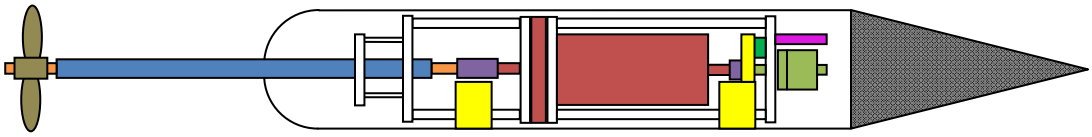

Figure 3-10: Propeller test rig component illustration (side view)

There are four pieces that make up the shell of the rig: a top and bottom half of a polycarbonate tube, a rubber nose cone, and a PVC tail (this allows easy access to the internals). The inner support structure is made up of aluminum disks and aluminum or stainless steel standoffs. The purpose of the propeller test rig is to measure thrust, torque, and motor revolution. To measure thrust the entire unit, including the torque sensor, has to be mounted rigidly together so that the thrust from the propeller can be transferred to a load cell. The transfer of thrust from the propeller (marked tan in Figure 3-10) to the load cell (marked dark green in Figure 3-10) is implemented by having the whole assembly travel axially via aluminum mounts (marked yellow in Figure 3-10). The bottom standoffs being made of smooth stainless steel shaft and inside the mounts are linear shaft bearings. Two linear shaft bearings are in each mount, which allow for a four point stability system (allow for more direct transfer of axial thrust). As seen in Figure 3-10 above the torque sensor (marked red in Figure 3-10) requires about half the total length of the internals. The propeller is attached to a drive shaft (marked orange in Figure 3-10) and spins inside of another shaft (marked blue in Figure 3-10) that houses four rotational ball bearing assemblies, spaced equally along the shaft. Originally only two rotational ball bearing assemblies where used but due to the shaft's length it would deflect enough to touch the inside of the outer shaft during operation. Much effort was made to balance the propeller and shaft without changing the number of bearings used, but the effort was not successful. A coupler is added between the propeller shaft and torque sensor as well as between the torque sensor and the motor (marked light green in Figure 3-10). Vibration seemed to resonate from the torque sensor while in operation. The oscillation appeared to be representative of a cantilever beam, despite the rigid coupler between the motor and the torque sensor. To reduce this vibration rubber was casted between the torque sensor and the struts. The final component is a RPM sensor; it measures the rotation of the motor as it spins (marked pink in Figure 3-10).

Another design feature of the propeller test rig is minimal or no flow through the shell. There is a small opening for the propeller shaft to exit from the propeller test rig nose, with no exit for that opening. The propeller test rig is sealed with tape along the seams. Sealing the propeller test rig ensures the pressure on the inside of the test rig is equal to the total pressure in the tunnel. The purpose of this feature is to eliminate drag on the internals which adds a false thrust value as velocity increases. See Figure 3-11 and Figure 3-12 below to see propeller test rig shaft to nose tolerance and sealing.

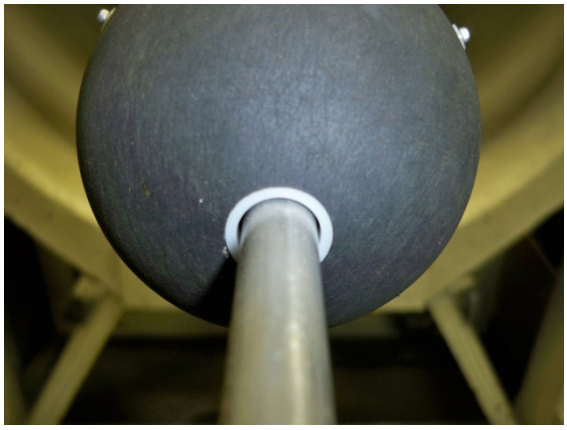

Figure 3-11: Propeller test rig shaft to nose tolerance

Figure 3-12: Propeller test rig sealing

Using Hoerner's book on drag [14], an estimate of pressure build up around the nose of the rig requires at least one and a half times the diameter of the rig. The pressure buildup from the nose could affect the addition axial velocity contribution from the propeller. The length of the shaft from the exit of the front of the propeller test rig to the propeller blade is three times the diameter of the propeller test rig.

The mounting of propeller test rig is equally as important as the propeller test rig. A picture of the propeller test rig and propeller stand can be seen below in Figure 3-13. There are three parts to the stand: first is the base; it is made of steel to hold the propeller test rig and accessories down when there is drag on the body of the propeller test rig. The second is a hollow shaft that runs from the bottom of the base to a rigidly attached flat plate that the propeller test rig can mount to. The flat plate gives a place to level out the stand. Leveling of the stand allows the propeller to see horizontal tunnel flow and removes gravitational effects on the load cell. The hollow shaft is designed to allow the wires to pass down the tube and out the bottom without being in the flow. If the wires were exposed to the flow a non-linear induced thrust would be added to the thrust measured by load cell. The final component of this stand is a machined polycarbonate plate that matches the bottom half of the propeller test rig shell. This machined plate allows the wires to pass from the hull to the hollow shaft. As mentioned in the tunnel section; a rubber mat was placed under the base of the propeller test stand to reduce noise from

the tunnel. The propeller test rig and propeller test stand together can be seen in Figure 3-13 below. The propeller test stand leveling can be seen in Figure 3-14 below.

Figure 3-13: Propeller test rig and propeller test stand

Figure 3-14: Propeller test stand leveling

3.3.1 – Load Cell

A Honeywell, Model 31 Low, Low Range Precision Miniature Load Cell was used to measure the propeller thrust. Both tension and compression can be sensed by this load cell, which is useful to get a good zero crossing of thrust (useful for establishing the pitch to diameter ratio P/D of the propeller blade). The unit is essentially a packaged and highly reliable strain gauge setup. The load range is +/-50g with a 5lb max load and infinite resolution. Linearity and hysteresis are both +/-0.15% full scale. Ideal temperature range is from -53°C to 121°C. For a full spec sheet please see Honeywell's website[15]. A dimensioned schematic and picture can be seen in Figure 3-15. The load cell was calibrated outside the propeller test rig, inside the propeller test rig and outside the tunnel, and inside the propeller test rig and inside the tunnel; all the slopes were found to be different from each other. The calibration in the tunnel was trusted as reliable because it was repeatable and the values measured in the tunnel are the

values desired for testing. The calibration difference of the other positions was assumed to be due to gravitational effects, rolling resistance, and the interaction between bearing shaft and the propeller test rig nose (if misaligned). The calibration in the tunnel used a smooth stainless steel shaft, cloth string, a metal hook, and known weights. The calibration process is shown in Figure 3-16. Calibration in the tunnel required the removal of the tail cone of the propeller test rig and the cloth string was attached to the RPM sensor instead of the propeller as shown in Figure 3-16.

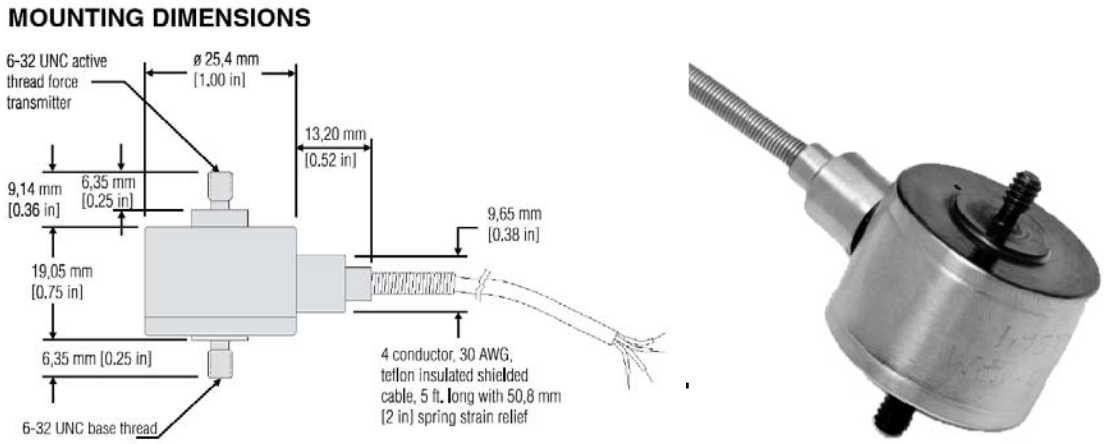

Figure 3-15: Honeywell, Model 31 Low, Low Range Precision Miniature Load Cell [15]

Figure 3-16: Propeller test rig load cell calibration process

3.3.2 – Torque Sensor

A Vibrac, Series I, TQ10, Torque Measuring Transducer, was used to measure propeller torque. The torque sensor uses a light shuttering system to measure angular torsion. This technique allows the shaft to spin freely without brushes or slip rings and in turn allows for longer life and cleaner signals. Torque can be measured at +/-10oz-in with accuracy of +/-1% of span. The moment of inertia of this rotating mass is 2.15E-4oz-in-sec^2. The torque transducer has a bearing drag torque of 0.05oz-in. The overload capacity is at least +/-20oz-in. The sensor shaft can spin at 10,000 RPM (higher with dynamic balancing). A schematic and a picture of this sensor can be seen in Figure 3-17. Calibration of this torque sensor was done statically (dynamic balancing was unavailable). To calibrate one end of the torque sensor was held in place while the other had a torque applied to it. A constant torque was applied by using a lever arm (hex key) and known weights (washers). A picture of the calibration process can be seen in Figure 3-18.

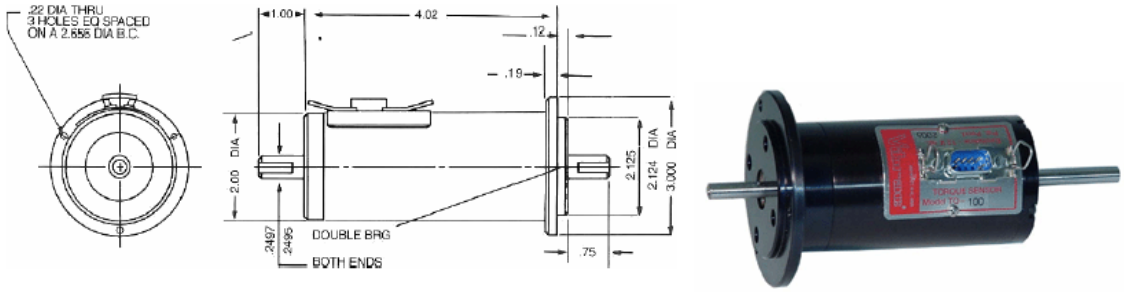

Figure 3-17: Vibrac, Series I, TQ10, Torque Measuring Transducer schematic and picture [16]

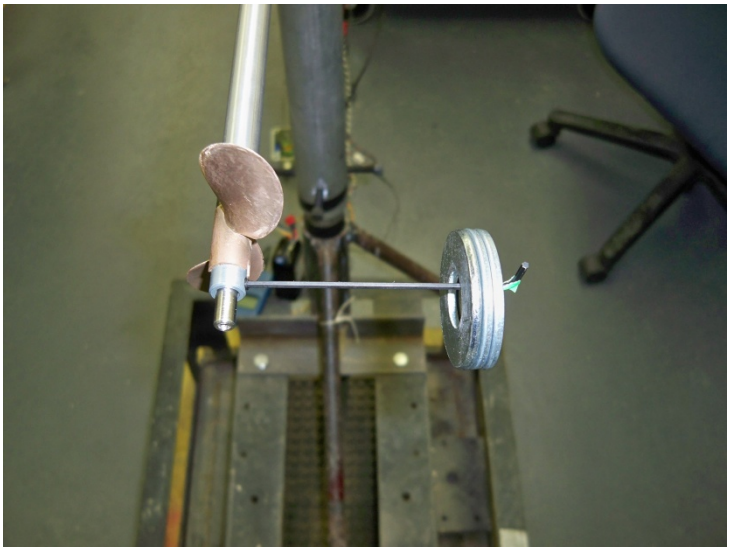

Figure 3-18: Vibrac, Series I, TQ10, Torque Measuring Transducer calibration process

3.3.3 – RPM Board

The RPM board was designed and built at Virginia Tech using an Allegro True Speed, High Accuracy, Gear Tooth Sensor (Hall Effect sensor), with a basic logic and signal manipulation board that

outputs a 0-5V square wave as the sensor is switched. Five volts is input into the sensor. The sensor has a negligible current draw. The RPM board was calibrated using a Shimpo, DT-315A stroboscope. The scope can flash between 40.0-35000 times per minute with an accuracy of +/- 0.01% of reading.

3.3.4 – Motor

The motor chosen was a Hyperion 2213-24, see Figure 3-19. The designation 2213-24 indicates to the consumer that the motor is 22mm in diameter, has a 13mm stator length and 24 winds of copper wire per stator arm. This motor is suitable for the propellers and power source we will be using. This motor it is able to spin in the 13k RPM range with the 16V power supply used in testing. This motor has enough power to spin much larger propellers, just not at the same RPM due to torque requirements of larger propellers. For this setup a Hyperion Titan 10A motor controller was used, see Figure 3-20. If larger propellers are used, a motor controller with a higher amperage rating may be needed.

Figure 3-19: Hyperion 2213-24 BLDC motor [17]

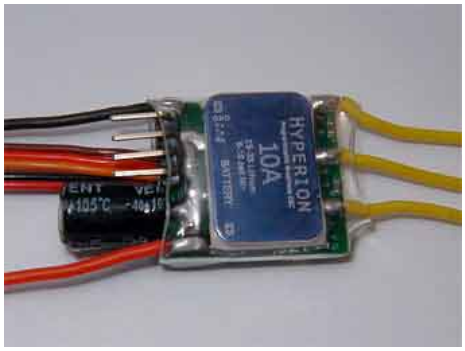

Figure 3-20: Hyperion Titan 10A Motor Controller [17]

3.4 – Signal Generation, Manipulation and Acquisition

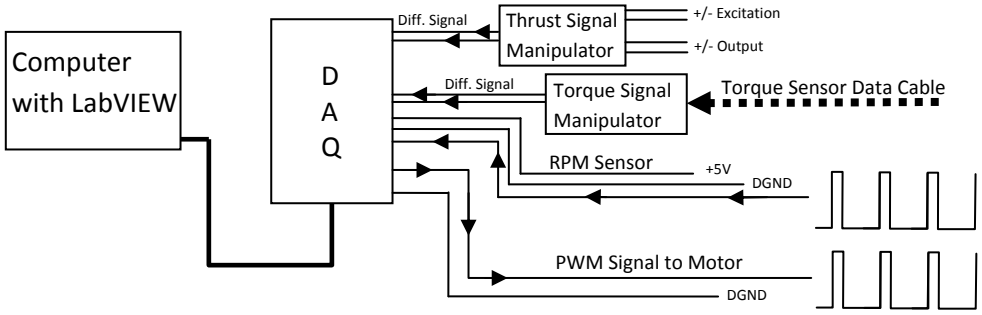

Figure 3-21: Signal Generation, Manipulation and Acquisition Architecture Schematic

Signal generation, manipulation, and acquisition can be very useful to gather data at high rates and store it. A good knowledge of electronics and data collection is required to build and manipulate the basic architecture of signal generation, manipulation, and acquisition. Implementing good signal architecture allows for easy error checking and less trouble as the system becomes more complex. This basic architecture can be seen above in Figure 3-21 and is quite simple. Starting from right to left; each sensor is attached via a series of wires from the transducer to a signal manipulator to the data acquisition (DAQ) unit or directly to the data acquisition unit. Each signal manipulator will be explained below. The voltage from the manipulators to the DAQ is between 0-5V or -5 to 5V or -10 to 10V. The DAQ samples each line one by one very quickly and sends this information to the computer. The computer reads the information and using National Instruments LabVIEW software it is manipulated or displayed to allow the user to interpret the refined data. A screenshot of the LabVIEW front panel and block diagram for this thesis can be seen in Figure 3-22 and Figure 3-23. The results of manipulation in LabVIEW can then be stored and further refined later. An important lesson learned from this thesis is to properly ground instrumentation. Without proper grounding, a grounding loop will occur. A grounding loop shows up in the data being collected as a “false” signal that has a frequency of 60Hz (assuming the instruments are using 115V AC power supply). A good picture of the wiring can be seen in Figure 3-24, note that the grounds are connected.

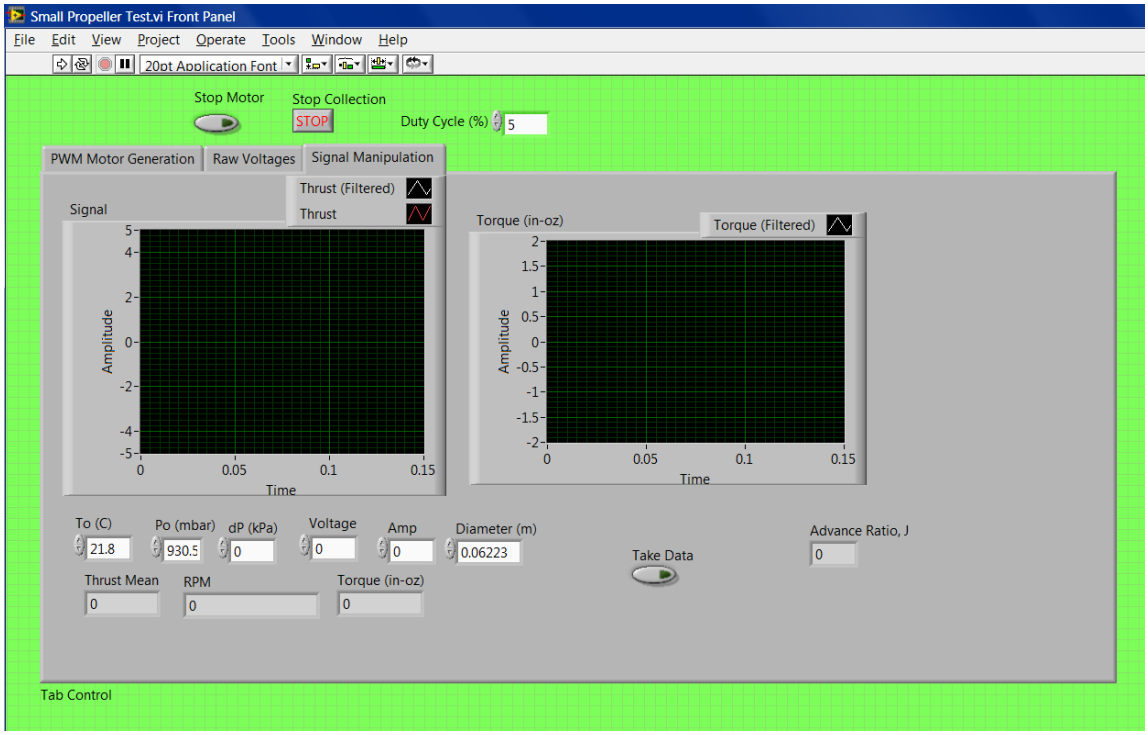

Figure 3-22: LabVIEW front panel screenshot

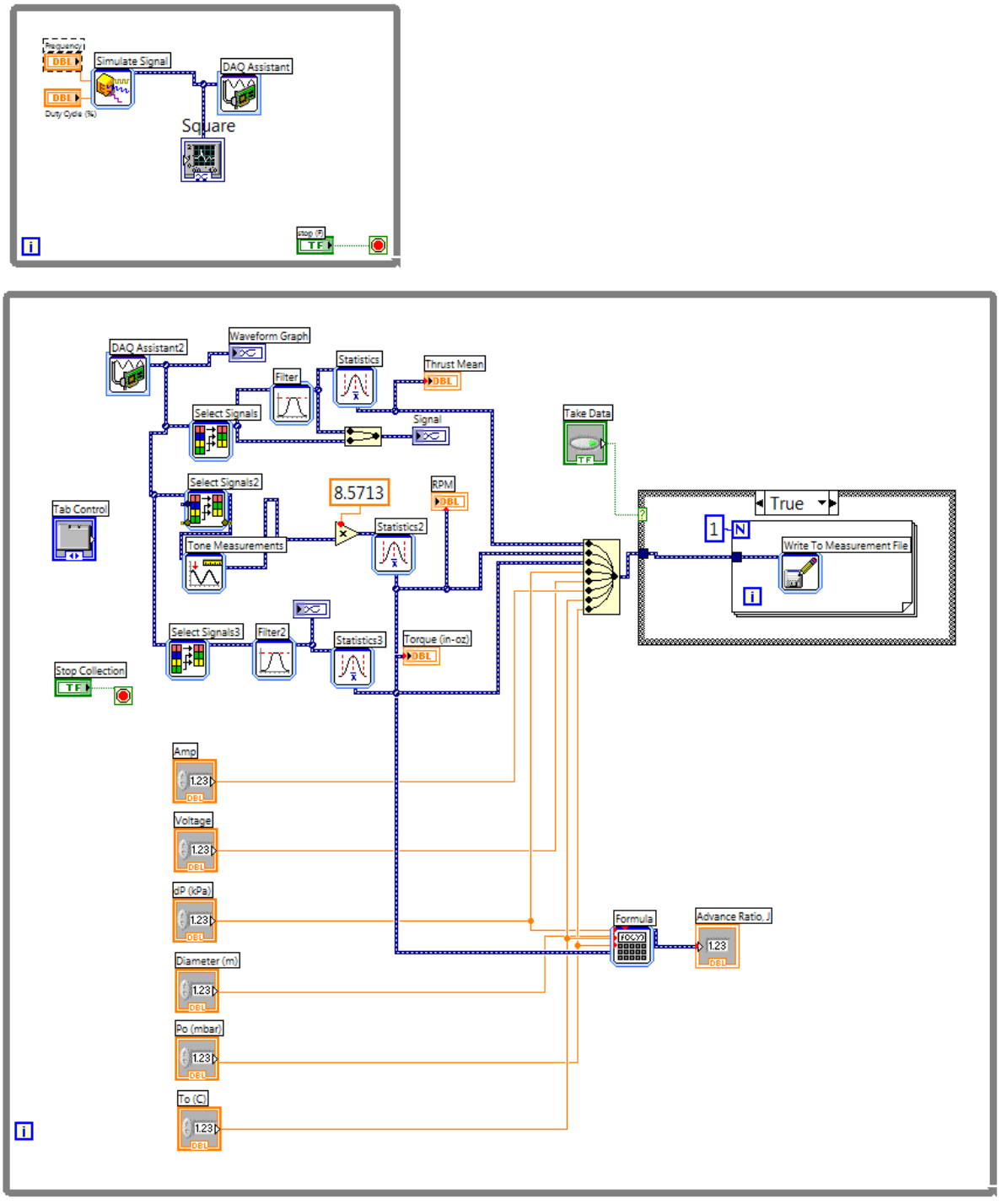

Figure 3-23: LabVIEW block diagram screenshot

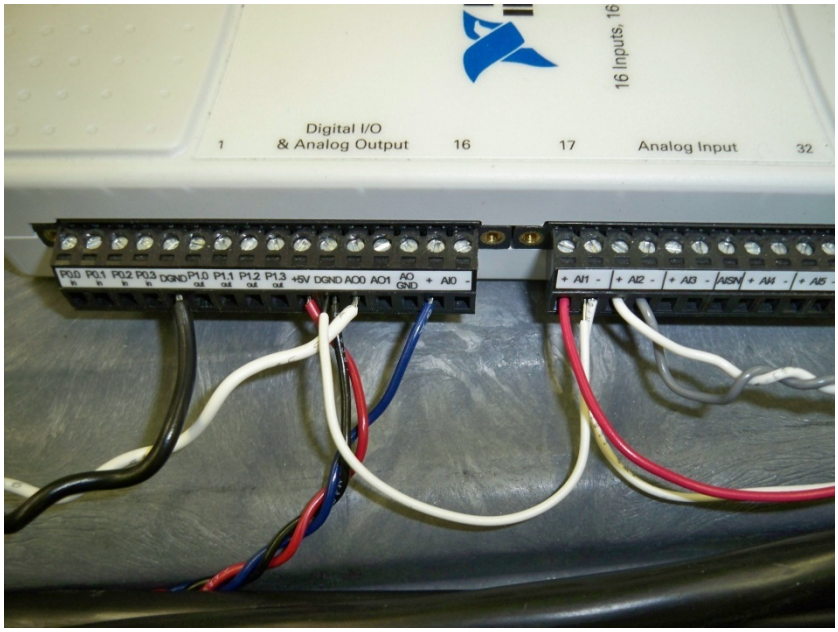

Figure 3-24: Wiring of DAQ box

3.4.1 – PWM Signal to Motor

A Pulse Width Modulated (PWM) signal ranging from 5-10% duty cycle at 50 Hz is sent to the motor controller. The signal generated from the DAQ and sent to the motor controller (or electronic speed controller ESC) is switched on and off from 0 to 5V. The motor controller then interprets the pulse width of this signal from the DAQ and depending on how it has been modulated will increase or decrease the power being supplied to the motor. The process of supplying power from the ESC to the motor requires the use of MOSFET's (Metal-Oxide-Semiconductor Field-Effect transistor [18]); which have a source, drain, and switch. MOSFET's allow the transfer power to be turned on and off very rapidly. The switching is what allows the motor to rotate between permanent magnets and electromagnets. The power from the motor controller to the motor is electrically commutated to generate something similar to a three phase sine wave. The commutated, pseudo sine wave, allows the motor to switch polarity of each stator arm in the motor and in turn rotate the magnets around the stator. There is much more detail to this process, but will not be discussed here. The ESC chosen for this experiment is a Hyperion Titan Series Brushless ESC 10A. The ESC chosen can commutate at 5754 times per second and 1918 times per second per MOSFET.

3.4.2 – RPM Signal

The RPM signal requires no hardware to manipulate the signal. The signal output from the sensor is 0 or 5V and is represented by a square wave. The square wave from the sensor is sent to the DAQ box. The DAQ box sends the signal to the computer where the computer uses LabVIEW software to interpret the frequency that the signal is oscillating at. The frequency of this signal is multiplied by 8.5713 RPM/Hz to put the signal into RPM. This conversion can be seen below:

$$\mathrm{RPM} = \frac{\text{Frequency}\left(\frac{\text{rev}}{\text{s}}\right)}{\#\text{ of positively faced magnets}}\left(60\,\frac{\text{sec}}{\text{min}}\right) = \mathrm{f} * \frac{60}{7} \tag{3-1}$$

From here the signal is averaged and displayed. The values displayed can be stored in a data file for later.

3.4.3 – Torque Signal

The torque signal is passed from the sensor to a Vibrac Motorized Dynamometer Instrument Model 1038 (see Figure 3-25) via a relatively large data cable. This instrument is able to run a motor, read RPM, and much more. Only torque was used for propeller testing. The unit has a method of manipulating the signal that is proprietary, but for this experiment it can be understood that a -10 to 10V differential signal is being sent to the DAQ. This signal's zero can be manually adjusted on the dynamometer. The signal is filtered digitally using LabVIEW; the filter is a low pass third order Butterworth with a cut off frequency of 5Hz. The signal is then averaged and sent to display. The signal can also be stored digitally if the used derires.

Figure 3-25: Vibrac Motorized Dynamometer Instrument Model 1038 [16]

3.4.4 – Thrust Signal

The thrust signal is amplified by a Sensotec In-Line Amplifier, model: Universal Bi-Polar (UBP). The unit requires 15VDC power source and amplifies the signal to +/-5V. The span adjustment range is from 0.5 to 10 mV/V. The zero can be adjusted +/-50% on using the course controller and +/-15% on the fine controller. Linearity is 0.01% of full span. Wiring of the thrust signal amplifier can be seen in Figure 3-26. A schematic of the thrust signal amplifier can be seen in Figure 3-27. The differential signal is then sent to the DAQ and into the computer where the signal is then again modified. The signal is filtered digitally using LabVIEW; the filter is a low pass third order Butterworth with a cut off frequency of 4Hz. The signal is then averaged and sent to display and can be saved later. The signal is not converted into a force until after the experiment is completed.

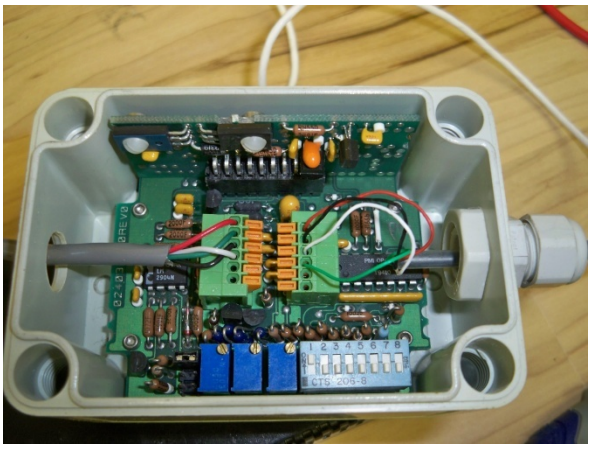

Figure 3-26: Sensotec In-Line Amplifier, model: Universal Bi-Polar (UBP) wiring

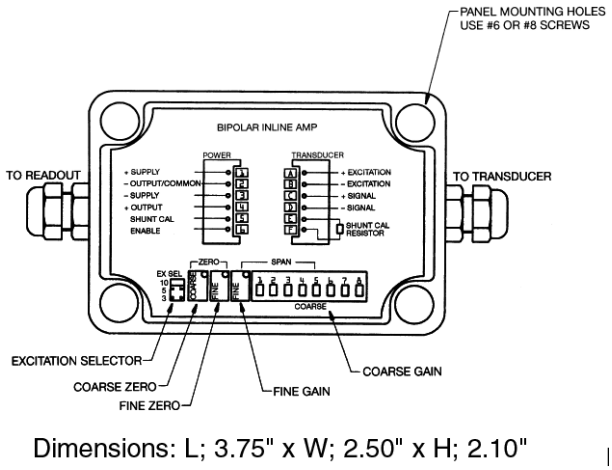

Figure 3-27: Sensotec In-Line Amplifier, model: Universal Bi-Polar (UBP) schematic [19]

3.4.5 – DAQ

The data acquisition unit is a National Instruments (NI) USB 6211. This unit is capable of reading 8 differential signals or 16 single ended signals. The analog to digital resolution is 16 bits with a maximum sampling rate of 250,000 samples per second over the given channels. The USB 6211 is capable of 50 pulse position modulations (ppm) of sample rate and 50 ns of resolution. The input range can be set to read +/-10V, +/-5V, +/-1V, or +/-0.2V for each channel. The DAQ unit can be adjusted to suite many needs including; sampling, writing, providing a 5V source, and common grounding. The DAQ uses a multiplexer which allows multiple signals to be recorded. Differential mode allows no assumptions of ground lines and noise contamination is not as much of a problem, though it takes two signal inputs. One important characteristic to note is: there is actually a delay between sampling between multiple lines. The "true" values are off from each other by 1/250000th of a second and with high frequency applications this may not be acceptable. So a sample and hold capability allows you to truly sample simultaneously. Sample and hold capability was not needed for this experiment.

Resolution, of the analog to digital, A/D, converter is calculated using:

$$Q = {}^{E_{FSR}}/_{2^M} = {}^{E_{FSR}}/_{N}$$

where Q is the resolution in volts per step (volts per output code), E_{FSR} is the full scale voltage range, and M is the A/D converters resolution in bits. N is the number of intervals of available output codes [20]. For the load cell, torque sensor, and RPM sensor, the resolution is 0.153, 0.305, and 0.076 mV/code respectively.

When sampling a signal the sampling has to be twice the highest frequency of the desired signal to avoid aliasing. This is known as the Nyquist Criterion.

Chapter 4 – Propeller Analysis

4.1 – Propeller Selection Process

One major objective of this report is to design a propeller that will have high efficiency and meet the mission requirements. The propeller geometry: diameter, pitch, skew, blade area, and shape are all factors in designing this theoretical propeller (see Figure 4-1). This design space is too large to experimentally test. In this section a method of propeller selection is developed to help pick an efficient propeller. To guide in the selection process a MATLAB® program designed by various sources at MIT[21] called OpenProp is implemented. This program uses a propeller vortex lattice lifting line theory to adjust the pitch of each small segment along the radius of the blade to meet the input requirements specified by the user (see Figure 4-2). OpenProp uses general geometry and power requirements, to evaluate a Lerbs, Horseshoe, and Wretch function that in turn gives the circulation distribution along the blade. The extent of this code will not be discussed here, more information on the theory and code can be found in Kerwin, 2001 [22] and Chung, 2007 [23] respectively.

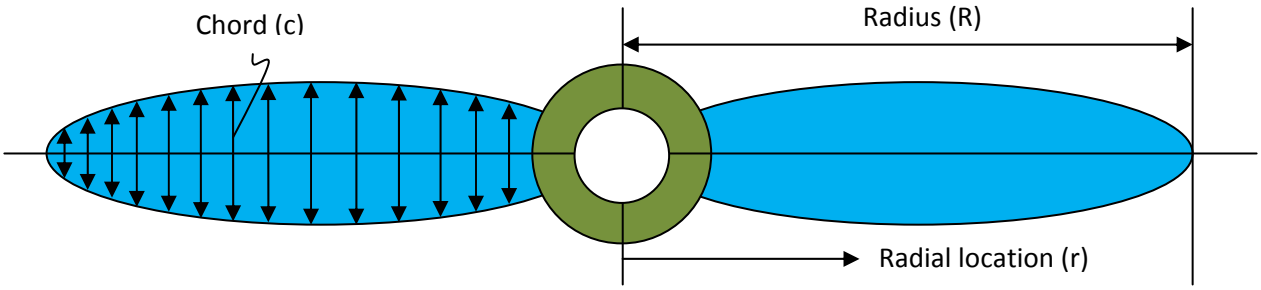

Figure 4-1: Propeller Geometry (simplified)

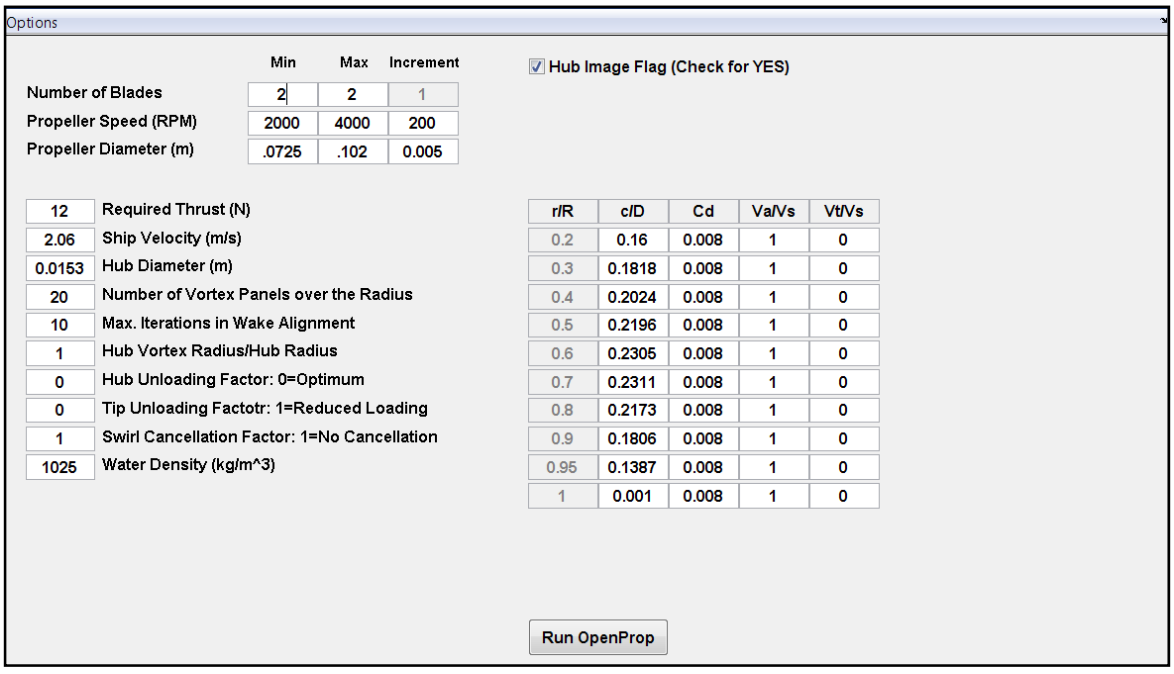

Figure 4-2: OpenProp input screen

Commercial off the shelf (COTS) small propeller blades are found relatively easy by searching the internet. Small Blade Area Ratio (BAR) propellers are generally designed for remote control airplanes and helicopters. Medium BAR are usually designed for bigger aircraft that require more thrust or boats and submarines that require less thrust than the large BAR marine grade propellers. Large BAR propellers are generally designed for marine applications. The design space of this analysis is not limited to any BAR, and therefore all three were considered. The three basic shapes were used to parametrically evaluate efficiency; small, medium, and large blade area ratio's. The figure below shows the dimensionless chord distribution of the small, medium, and large BAR's (see Appendix A for tabulated values):

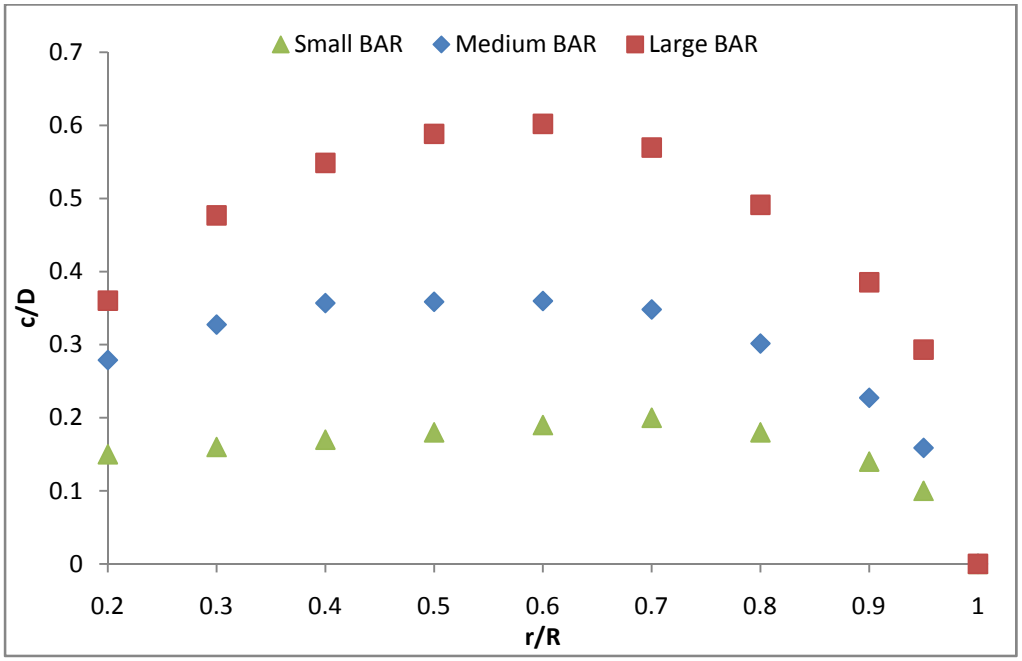

Figure 4-3: Chord to diameter ratios of small medium and large BAR's tested

The above figure shows the radial chord distribution of a small, medium, and large BAR propeller. For a specific thrust requirement, each propeller could have the same amount of expanded blade area, but with a different pitch. The design space is now comprised of small, medium, and large BAR's. The next step is to generate a series of propellers with changing RPM and diameter to give the maximum efficiency. The propeller diameter is limited to propeller blades between 2.5" and 4.0" from the mission statement. RPM was limited to a range between 2000 and 4000 RPM, based on previous experience of direct drive electric motors, which is a very fast spinning propeller blade if you were to compare it to a large ship. Only two bladed propellers were evaluated because they offer higher overall efficiency values as compared to three or more blades. Two bladed propellers are also the most common commercial propellers in the RC market. Using the mission statement, a 15% hub diameter requirement, and the information explained in this paragraph, the following values were put into OpenProp:

a) Thrust Required = 12N
b) Velocity Required = 2 m/s

c) Hub diameter = 15.3 mm (0.6”)
d) Number of blades = 2
e) RPM 2k-4k increment of 200
f) Prop Diameter 63.5-101.6 mm (2.5”-4”) increments of 0.5 mm

The rest of the input values were left to the preset values given by OpenProp (see Figure 4-2). The results of these input values can be seen below:

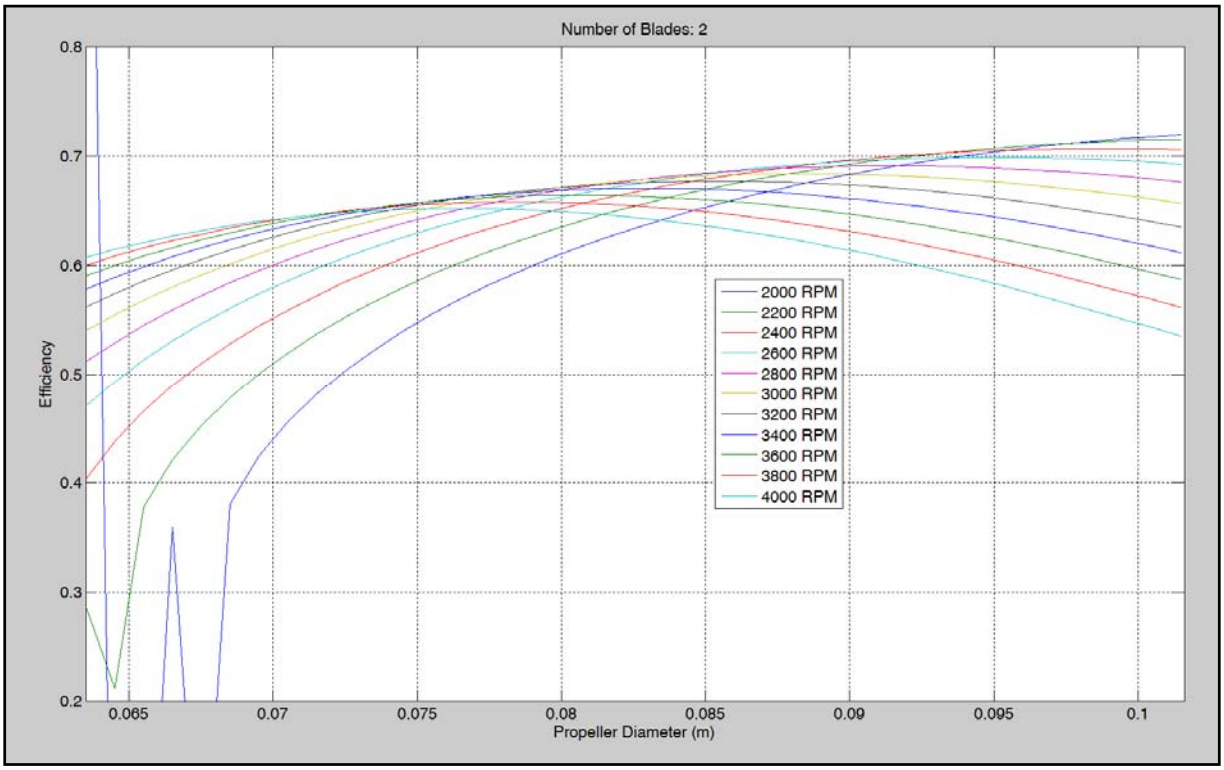

Figure 4-4: Small Blade Area Ratio parametric efficiency output

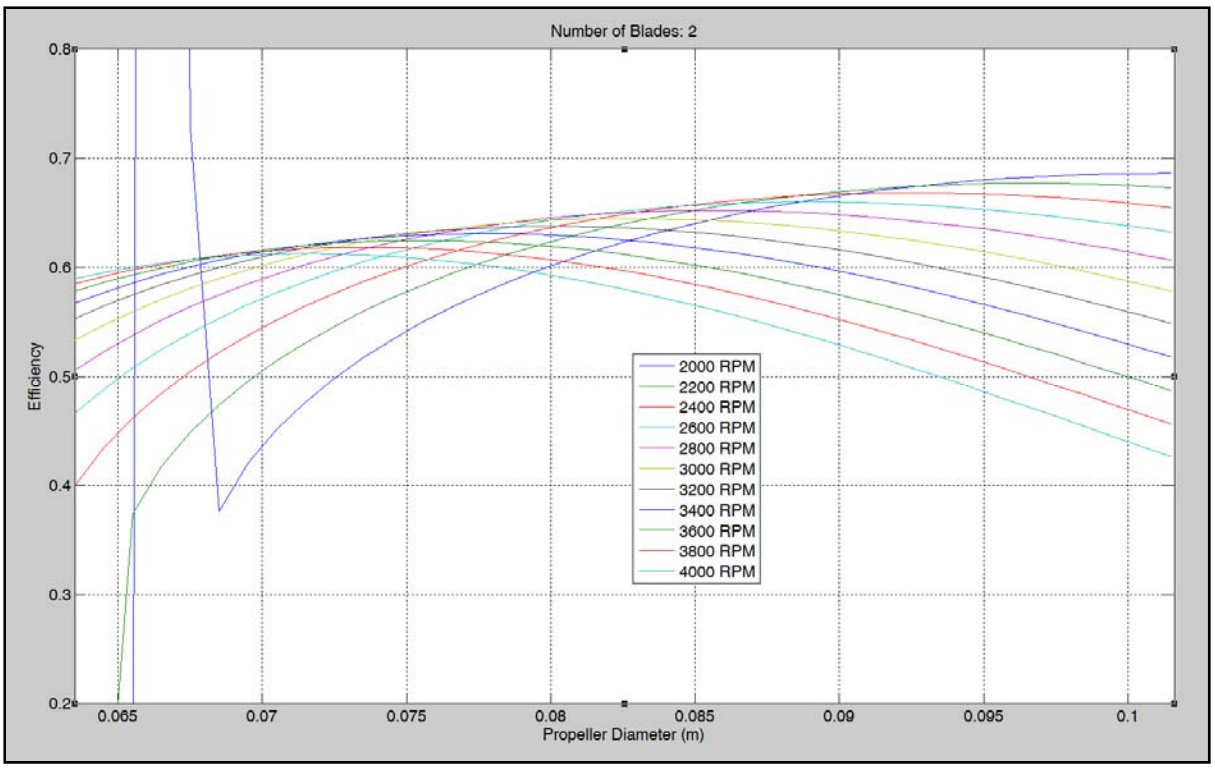

Figure 4-5: Medium Blade Area Ratio parametric efficiency output

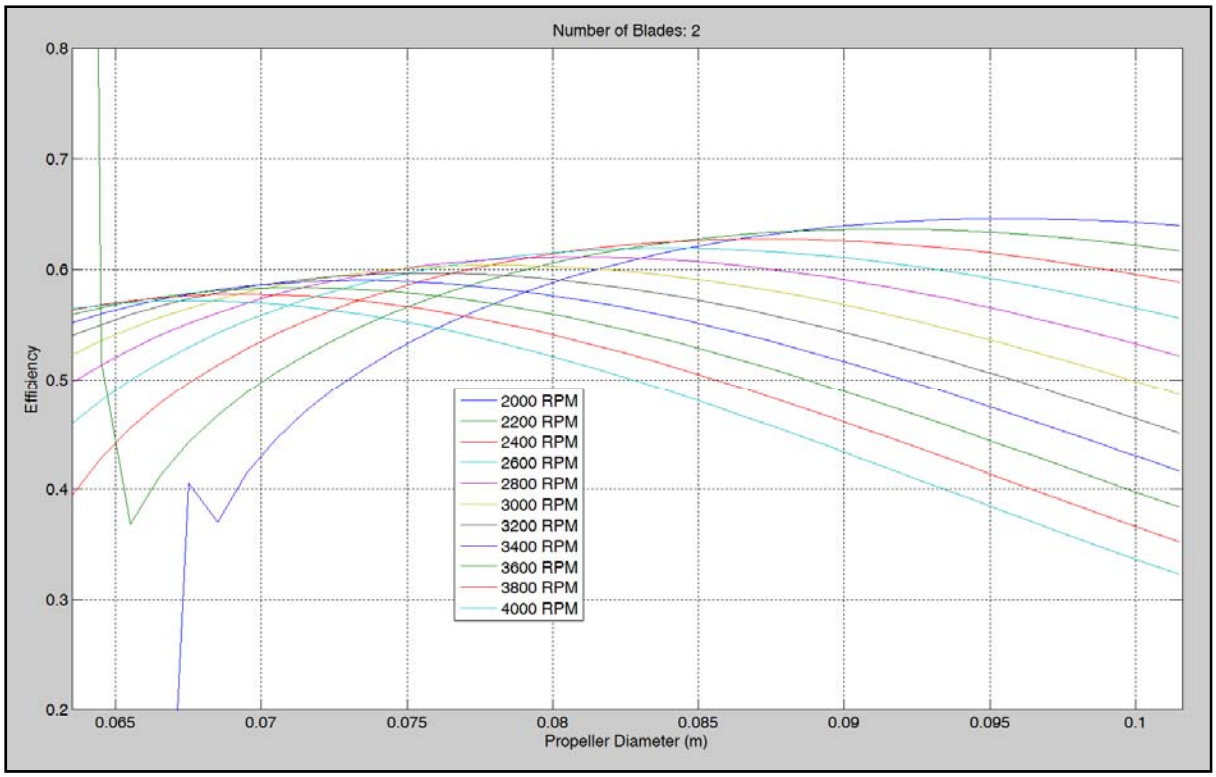

Figure 4-6: Large Blade Area Ratio parametric efficiency output

Each point in above figures represents a different propeller that has been optimized by varying the pitch angle along the propeller blade. The curves in the above figures show a full range of propellers that could be used to conduct the mission stated in the mission statement. For this study maximum efficiency for a given RPM is desired. The maximum efficiency and RPM together yield a propeller diameter that would give good efficiency. Since the velocity of vehicle, RPM, and diameter are known; an expected advance ratio of small medium and large BAR's with their respective efficiencies can be obtained and plotted to reveal candidate propellers.

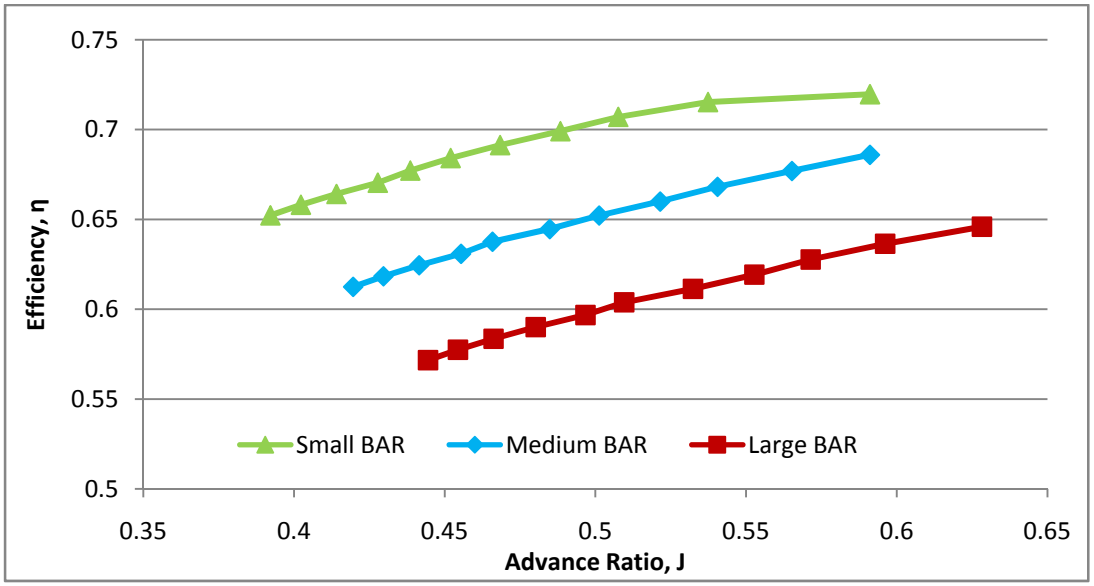

Figure 4-7: Efficiency vs. advance ratio for small, medium, and large BAR's

In the above figure, starting from left to right, RPM incrementally decreases from 4000 to 2000 by increments of 200 and is represented by each point (please see Appendix A for more detail). Please note that for the small BAR propeller curve, the efficiency curve was still climbing when the diameter limitation set forth in the mission statement stopped the curve from climbing higher (there is obvious non-uniformity in the small BAR curve above J=0.54). Efficiency of the candidate propellers increase as the propeller RPM decreases and advance ratio goes up. The diameter is also increasing as the RPM decreases. This is due to the pitch of the blade is increasing to allow the same amount of thrust to be generated at lower RPM. The efficiency also is four to five percent higher when switching to a lower BAR. After looking at the above plot, it is desirable to select a propeller that has a low BAR, large diameter, and operates at low RPM's. Outside these ideal values will result in a loss in maximum attainable efficiency.

OpenProp takes the input chord distribution and adjusts the angle at which each propeller section is pitched along the blade to result in a correct amount of thrust, circulation strength. Most propellers are advertised by their pitch to diameter ratio, P/D, at 75% r/R. The P/D ratio is not given in the parametric analysis, but is given in the single propeller design part of the program, so each blade was analyzed individually to find the respective P/D for each of the propellers shown in the figure above.

To aid in the selection process these values are then plotted against each other for small, medium, and large BAR's. These can be seen below:

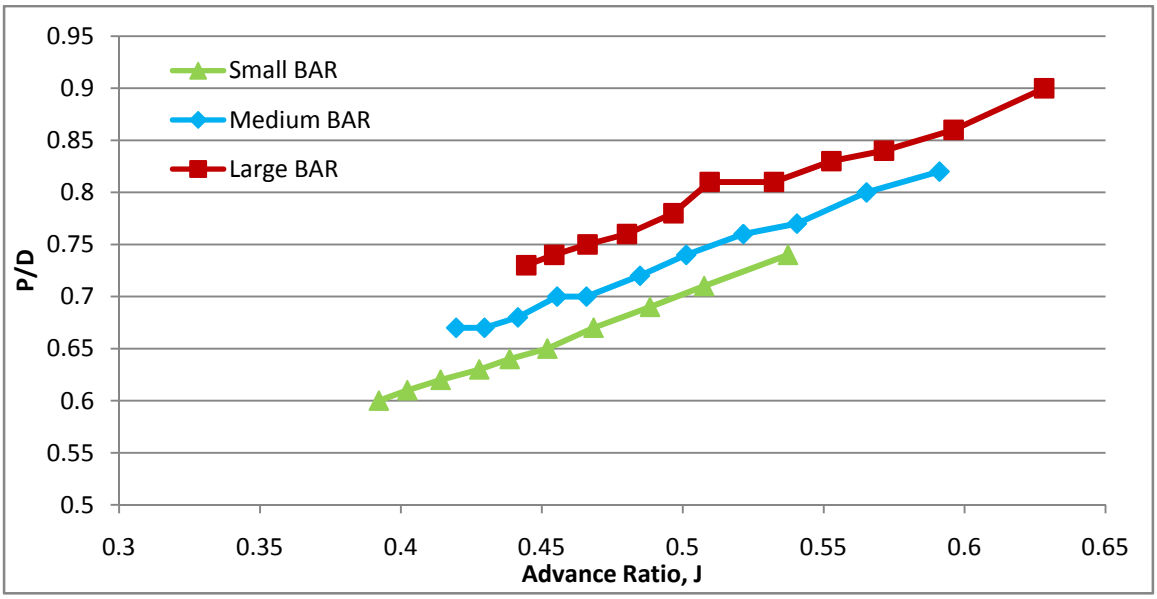

Figure 4-8: P/D vs. J for small, medium, and large BAR's

The above figure shows that as BAR increases the P/D ratio increases as well (See Appendix A for tabulated results). Comparing Figure 4-7 and Figure 4-8 reveals that an efficient propeller is a propeller that is large in diameter with a small BAR spinning at lower RPM's and having a larger pitch.

After exploring the commercial world of RC planes, boats, and submarine propellers with the guidelines for an efficient propeller, it was found that the propellers with low BAR were mainly designed for airplanes or low quality toys. When the proper P/D was found, the diameter was usually too large. This greatly limited the number of propeller choices. After more searching, there were a couple of propellers that met the BAR, P/D, and diameter, but under load the design of the propeller was proven not able to handle the thrust requirements and still maintain shape. Since custom fabrication is not available for this analysis and commercial low BAR propellers don't meet the requirements, it was then decided to search the medium BAR design space. In the RC world, this area is not a desirable area for marine applications because generally consumers want their vehicles to go fast. A large amount of thrust is required to go fast, so a high BAR is usually chosen to keep the diameter down and reduce cavitation. Medium BAR's for airplanes are designed for large motors and in turn larger planes to carry the heavier cargo, and therefore are usually designed for larger diameter. This left a few propellers in our design space and most of them were eliminated due to the number of blades. A propeller was finally selected that was close to the Medium BAR requirements. The propeller is an Octura 0977 which designates 0.9 P/D ratio with a 77mm diameter.

4.2 - Propeller Testing

The performance characteristics of the Octura 0977 are not given experimentally or theoretically when purchasing this propeller, so experimental tests on this propeller are required to

evaluate if the propeller meets the desired output. The experimental testing of these propellers was done using a propeller test rig designed to test small propellers in a wind tunnel (see previous section for details). The result of the uncertainty analysis revealed that the largest uncertainty comes from the primary measurement of torque and thrust, meaning the torque sensor and the load cell. The uncertainty in advance ratio, J, is 0.5%, the uncertainty in thrust coefficient, K_T, is 1%, and the uncertainty in torque coefficient, K_Q, is 1.5%. The resultant uncertainty in efficiency is 2%. The full uncertainty analysis of the propeller system can be seen in Appendix B.

To properly evaluate the accuracy, precision, and repeatability of this rig, a propeller of somewhat known characteristics was placed on the rig and compared to experimental data taken from water tunnel testing done here at Virginia Tech [24]. The propeller chosen to compare to is an Octura 1462 propeller. The expanded blade area dimensions of this propeller and cord distribution can be seen below (see Appendix C for numerical values):

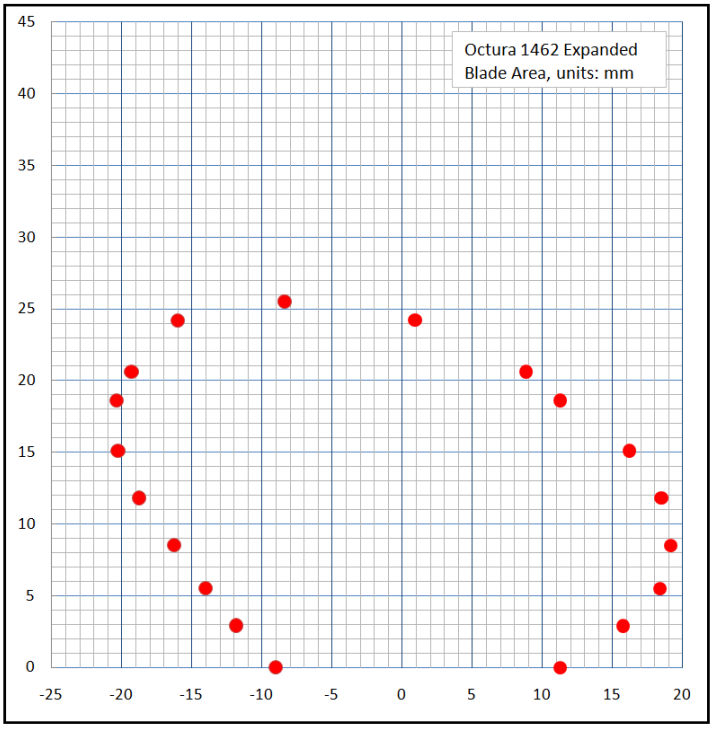

Figure 4-9: Dimensional Expanded Blade Area of Octura 1462

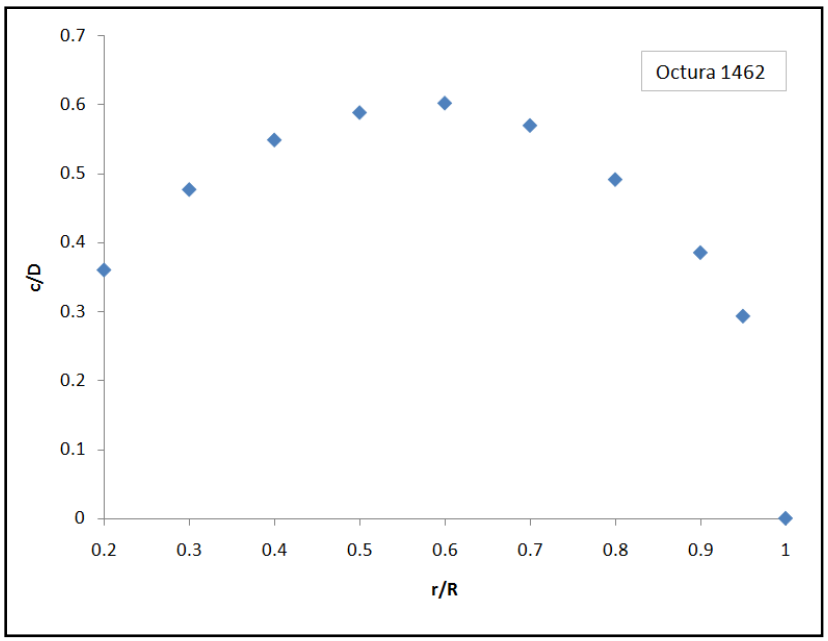

Figure 4-10: Dimensionless cord distribution of Octura 1462

The data in Figure 4-9 and Figure 4-10 was obtained by taking a malleable material and forming to the expanded blade area. The material was then carefully removed and the dimensions of the blade were measured.

The unrefined propeller test data obtained from this propeller can be seen below:

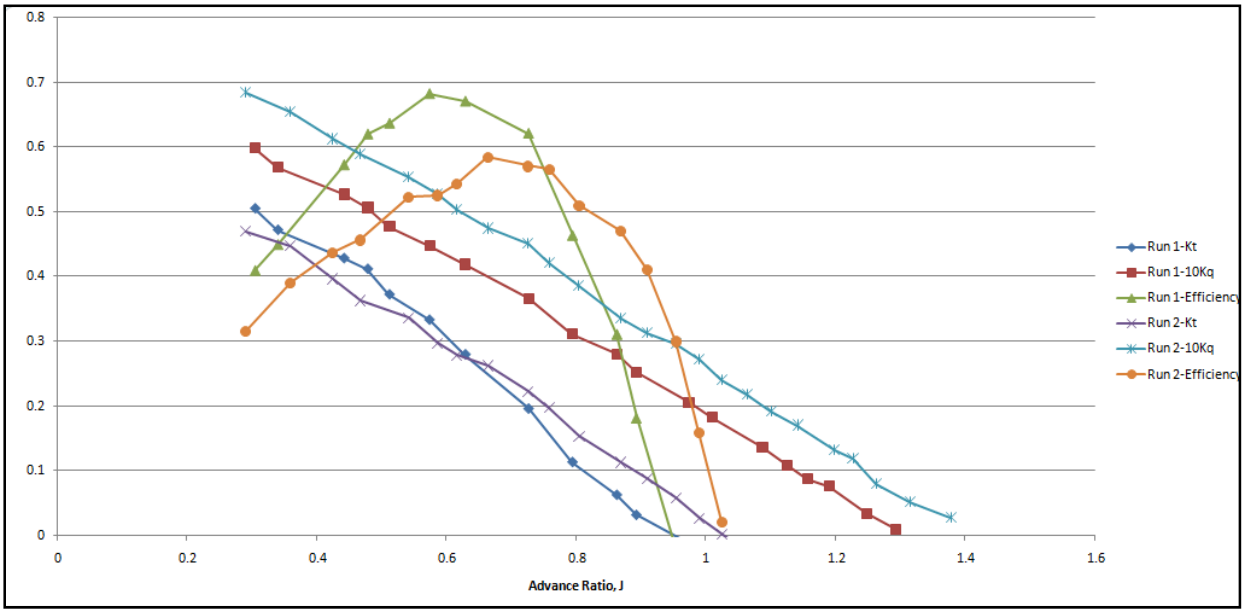

Figure 4-11: Unrefined Octura 1462 propeller data

The results of testing the Octura 1462 propeller appear to give significant variation between run 1 and run 2. One issue with testing in air is the thrust and torque values associated with small propellers

are very small. To get larger thrust and torque values, the propeller is required to operate at high RPM's. The measured torque range of the data above is from 0-0.4 in-oz, which is only 2% of the torque sensors range, meaning the slightest hysteresis or instrumentation drift would shift the curve up or down significantly. This is a major concern and many runs and hours testing were taken to remove this error. The best method to remove the torque error was to run the shaft at the RPM in which testing was to take place and then zero the unit. The logic is that when the sensor comes to a rest, induced bearing torque and motor torque can work together to create a false zero, again this is very important to remove as best as possible. This error can be seen more clearly below:

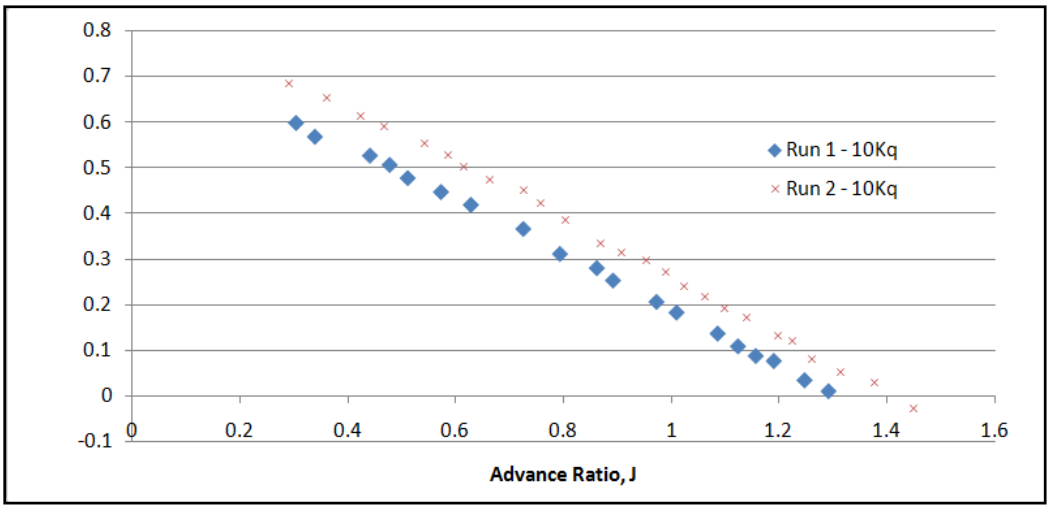

Figure 4-12: Torque sensor drift

The error shown above is due to +/- 0.02 in-oz, which is very small and is likely due to instrumentation drift. It can be seen that the two data sets are of very similar slope, but different zero value, so the values were shifted up and down to overlap and was credited to sensor drift. A future suggestion for the propeller rig is a torque sensor with a smaller range. The result of this shift can be seen below:

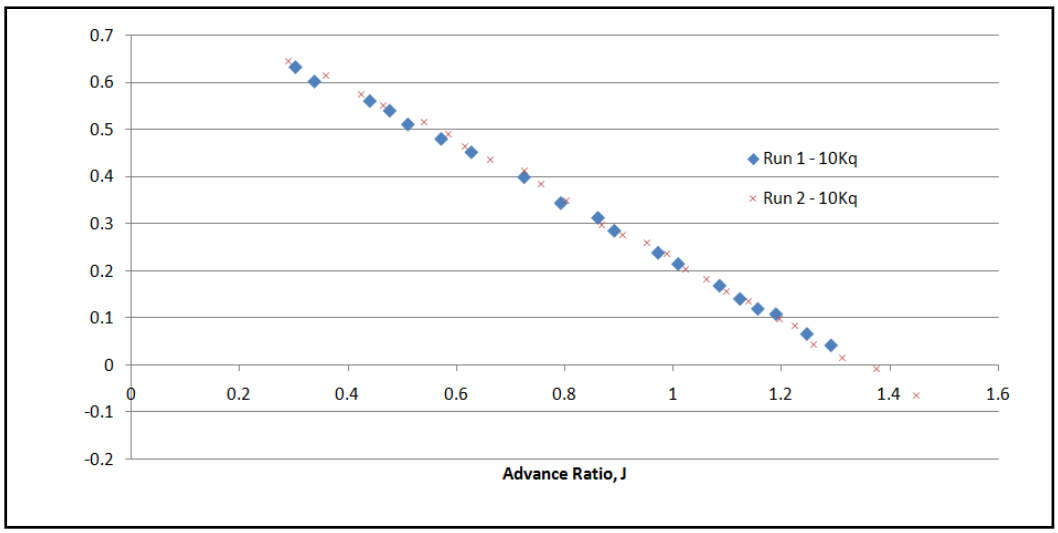

Figure 4-13: Adjusted torque sensor drift

The thrust sensor is within its range for testing this propeller, but it has other unique errors to remove and or comment on in order to achieve good data. One style of error can stem from a non-uniform flow from the tunnel that causes positive or negative lift on the outer shaft tube (shaft tube is directly coupled with thrust sensor, see Figure 3-10). This error can be amplified if the propeller rig and stand are not level. This error may appear by a gradual increase or decrease in the Kt curve as J increases and will look like a small hill or valley that is randomly placed on the curve. The second style of error could come from a linear bearing becoming obstructed by dirt, grease build-up, or a flat spot on one of the bearings. This will present itself as a jump or discontinuity in the Kt curve. Third type of error noticed is propeller rig vibration. The propeller, torque sensor internals, and propeller shafting need to be balanced very well to spin at the high RPM's tested here. The result of imbalance is large vibration amplitude occurring in the thrust sensor signal. Effort was placed into reducing the vibration of the torque sensor and propeller but a noticeable vibration from the rig was still present. Most of the vibration was able to be removed digitally by a low-pass filter. Another source of vibration came from the test floor of the tunnel; this was due to the tunnel motor vibrating and being transmitted through the testing floor. The tunnel test area and tunnel are connected as one unit so the motor vibration is transferred into the thrust sensor directly and is very evidently in the thrust signal readings, on the order of +/- 150 to 200 grams, depending on the frequency of the propeller spinning inside the tunnel.

Errors such as these are unfortunate and can cost the experimenter much time testing to record a good run. The vibration of both the rig and tunnel can be damped out using a low-pass filter assuming the vibration is within the range of the sensor. The error due to bearing obstruction and lift on the tube are quite obvious and can be slightly corrected, but mainly it is useful to see more clearly the error and note it. In Figure 4-11 you may be able to see some of this wavy trend and the jump in Run 1 of K_T; notice how it goes above and below the Run 2 trend, but still maintains a mean trend. Also note that data is missing between the advance ratio of 1 and 1.15, this was due to a jump in thrust, which most likely indicated a bearing obstruction.

After removing statistical outliers and shifting to "fix" drift, the data was reduced to fit a series of curves listed below:

$$K_T = -0.6545 * J + 0.6893 \qquad [0.3 \leq J \leq 1.1]$$

$$10K_Q = -0.615 * J + 0.8357 \qquad [0.3 \leq J \leq 1.4]$$

The thrust coefficient and torque coefficient regression resulted in a R^2 value of 0.995 and 0.998 respectively. The regressed curve fit results of running this test are shown below:

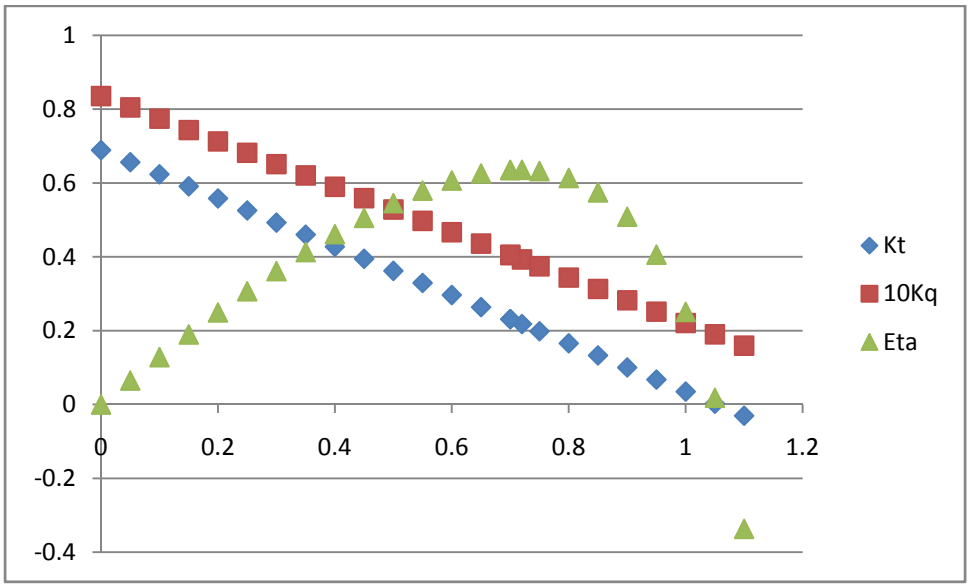

Figure 4-14: Regressed Octura 1462 propeller performance curves

The propeller test resulted in a P/D of 1.053 and a max efficiency of 0.636 at an advance ratio of 0.72. The P/D is obtained when the thrust goes to zero. This is due to the rotational velocity vector and inflow velocity vector summing to equal a velocity vector that is equal to the pitch angle and magnitude of the propeller blade.

4.3 – Jacobson Comparison

Jessica Jacobson, a recent graduate of Virginia Tech, produced some propeller performance curves using the same Octura 1462 propeller. Her testing was done in a water tunnel instead of air. The focus of her research was on contra-rotational propellers, but single propeller analysis was also done [24]. Her results from the Octura 1462 propeller are seen below:

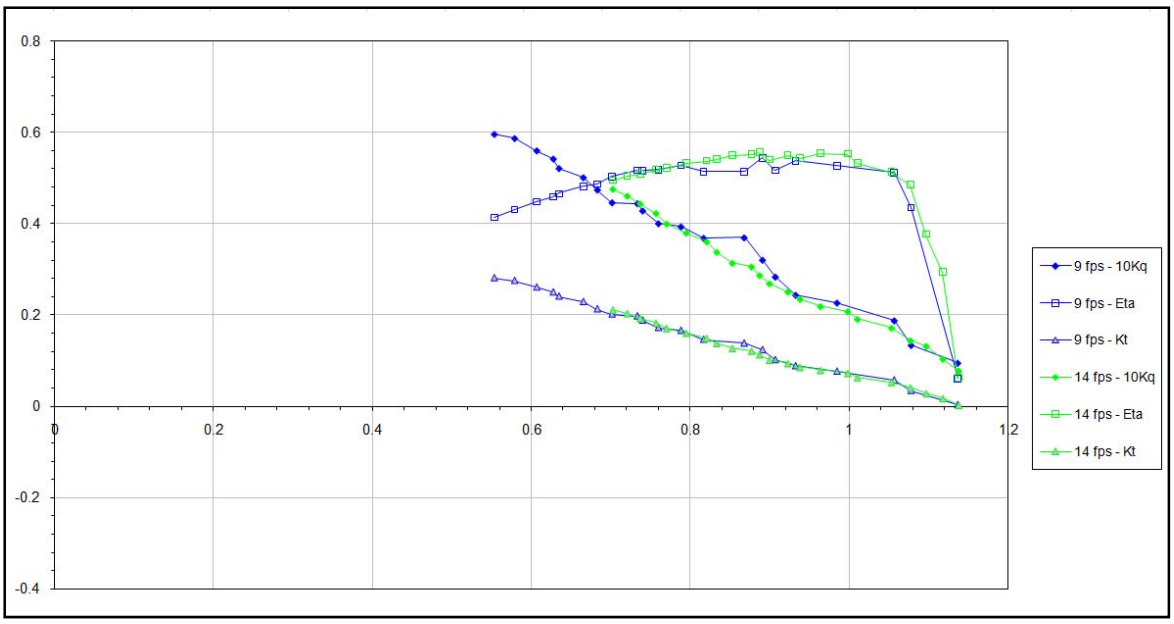

Figure 4-15: Water tunnel testing of Octura 1462 [24]

The result of the data above is a maximum efficiency of about 0.56 at J = 0.9 and P/D occurring at 1.14. These values are different than what was attained in the wind tunnel test. A comparison of the wind tunnel and water tunnel K_T and $10K_Q$ curves can be seen below:

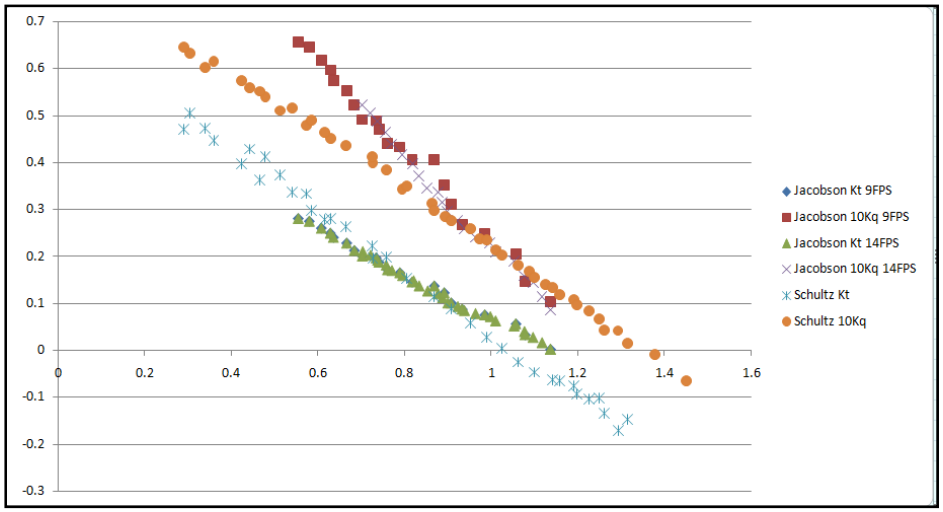

Figure 4-16: Water-tunnel and Wind-tunnel propeller performance data

The above figure shows a comparison between Jacobson's tests and the wind-tunnel tests. The data of Jacobson is much cleaner and closer together, indicating a more stable/precise signal. When comparing the water tunnel to wind tunnel, the thrust and torque appear to have consistently different slopes. When the slopes are adjusted to match each other, the J value appears to be shifted. Under these observations, a number of issues could have occurred in wind-tunnel testing or Jacobson's data. The RPM, flow speed, thrust, and torque voltage to unit calibration multiplier could be off or the zeroing

of each sensor could be off. This could be a combination of both sets of data not in calibration or just one. The precision of Jacobson's data appears to be better, but this doesn't mean it is more accurate. If our data agreed, then the rig created for the wind tunnel would more than likely be accurate. Since they don't, an OpenProp evaluation may make it more clear which set of data matches closer to the expected values.

OpenProp has the capability to run a single propeller design. The single propeller design requires the number of blades, RPM, propeller diameter, thrust required, velocity of vehicle, and radial chord distribution (c/D) as seen below:

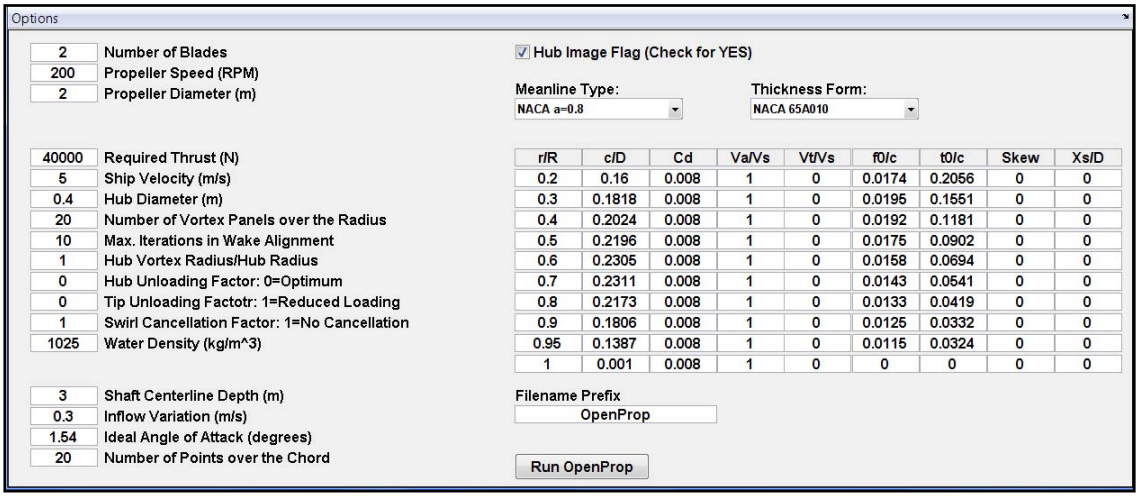

Figure 4-17: OpenProp single propeller design input screen

Using the geometry of the Octura 1462 propeller blade and the non-dimensional propeller performance values from water-tunnel and wind-tunnel testing, a theoretical propeller design can be optimized in OpenProp. OpenProp takes expanded propeller blade area and breaks it into incremental sections along the blade. Each section is adjusted to give the proper thrust required at the RPM and vehicle velocity required. The result is an optimized propeller blade. An optimized propeller blade example can be seen below:

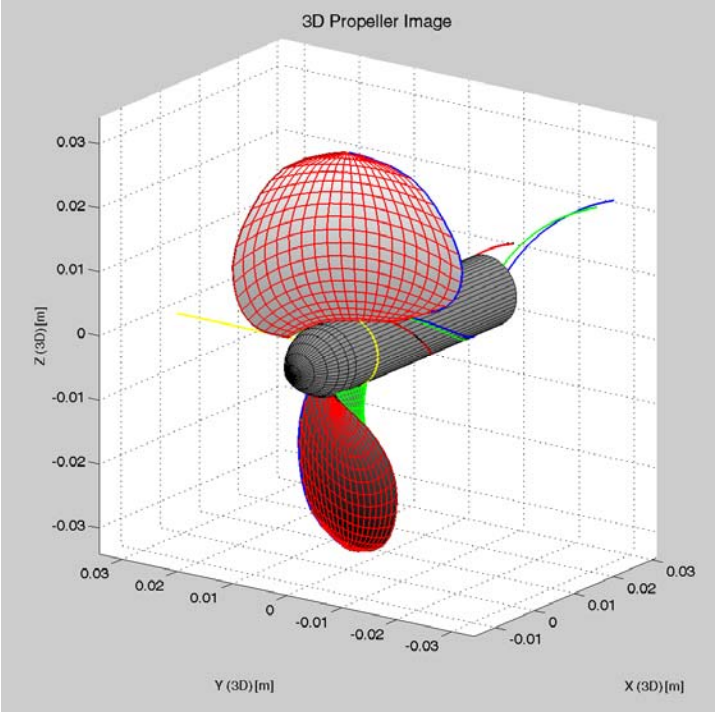

Figure 4-18: OpenProp optimized propeller geometry example

The geometric quantities of the Octura 1462 propeller are: two blades, 62mm diameter, 11mm hub diameter, and the radial chord distribution (seen in Figure 4-10). OpenProp requests other quantities such a skew, shaft center line, thickness form, and many others, but these values were left to the preset values. Since OpenProp designs an optimized propeller blade the experimental max efficiency values of advance ratio and thrust coefficient of the water tunnel and wind tunnel tests can be used. Using the advance ratio at experimental max efficiency, a vehicle velocity and RPM can be chosen to match. These values are arbitrary as long as the advance ratio value matches. Using the thrust coefficient at experimental max efficiency and the RPM chosen to match the advance ratio at experimental max efficiency a thrust value can be obtained. The results using the values of the water tunnel and wind tunnel are tabulated below:

Table 1: OpenProp comparison to experimental data

	Water Tunnel	Wind Tunnel
J @max eff	0.90	0.72
Kt @max eff	0.114	0.218
10Kq @max eff	0.292	0.393
η(experimental)	0.559	0.636
η(OpenProp)	0.721	0.612
% Diff (η_{exp} / η_{OP})	29	3.8

Using the data above and OpenProp, it appears that the wind tunnel data is about 3.8% off from the predicted. The precision of Jacobson's data is clearly better, but the data taken from the wind tunnel

appears to agree better with the theoretical maximum efficiency of OpenProp. There are many factors that weigh heavily into producing good propeller data experimentally, and it can't be conclusively stated that the data that comes from the wind-tunnel propeller rig is correct. It can be stated, from me, that much time was spent to get the calibration of the RPM, torque, and thrust sensors correct since they are highly sensitive and very important. The differences shouldn't be neglected and more testing should be done with the wind-tunnel rig, but due to time constraints and the wind-tunnel being removed, no further testing could be done.

4.4 – Candidate propeller testing, Octura 0977

The Octura 0977 is the candidate propeller chosen from the propeller selection process because of its commercial availability and its estimated efficiency. The Octura 0977 propeller is proposed to produce a good efficiency, but experimental testing was done to validate the proposed solution. The propeller expanded blade area and cord distribution can be seen below:

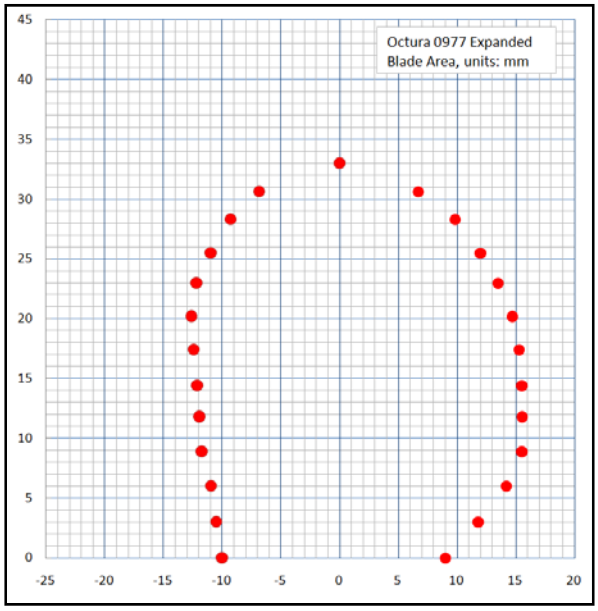

Figure 4-19: Dimensional Expanded Blade Area of Octura 0977

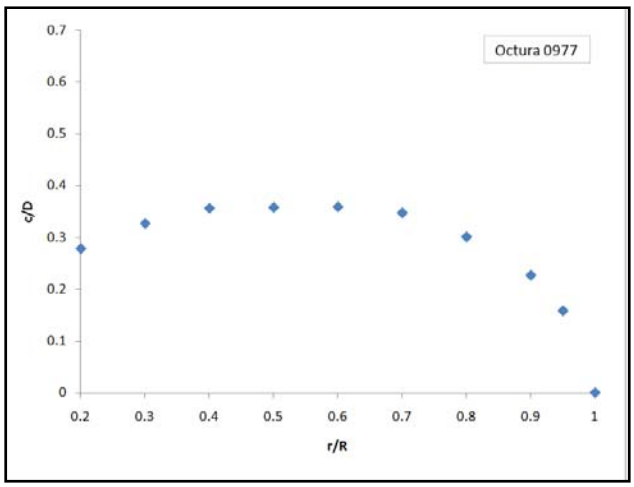

Figure 4-20: Dimensionless cord distribution of Octura 0977

The expanded blade area of the Octura 0977 is almost the exact area as the 1462; with the Octura 1462 at 769 mm^2 and the Octura 0977 at 762 mm^2. The area is almost the same, but the radial chord distribution along the blade and diameter is different. The Octura 0977 has a BAR of 0.33 while the Octura 1462 has a BAR of 0.505. The blade area was obtained by using composite trapezoidal integration. The measured points can be seen in Appendix C. The raw data obtained from experimentally testing the Octura 0977 can be seen below:

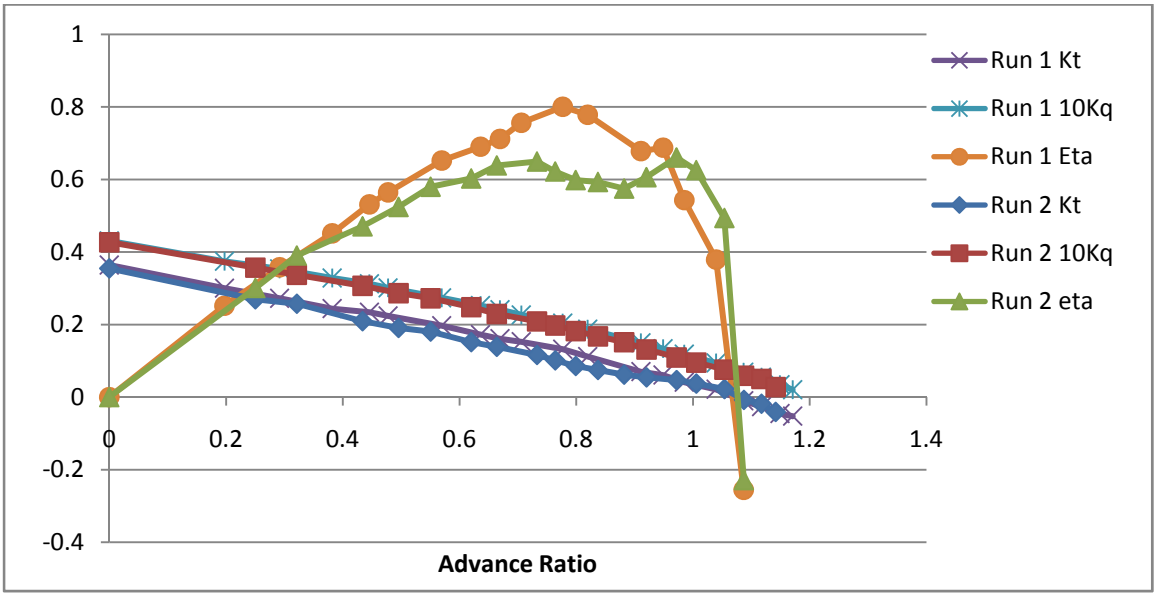

Figure 4-21: Octura 0977 experimental propeller performance data

The figure above shows two runs using the Octura 0977 propeller blade. The propeller performance curves appear to be closely related for K_T and $10K_Q$. There appears to be a bearing obstruction error in Run 2 of K_T causing the curve to shift down and then back onto the mean K_T curve. This shows up in the efficiency curve between an advance ratio of 0.4 to around 1. The above propeller

performance curves are regressed using a linear trend for the K_T and a 2nd order polynomial for the $10K_Q$ curve, resulting in:

$$K_T = -.3306 * J + .366 \qquad [0 \leq J \leq 1.1]$$

$$10K_Q = -0.1126 * J^2 - 0.2071 * J + 0.4325 \qquad [0 \leq J \leq 1.2]$$

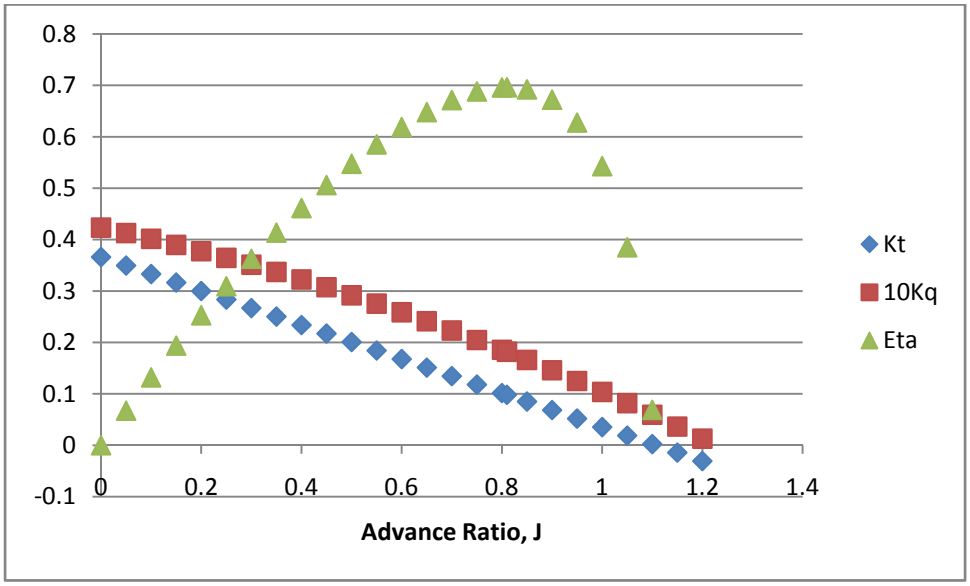

Figure 4-22: Regressed Octura 0977 Propeller Performance Curves

The propeller appears to have a P/D of 1.11 and a max efficiency of 0.696 at J = 0.81. The ideal efficiency is 0.796 using the momentum theory analysis of an actuator disk.

Chapter 5 – Motor Selection Guidelines

Motor selection requires an adequate understanding between the various types of motors available: AC induction, AC synchronous, stepper DC, and brushless DC are of the most common. Brushless direct current (BLDC) motors offer higher efficiency and reliability, noise reduction, longer lifetime (no brush erosion), no ionizing sparks, and overall reduction of electromagnetic interference (EMI) [25] as compared to the others types of electric motors. The negative of BLDC's is their initial cost. A brushless, electrically commutated, direct current motor was selected despite the initial cost. There are two main components to a BLDC motor; permanent magnets and electromagnets. The permanent magnets rotate in a housing attached to the motor shaft called a rotor. The electro magnets are made of iron arms with wrapped copper wire and stay stationary on a piece called the stator. To get the shaft to rotate, the electromagnets are switched on and off at proper times to allow the permanent magnets to either attract or repel the electromagnets.

Hobbyists have used BLDC motors for many years and there are many options of size and power ratings available. You can select the number of windings, pole strength, inner and outer rotor, number of teeth, number of phases and much more.

The first design criterion analyzed in this report is a comparison between outer rotor and inner rotor BLDC motors. An outer rotor motor consists of a free spinning bell-housing where permanent magnets are mounted on the inside and a small gap is left between the rotor and stator. The permanent magnets alternated positive to negative around the rotor. The stator consists of wire wound around iron armatures to create an electromagnet. An inner rotor design is the opposite; the permanent magnets are located inside the electromagnets. A general comparison can be seen in the two tables below:

Table 2: Comparison of Outer-Rotor and Inner-Rotor Motors [26]

Outer Rotor	**Inner Rotor**
Greater rotor inertia	Lower rotor inertia
Less torque perturbation	More torque perturbation
Slower acceleration	Fast acceleration
Lower-energy magnets can be used	Higher energy magnets required

Table 3: Inner-Rotor versus Outer-Rotor Motor Applications [26]

Requirement	Inner rotor	Outer rotor
Rapid acceleration	Very good	Poor
Heat dissipation	Very good	Poor
Low cogging	Okay	Good
Pump application	Okay	Good
Disk-drive application	Okay	Very Good
Fan application	Poor	Very Good
High side load	Good	Poor
Use with speed reducers	Good	Poor to okay
Reversible	Very good	poor

For our application it was decided to use an outer rotor BLDC motor because of higher rotor inertia and less torque perturbation. An advantage, not mentioned in the tables above, is greater amounts of torque can be generated from outer rotor designs. The inner rotor can spin faster than an outer rotor, but its torque is limited due to the moment arm offered from the stator to rotor distance. See figure below for this principle:

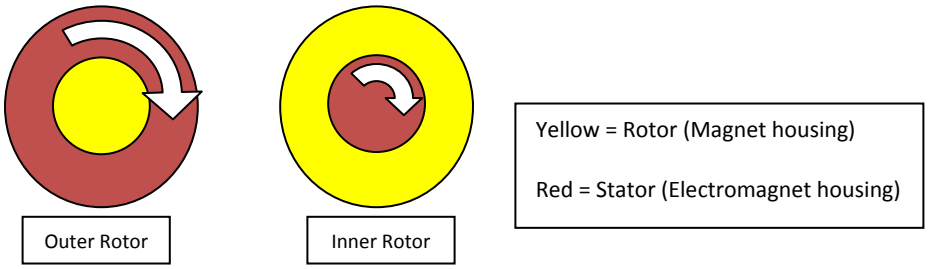

Figure 5-1: Inner and Outer Rotor Concept

The next motor criterion evaluated is the number of phases, teeth, and poles. A phase on a BLDC motor represents the channel in which an electromagnetic is switch on and off. A single-phase motor only has one channel to switch on and off, meaning it has to rely on inertial to get it started. A two-phase motor and above has two channels of electromagnets it can switch between to alternate the electromagnetic switching. Three-phase has three channels and so forth. Single-phase motors have poor conductor utilization, high torque ripple, and null zones that may create starting problems, but they are easy to wind and low cost and require only one or two power switches. Two-phase motors also have poor conductor utilization, but the null zones are eliminated, the torque ripple is greatly reduced, and the cost is higher because a minimum of four power switches are required. Three-phase motors have better conductor utilization, no starting problems, and greatly reduced torque ripple; they can get by with as few as three power switches, but they generally cost more to wind. Increasing the number of phases to four or greater realizes small gains in copper utilization and torque ripple and the cost of winding and power switches usually outweigh the gains. A three phase motor was selected for this thesis.

The number of teeth on a stator represents the number of electromagnets available to switch between. The number of poles represents the number of permanent magnets. A simplified chart for increasing/decreasing the number of poles, teeth, and phases can be seen in the table below for these effects:

Table 4: Effects of Changing Number of Poles, Teeth, and Phases [26]

	Effect on design factors				
Change	Cogging	Speed	Torque	Active material utilization	cost
Number of Poles					
Increased	Decreases	Decreases	Increases	Increases	Increases
Decreased	Increases	Increases	Decreases	Decreases	Decreases
Number of Teeth					
Increased	Decreases	No change	No change	Increases	Increases
Decreased	Increases	No change	No change	Decreases	Decreases
Number of phases					
Increased	Decreases	No change	No change	Increases	Increases
Decreased	Increases	No change	No change	Decreases	Decreases

The physical size of the motor is generally representative of the power it can produce. A larger motor should produce a greater amount of power. The physical size is also representative of the efficiency it produces, see table below:

Table 5: Electric motor assumed efficiencies based on motor diameter [26]

Motor diameter, in	Assumed efficiency
<2.0	65%
2.0-4.0	75%
>4.0	85%

As the size of the motor increases, the efficiency goes up. Over the last eight years the demand for remote control (RC) BLDC's (thanks in majority to airplane hobbyists) has forced motors to become more powerful, efficient, lighter, and smaller in size. The efficiency of some of the RC motors is on the order of 80% to 85% efficient at its peak with a diameter of less than two inches.

Other factors in BLDC motors include: winding style, wire thickness, bearing type, wire termination, number of wraps on a stator arm, and much more. We can see in the table below that the loss associated with the amount of current carried across the wires and resistance of the wire make up an estimated 65% of the overall loss. So choosing the right wire setup is essential.

Table 6: Proposed proportion of electric motor losses [26]

I^2R	65%
Friction and winding	20%
Iron	10%
Stray load	5%

There are multiple ways to wind a motor as well as terminate the wires. The depth of this subject is much larger than being discussed here, but some basic principle will be highlighted. The first style of wire termination is called a Star or Wye ('Y') termination. The Star style of termination connects each phase of wires in series with one another and the circuit diagram looks like a 'Y', hence the name. The second style is called a Delta termination. The Delta style of termination connects each phase of wires in parallel and the circuit diagram looks like the Greek symbol Δ.

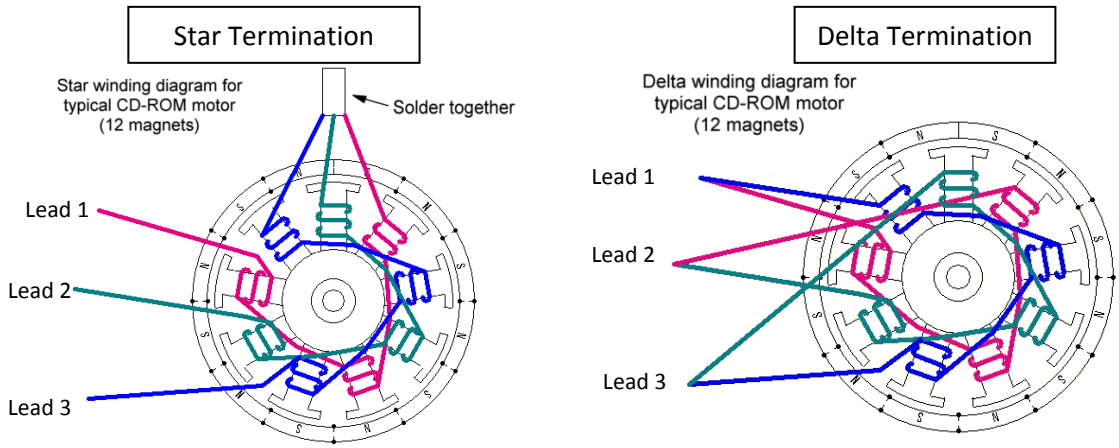

Figure 5-2: Winding Terminations [27]

The above figure can be represented by nine resistors, with each resistor representing a stator arm with wire wrapped around it. The figure below shows electrically the resistors as forming a Y or Δ.

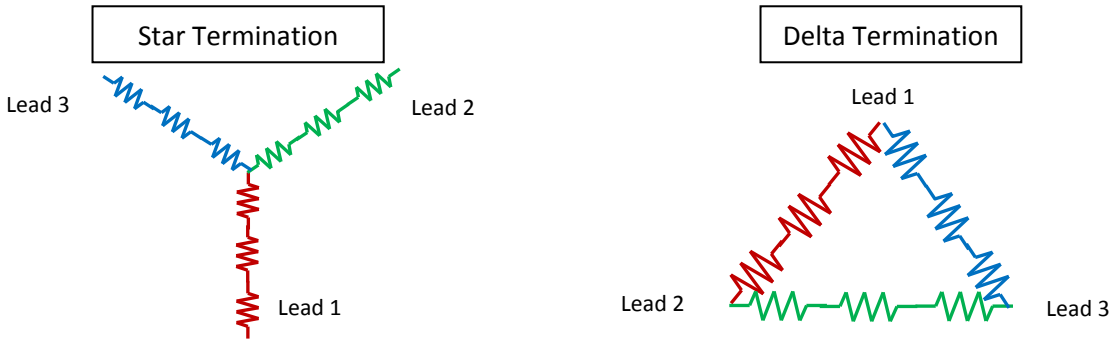

Figure 5-3: Winding Terminations (Electrically)

Depending on the termination style chosen, a motor will have a higher or lower total resistance. As with resistors in series (Star termination), you will get a higher resistance as you travel from lead to lead. The resistance of a star termination is 3 times larger than that of the delta termination. This higher resistance relates to 1.73 times slower than the delta termination. Since the desired design is a low RPM high torque motor, a star termination was choose as our ideal termination.

The way a motor is wound affects the amount of torque and rpm delivered to the propeller. A good wiring diagram listing some possible ways to wire up 3, 6, 9, 12, 15, and 18 teeth stators with

either 2, 4, 6, 8, 10, 12, 14,16, or 20 magnets and their respective electrical reduction gearing can be seen below:

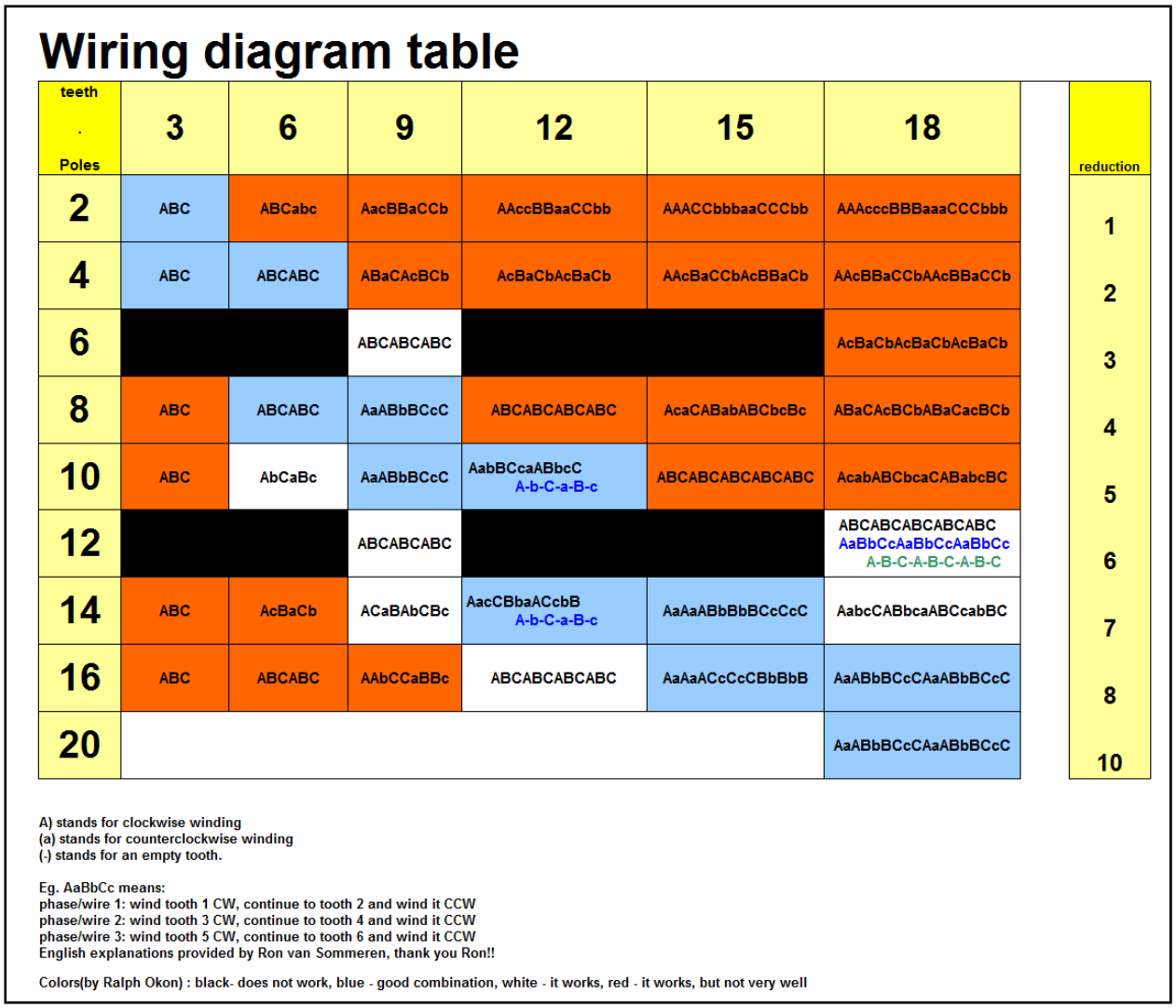

Wiring diagram table

teeth . Poles	3	6	9	12	15	18	reduction
2	ABC	ABCabc	AacBBaCCb	AAccBBaaCCbb	AAACCbbbaaCCCbb	AAAcccBBBaaaCCCbbb	1
4	ABC	ABCABC	ABaCAcBCb	AcBaCbAcBaCb	AAcBaCCbAcBBaCb	AAcBBaCCbAAcBBaCCb	2
6			ABCABCABC			AcBaCbAcBaCbAcBaCb	3
8	ABC	ABCABC	AaABbBCcC	ABCABCABCABC	AcaCABabABCbcBc	ABaCAcBCbABaCacBCb	4
10	ABC	AbCaBc	AaABbBCcC	AabBCcaABbcC A-b-C-a-B-c	ABCABCABCABCABC	AcabABCbcaCABabcBC	5
12			ABCABCABC			ABCABCABCABCABC AaBbCcAaBbCcAaBbCc A-B-C-A-B-C-A-B-C	6
14	ABC	AcBaCb	ACaBAbCBc	AacCBbaACcbB A-b-C-a-B-c	AaAaABbBbBCcCcC	AabcCABbcaABCcabBC	7
16	ABC	ABCABC	AAbCCaBBc	ABCABCABCABC	AaAaACcCcCBbBbB	AaABbBCcCAaABbBCcC	8
20						AaABbBCcCAaABbBCcC	10

A) stands for clockwise winding
(a) stands for counterclockwise winding
(-) stands for an empty tooth.

Eg. AaBbCc means:
phase/wire 1: wind tooth 1 CW, continue to tooth 2 and wind it CCW
phase/wire 2: wind tooth 3 CW, continue to tooth 4 and wind it CCW
phase/wire 3: wind tooth 5 CW, continue to tooth 6 and wind it CCW
English explanations provided by Ron van Sommeren, thank you Ron!!

Colors(by Ralph Okon) : black- does not work, blue - good combination, white - it works, red - it works, but not very well

Figure 5-4: Tested wiring styles [27]

The wiring styles highlighted in blue are of interest for this research because it has been proven to be a good combination of teeth and poles. The upper and lower-case sign conventions are used to describe the winding direction and the order in which they are wound. There are two styles that are within our range: the standard “CD-ROM” style and LRK. For this evaluation a Distributed LRK (DLRK) was also considered since offers some torque advantages. The CD-ROM is called this due to its use in CD-ROM drives and the LRK stand for the inventors Lucas, Retzbach, and Kühlfuss. The LRK winding style has been given much recognition and has some great advantages that are useful for a high torque, slow spinning motors. The figure below show the ways to wind BLDC motors, please note the winding directions.

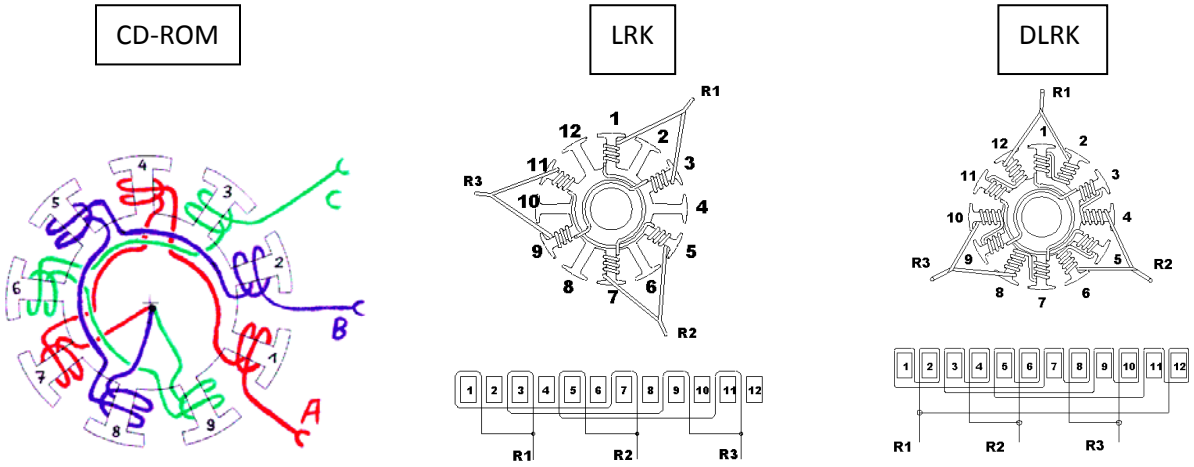

Figure 5-5: Winding Styles [27]

The LRK winding style tries to obtain the highest flux (lines of magnetic force) for a given amount of stator metal and magnetism. The more flux that is available relates to more torque that is available and as a result the RPM gets lower[28]. The internal electrical gearing of the LRK winding style is equal to half the number of magnets in the rotor bell. This reduction allows it to spin slower and have a higher torque compared to CD-ROM style windings. Suppose there are 14 magnets on the rotor then a reduction gear of 7:1 is attained by using a LRK winding style. Not much material was available on the DLRK, since it has only been around for a short while, but based on the wiring diagram above it would appear as if more torque is available through this style because it is wrapping two stator arms instead of one, therefore increasing the magnetic field strength of the electromagnet and in turn decreasing the RPM of the motor. Some data was found to support this understanding and the RPM did decrease but only slightly.

For the standard LRK it is possible to get more winds per arm, since only half the arms are being wound. The number of wraps on each arm is dependent on the quality of wrap being produced by the person/machine wrapping each arm. As the wraps of wire on each arm increases, the magnetic field increases. The limitations to designing an optimized motor are the same for an optimized propeller; the cost and time to custom fabricate this item may not be worthwhile. Using the outlined method above for selecting a motor it is possible to guide a designer to an acceptably efficient motor solution. Some more “rules of thumb” are:

- Doubling the number of windings per stator arm halves the RPM
- Doubling the length of the stator arm halves the RPM
- As the magnetic field increases the RPM goes down
- Increasing the number of permanent magnets decreases the RPM
- 70-75% magnet coverage is ideal, but outside this range the efficiency drops.
- Multiple strands of thin wire should be used instead of one thick wire, since electrons travel along the skin of the wire.

Some common constants to identify motors are:

$$K_V = {}^{RPM}/_{V}$$

$$I_o$$

$$R_m$$

where Kv represents rotation of the shaft per minute (RPM) per volt (V) of the battery stack. The variable I_o represents the current draw to get the motor to start spinning and R_m is the resistance of the motor.

Chapter 6 – Motor testing setup

Some equipment used to test the propellers will be used to test motors as well. The information on these instruments can be found in Chapter 3. The same torque transducer that runs directly to the Motorized Dynamometer Instrument Model 1038 for the propeller testing is used in the testing of motors. The torque transducer used in the motor test rig (see Figure 6-1) has a RPM sensor built in and the RPM sensor from the propeller test rig is not used. The USB 6211 DAQ is also used again, but this time only RPM and torque will be measured. The measurements will again be displayed by a computer using LabVIEW. Voltage and current from the battery to motor controller are measured via a digital readout from a digital meter. The figure below shows the motor test rig setup:

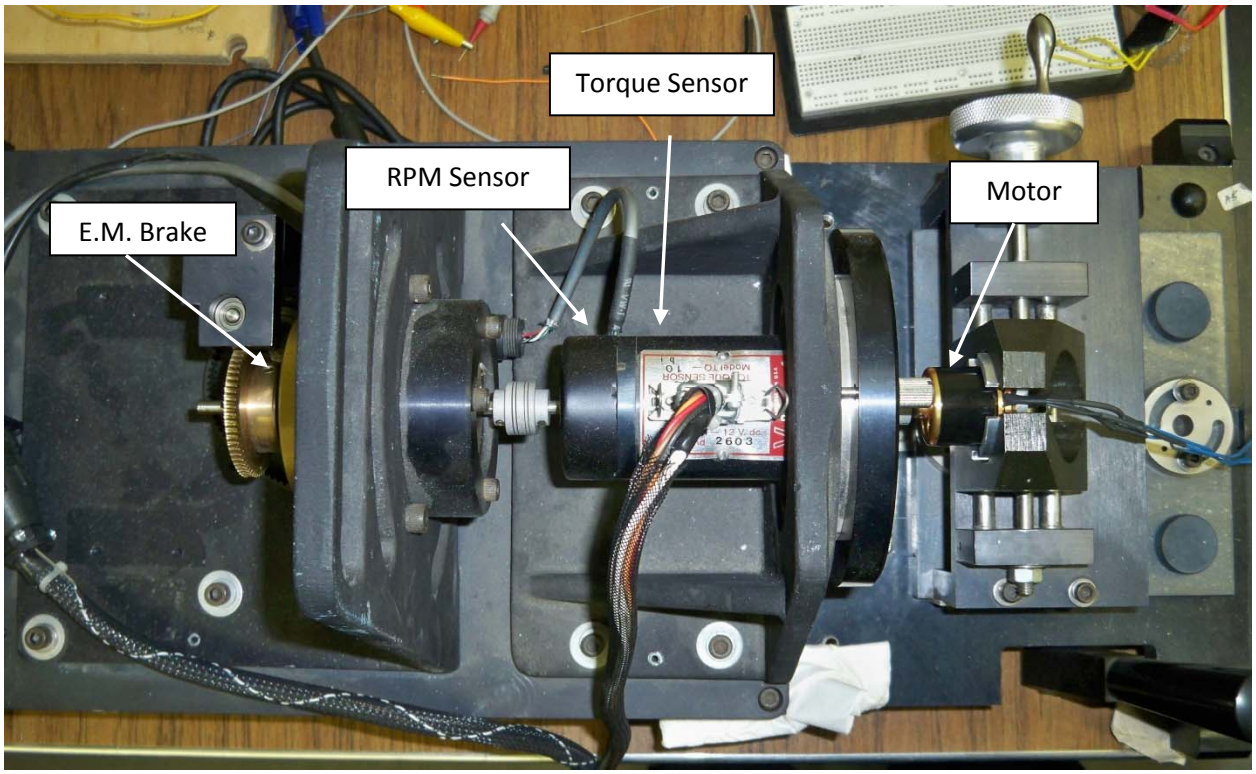

Figure 6-1: Motor Test Rig Setup

6.1 – Torque Tester

A Vibrac Stepper Motor Torque Tester Model STT 3050 was used to test each motor. The main purpose of this system was to be able to apply a variable braking system to the BLDC motor. One side of the torque transducer has the brake being applied, while the motor being tested is on the other side of the torque transducer and is trying to rotate the shaft at the given load. The variable braking system is done by an electromagnetic clutch, which allows for an analog variance in applied torque. The torque sensor was found to be undersized, for the motors tested in this thesis. The motor test rig is designed to test a variety of motor sizes and types. The rig is also able reduce the vibration generated by the instruments using rubber feet. A special housing needed to be made to hold the outer rotor motors because the bell on the outside needs to spin freely. A picture of this setup can be seen in Figure 6-1.

6.2 – Voltage and Current Meter

The voltage and current is measured by a Hyperion E-meter unit. The meter itself is a multipurpose tool for brushless DC motors, specifically Hyperion, but only current and voltage measurements were needed. The E-meter's shunt can measure up to 20A with 1/100A resolution. The data was collected manually instead of through the DAQ unit. A picture of this unit can be seen in Figure 6-2.

Figure 6-2: Hyperion E-meter [29]

Chapter 7 – Motor Evaluation and Testing

There are many ways to design a motor to fit the specification you wish, by changing the wire size, wire terminations, wire scheme, stator length, stator diameter, number of magnets, types of magnets, and so forth. The purpose of this section is not to test all these types of motors, but to test a few select motors and get a better understanding of how an electric motor performs, so a guided motor decision can be made. Four motors were tested to give guidance:

Table 7: Motor Constants of Motors Tested

	Kv(RPM/V)	Io (A)	Rm(Ohm)	Weight (g)
HP-Z2205-46	1200	0.42	0.245	29.4
HP-Z2209-32	910	0.55	0.181	42.5
HP-Z2213-24	850	0.60	0.135	53.8
Custom	198.5	0.10	2.77	59.2

The values above are specification's given by the manufacture or designer of the motor. Kv is the RPM the motor will spin per volt of the battery, under no load and the motor controller is set to allow full power. Io is the amount of current required to spin the motor under no load. Rm is the resistance of the motor. These specifications, along with other physical details of the motor can give a general understanding of how the motor might perform. The HP-Z2205-46 can be used for a fast spinning propeller since the Kv is high. The motors are controlled by a motor controller or electronic speed controller (ESC). The ESC switches the electromagnets of the stator to positive, negative, or

neutral polarity and depending on where the permanent magnet is located, it will push, pull, or allow the magnet to pass. This process happens very quickly and requires much programming and tuning to get to a controller that will efficiently rotate the motor. Motor controllers come in various sizes, shapes, and functions along with many styles of control. Some ESC use Hall-Effect sensors, other use back electromagnetic force (BEMF) to detect the location of the magnets as they rotate. There are a variety of ways to detect the zero crossing of the BEMF voltage to allow the MOSFET to switch on and off. For the slowest spinning motor possible, a Hall-Effect sensor style ESC is the best way to go, but unfortunately they are not as readily available as the BEMF, since BEMF is compatible with any BLDC motor and doesn't require external hardware. A Hyperion Titan 10A Titan series motor controller was chosen to test these motors with. This ESC operates by receiving a pulse width modulated (PWM) signal and interprets this signal as increasing or decreasing the amount of power given to the motor. This amount of power is regulated by the duration the MOSFET is open or closed, the signal would be a pulse width depending on how much power is required. A typical motor plot would look something like:

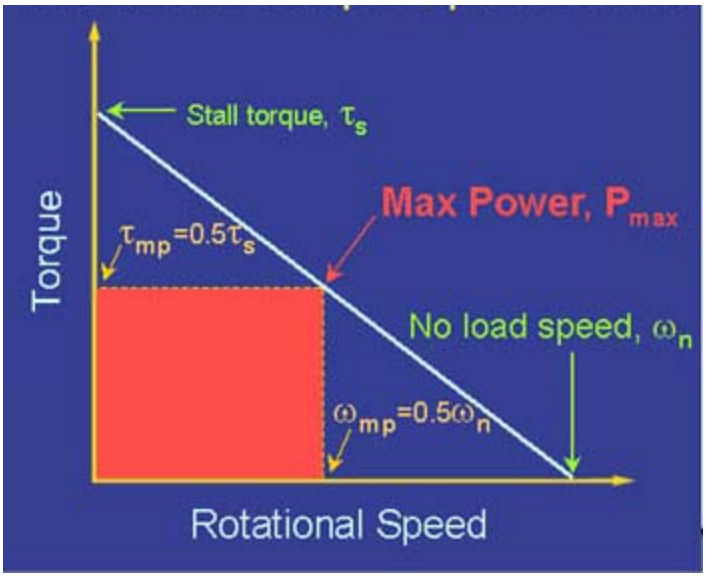

Figure 7-1: DC motor torque/Speed curve[30]

The above figure demonstrates that as torque increases the rotational speed goes down proportionally.

7.1 – PWM performance prediction

The ESC controller allows for different levels of power to be transmitted to the motor. A change in the percent of duty cycle of the signal sent to ESC will change the power transmitted to the motor. The duty cycle of the signal sent to the motor controller is varied from 5 to 10%. The 5 to 10% duty cycle of the signal sent to the motor controller corresponds with 0 to 100% of power transmitted to the motor (though the PWM sent to the ESC may be 8% duty cycle, this may correspond to 100% power transmission). Most servos operate on this language level as well. These different power levels cause the torque to RPM relationship to be nonlinear:

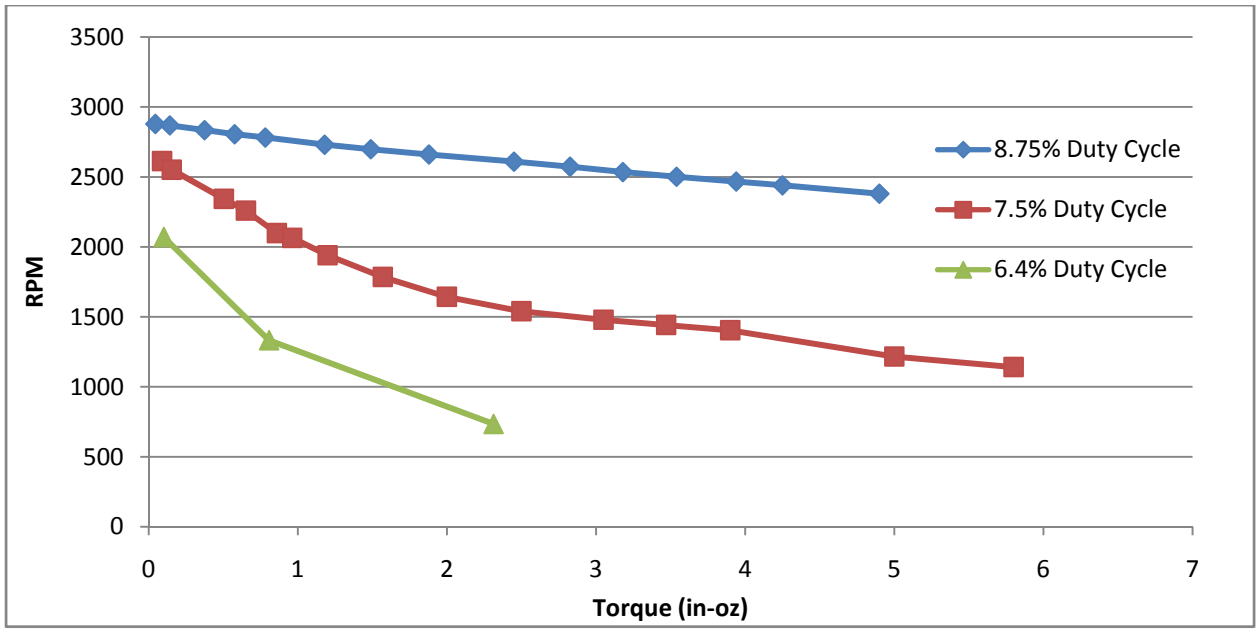

Figure 7-2: RPM as a function of torque with varying Duty Cycle (Custom motor)

The above figure shows how RPM changes as the torque on the motor increases and duty cycle of the signal sent to the motor control is changed. The motor used to demonstrate this concept is the "custom" motor. The data collected from the "custom" for this figure can be found in Appendix D. From Figure 7-2 the slope of the 8.75% duty cycle is constant and follows a typical motor curve, but as you decrease the duty cycle given to the ESC, the slope becomes non-linear.

The motors selected for testing were unable to be tested to their full limits because the electromagnetic brake couldn't provide enough braking resistance. The 8.75% duty cycle curve ideally could be extended out to about 28 in-oz, assuming the motor controller could detect the BEMF zero crossing at such a low value or lose efficiency due to motor heating and if the motor wire could handle such heavy load.

The voltage from the battery to the ESC doesn't change, relative to total voltage, but current draw does. The details of how voltage and current are regulated from the ESC to the motor are not discussed here, but it is understood to be a form of pulse width modulation using the MOSFET's. The effect torque has on current is most of the time stated as being linear; as torque increases, current increases proportionally. This is relatively true for the full power motor state, but off the full power motor state, the shape begins to change:

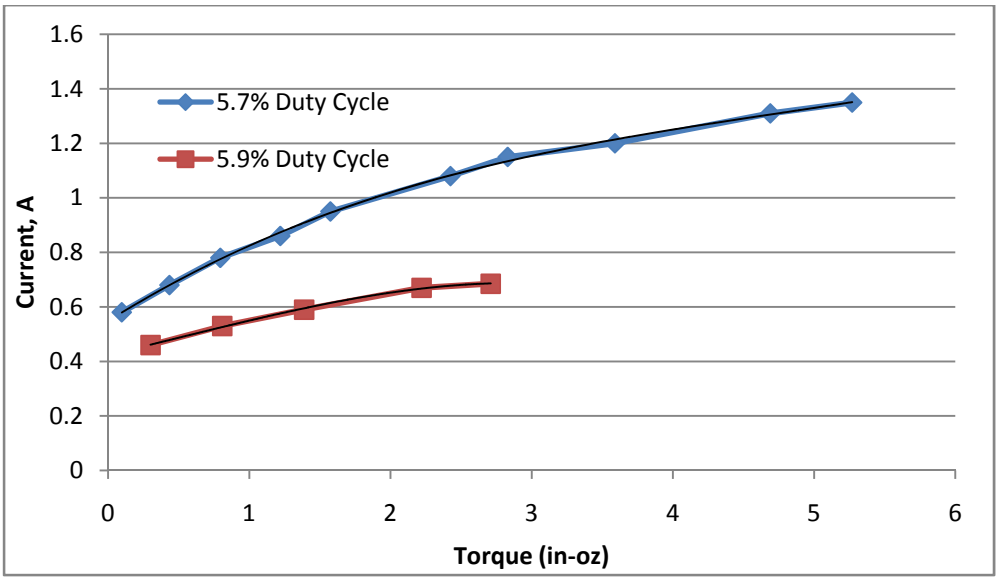

Figure 7-3: Current draw as torque on motor increases and PWN varies (Hyperion Z2213-24)

The above graph shows two cases where duty cycle is not at full load and the current is not proportional to the torque. The motor used to demonstrate this is the Hyperion Z2213-24 motor. The data collected to create the above figure can found in Appendix E. From the above figure it can be seen that the current gets to a point and starts to level off, but torque steadily increases. In this area, where current levels off, the RPM is dropping and the power being output by the motor starts to go down. While the output power starts to drop, the power being input into the motor continues to increase causing the efficiency to drop as well. This is the essence of this report, to find where the power into the motor controller and motor can best be transmitted to power output to the propeller. Using the same values in Appendix E to generate Figure 7-3 an efficiency curve for each PWM phase recognized by the motor controller is generated:

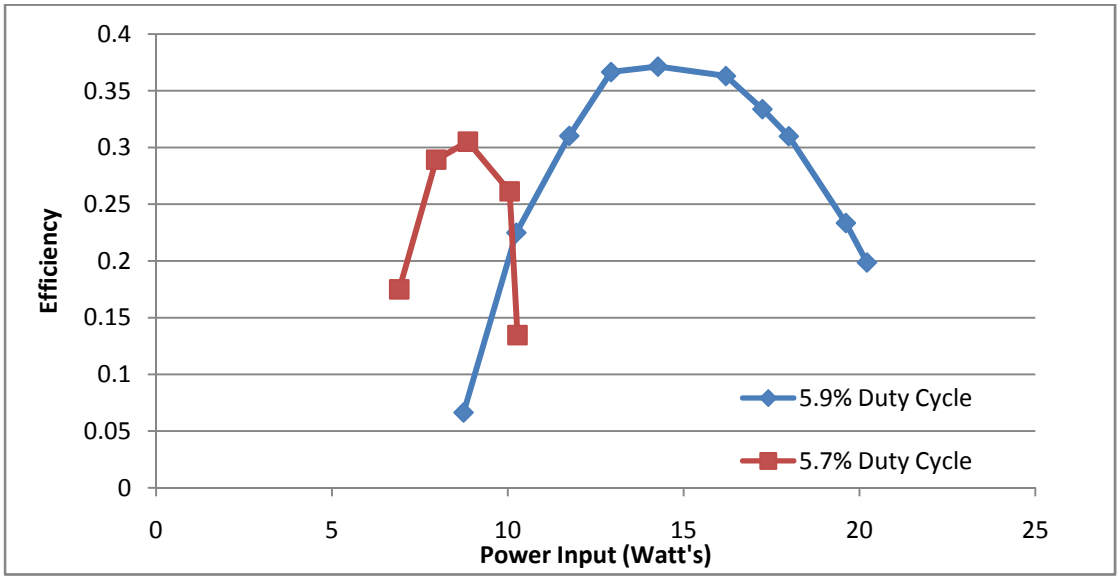

Figure 7-4: Efficiency of power input to motor, duty cycle dependent (Hyperion Z2213-24)

The above figure shows that efficiency has multiple "bands" that the motor can switch between. These bands are dependent upon the PWM signal sent to the motor controller. The motor used to demonstrate this is the Hyperion Z2213-24 motor. Efficiency will change depending on the power being input to the motor as well as the band the ESC is operating on. The above figure shows that at the same power input to the motor, there can be two efficiencies. Also at the same power input to the motor the motor is capable of producing multiple RPM and torque outputs depending on what PWM signal is sent to the motor controller. This makes performance analysis very difficult to predict, since voltage, PWM, and current can all be varied to give different RPM, torque, and efficiency values. To predict these values would require a better knowledge of motors than what will be discussed in this thesis. Though this information could prove to be useful for this report it was decided to use the full power "band", since as duty cycle is increased the maximum efficiency goes up. For this report maximum efficiency is the desired motor output. The bands of efficiency can be seen more clearly using the custom motor since it is able to be tested at full motor power:

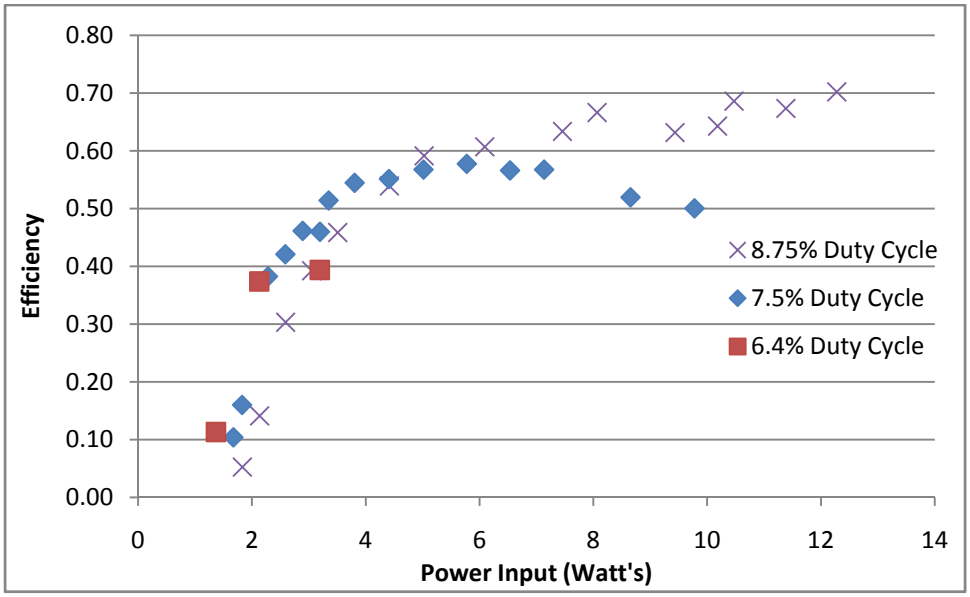

Figure 7-5: Efficiency of power input to motor, duty cycle dependent (Custom motor)

Using the figure above it can be seen that the efficiency curve of the 8.75% duty cycle "band" offers highest efficiency from about 4 Watts and above. The motor used in the above figure is the custom motor. The data collected from the custom motor for this figure can be found in Appendix D. The figure doesn't extend beyond around 12 Watts because of instrumentation limitations.

The evaluation of PWM variation has revealed that as the PWM increases, efficiency increases. The interest of this thesis is to operate in the most efficient region of the propeller and motor. So the uppermost PWM signal into the motor controller will be used to evaluate motor performance. Motor torque and RPM at the uppermost PWM signal into the motor controller can be considered proportional to current; this idea will be elaborated better in the next section.

7.2 – Motor Performance at full duty cycle

It has been proposed by multiple motor forums and articles that the 3 constants listed in Table 7 can be used to predict the performance of electric motors [31]. These "fundamental" motor equations are established by empirical motor results and Ohm's law. These equations can be seen below:

$$RPM = K_V(V - IR_m) \tag{7-1}$$

$$Q = K_q(I - I_o) \tag{7-2}$$

$$I = \left(V - {RPM}/{K_V}\right) \tag{7-3}$$

$$V = \left(I + {RPM}/{K_V}\right) \tag{7-4}$$

where *V* and *I* are the battery voltage and the current draw of the motor. The proposed RPM motor equation states that RPM is proportional to battery voltage minus the voltage drop (due to motor resistance, R_m, and current) multiplied by the constant K_V. The constant K_V usually has units of RPM per volt and the numerator can vary depending on which unit system is preferred. The proposed torque equation states that the torque is proportional to current minus the idle current, I_o, multiplied by the constant K_q. The constant K_q has units of torque per unit of current and the numerator can vary depending on the unit system selected. Using the proposed RPM and torque equations, efficiency can be represented by mechanical power out over electrical work in:

$$\eta_m = \frac{P_{out}}{P_{in}} = \frac{2\pi(RPM)Q}{60(VI)} = \frac{2\pi[K_V(V-IR_m)]\left[K_q(I-I_o)\right]}{60(VI)} \tag{7-5}$$

The above equation is assuming K_q is in units of (N-m)/Amp and the K_V is in units of RPM/Volt. According to the above equations, efficiency losses of the electric motor can be approximated by the resistance in the motor wire (R_m) and the idle current (I_o).The efficiency of the motor can be also be represent by electrical work out over electrical work in:

$$\eta_m = \frac{P_{out}}{P_{in}} = \frac{(V-IR_m)(I-I_o)}{VI} \tag{7-6}$$

The difference in the two efficiency equations is unit conversion. As shown in Figure 7-2, there is a linear relationship between torque and RPM. The linear relationship between torque and RPM indicate that K_q should be function of K_V.

Since the constant K_V is easier to obtain than the constant K_q, it is convenient to know the conversion between the two constants. The typical empirical value of K_q is 1352.59 in-oz/(Amp*K_V) and K_V is in units of RPM/V. This value is found by simple unit conversion and assuming motor resistance and idle current are the only losses:

$$K_q = \frac{60}{2\pi(0.0706)K_V}$$

The 0.0706 is to convert from N-m to in-oz. The conversion of K_V to K_q using 1352 in-oz/(Amp*K_V) experimentally proved to be close, but 9% higher than the values obtained for the "custom" motor tested. The experimental K_q value proved to be 1240 in-oz/(Amp*K_V). It was assumed that the difference was due to other losses such as iron losses, bearing drag, inductive reactance (frequency dependent), and heat losses that are not included in the derived empirical equations above. Tests were conducted on the "custom" motor and the empirical data was fit to the experimental data (see Appendix F for tabulated data). Other motors were unable to be tested, due to instrumentation limitations. The results of the "custom" motor can be seen below:

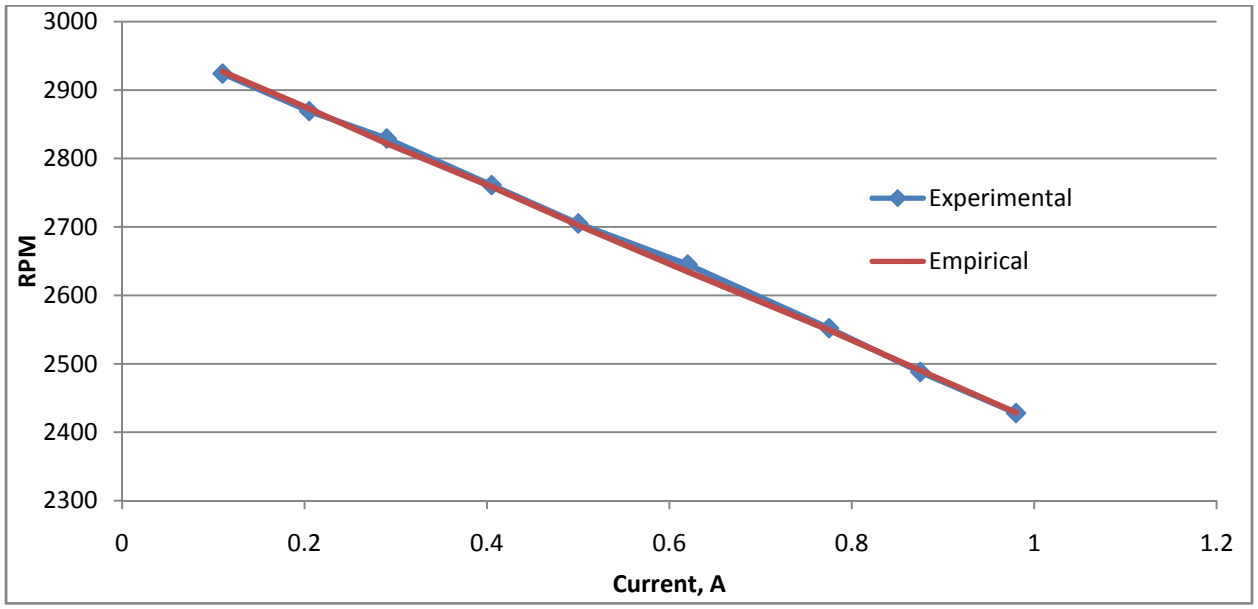

Figure 7-6: RPM as current increases (Experimental vs. Empirical of custom motor)

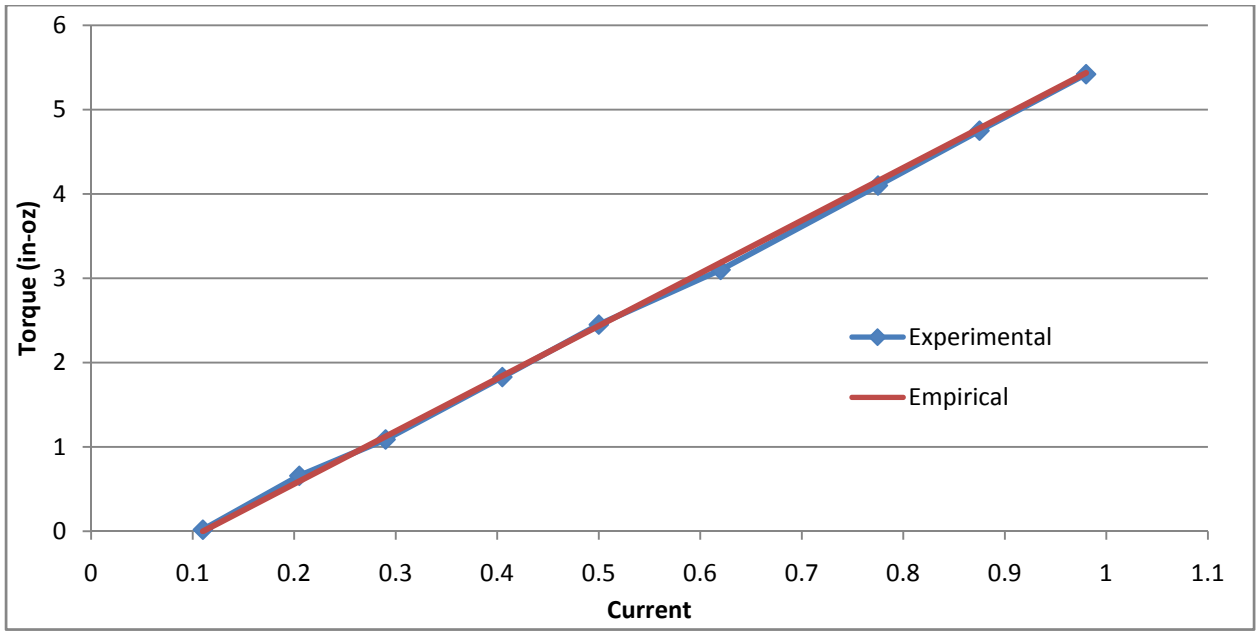

Figure 7-7: Torque as current increases (Experimental vs. Empirical of custom motor)

The difference between the "typical" empirical value used and the empirical value used to fit the "custom" motor (which is assumed to account for the extra losses) can be seen clearly in the efficiency curves below:

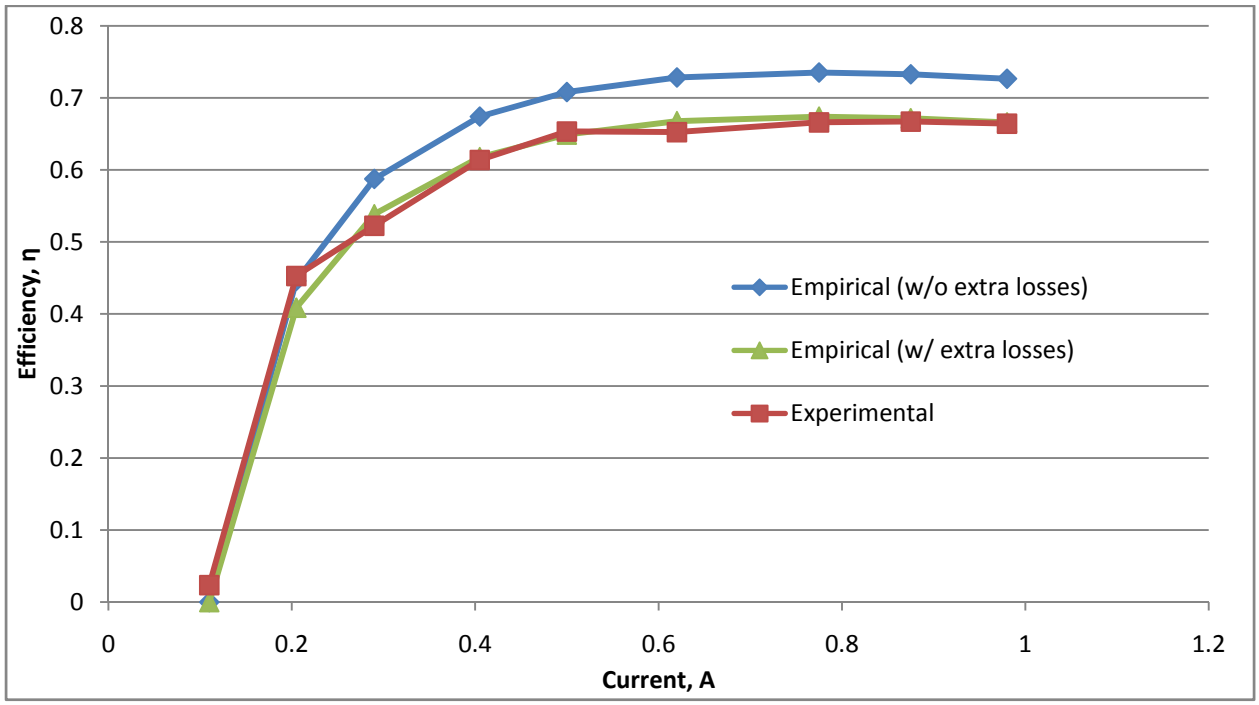

Figure 7-8: Efficiency as function of current for empirical, empirical including extra losses, and experimental (custom motor)

A list of motors with their respective K_V, I_o, and R_m can be created or found with a little bit of effort[32]; one was not included in this report, due to space. Some useful quantities that can be derived from the above empirical equations are the current at maximum power:

$$I_{P(max)} = \frac{V+R_m I_o}{2R_m} \tag{7-7}$$

The current at maximum efficiency:

$$I_{\eta(max)} = \sqrt{\frac{VI_o}{R_m}} \tag{7-8}$$

And the maximum efficiency:

$$\eta_{(max)} = \left(1 - \sqrt{\frac{I_o R_m}{V}}\right)^2 \tag{7-9}$$

These quantities are all derived from taking the derivative of each equation, setting it equal to zero and solving. Those derivations are not done here, but should be relatively straight forward. A figure of merit for a motor, usually in inch-ounces per root watt, can be used to describe a motors ability to produce torque as a function of heat:

$$K_m = \frac{K_q}{\sqrt{R_m}}$$

This value can be used to evaluate motors that may generate too much heat for a specific mission; this is especially useful if the motor is enclosed inside a vehicle.

Good rules of thumb by a motor enthusiast [31] include:

- Use at least, $\mathrm{I}_{\eta(\max)}$. If this is already too much power for your model, use a smaller motor.
- Never use more than $\mathrm{I}_{\mathrm{p(max)}}$. Otherwise, your motor will get too hot and the output power will drop.
- It is a good rule of thumb to use about 70-90% of $\mathrm{I}_{\mathrm{p(max)}}$.

Chapter 8 – Optimization of Propeller and Motor combination

Every propeller has a specific range of efficient operation. This range is dependent on the shape of the efficiency curve. The range of efficient operation is a combination of RPM and incoming flow velocity. The incoming flow velocity, for this analysis, is set to 2 m/s but in reality the flow seen by the propeller will be lower if the propeller is behind a vehicle. The deceleration of flow behind the body of the vehicle is due to separation and boundary layer effects. This non-uniform deceleration is lumped together as one fraction called the wake deduction fraction. This fraction will most likely be used in a more detailed analysis of vehicle performance, unless the propeller is placed in front of the vehicle, which is not the case for most marine vehicles. For this propulsion system optimization a uniform inflow velocity of 2 m/s is assumed to be seen by the propeller. The thrust required to get attain 2m/s by the vehicle is assumed to be 12N. These values are stated in the mission statement. If these values were not stated in the mission statement they could be obtained experimentally by tow tank testing the vehicle, running the vehicle with a propeller of known characteristics, or using theory (based on the shape of the vehicle). The coefficient of thrust is given in two forms. One form is dependent upon thrust and the other is dependent upon inflow velocity. The two equations combined can be seen below:

$$K_T = \frac{T}{\rho n^2 D^4} = K_T(J) = K_T(n, D, V_A)$$

The rotational speed, n, can be solved numerically to give a value of 44.1 RPS or 2646 RPM for the Octura 0977. At this speed the K_T has a value of 0.17 and the $10K_Q$ has a value of 0.27 resulting in an efficiency of 0.59. With the given Kq a torque of 0.146 N-m or 20.74 in-oz is required to generate the 12N of thrust. The efficiency of the propeller is on the left hand side of the peak efficiency, meaning a smaller efficiency slope and less efficiency variation if the advance ratio is off the predicted value. A couple of motors have been chosen to evaluate overall performance. The power source has an assumed battery pack voltage of 16V. Empirically derived values can be obtained using the motor constants:

Table 8: Motor Performance Characteristics

	Kv(RPM/V)	Io (A)	Rm(Ohm)	Weight (g)	I(Pmax)	I(η_{max})	η(max)
HP-Z2205-46	1200	0.42	0.245	29.4	32.86	5.24	0.85
HP-Z2209-32	910	0.55	0.181	42.5	44.47	6.97	0.85
HP-Z2213-24	850	0.6	0.135	53.8	59.56	8.43	0.86
Custom	198.5	0.11	2.77	59.2	2.94	0.76	0.75

The resultant empirical RPM and Torque values at max efficiency are:

Table 9: RPM and Torque at maximum efficiency

	RPM(ηmax)	Q(ηmax, in-oz)
HP-Z2205-46	17660.25	4.82
HP-Z2209-32	13411.52	8.47
HP-Z2213-24	12632.34	11.06
Custom	2758.11	3.99

From the above table it can be seen that the motors selected in this optimization do not meet the Octura 0977 propeller requirements. The custom motor meets the RPM requirement, but unfortunately doesn't meet the torque requirement. A second revision was used to evaluate the availability of a motor that could operate in this range. A list of 1460 brushless and brushed motors was used to evaluate if a motor is commercially available to operate in the Octura 0977 range at 16V. One motor out of the 1460 motors was able to operate below 3000 RPM when current is at maximum efficiency, but gives 4 times more torque than needed by the propeller. If we reduce the voltage input to the motor to 12V, 9 more motors appear to be within the RPM range. Unfortunately these motors still produce on the order of 3 to 4 times more torque than what is required. It is understood that many RC motors are designed for high RPM low torque applications and the larger motors are designed to spin the larger propellers at slow RPM, which apparently require much more torque than we need and weigh a lot more than desired.

Proposed solutions are: reduction gear for the higher spinning motors, going to a higher BAR propeller that can spin at higher RPM, increasing velocity of mission (RPM increases, Thrust increases, Torque increases, but the efficiency of the Octura 0977 propeller goes down), designing a custom motor that will operate at the design speed. A custom propeller would require a large investment to purchase and test as well as still require a motor that can spin slow enough to make the propeller efficient (meaning a custom motor or reduction gears as well). Of these proposed solutions the reduction gear and custom motor appear to be the easiest to obtain. The reduction gear is not desired due to losses in gears resistance, noise, and complexity. The custom motor requires more initial work and can't be replaced as easily as commercial reduction gears and motors. The custom motor in this analysis is a DLRK, 22mm in diameter with 15mm stator length with 30 turns and 30 gauge wire. Going to a larger motor with less turns, but larger wire should keep the Kv at about the same value, but decrease the resistance of the wire significantly, allowing for more current to be transferred. A proposed set of values at 16V are:

Theory	Kv (RPM/V)	Io (A)	Rm (Ohm)	Weight (g)	I (Pmax)	I (η_{max})	η (max)	RPM (ηmax)	Q(ηmax) (in-oz)
Custom2	200	0.3	0.25	80	24.15	3.79	0.85	2210.26	20.97

The above solution is estimated to be a DLRK, 30mm diameter 20 mm stator length with 25 turns and 25 gauge wire. This above solution has not been created or tested due to time.

Chapter 9 – Conclusions and Future Work

The objective of this thesis was to outline a method to propulsion selection for autonomous underwater vehicles depending on a mission specific scenario. The mission specific scenario required for this thesis was: an efficient propeller and motor combination that can propel a vehicle at 2 m/s. To travel at 2 m/s a thrust of 12N is required. The mission scenario helped to design guidelines for propeller selection and ultimately lead to selection of a commercially available efficient propeller. Motor selection guidelines were also developed using the mission statement. These guidelines lead to an estimated solution of the motor required to propel the vehicle.

9.1 - Results

A large design space was developed to examine propeller and motor combinations. The propeller design space was narrowed first, since propeller selection for this application was more limited than motor selection at this time. The propeller selected was an Octura 0977 and was tested in a wind-tunnel. The results of that wind tunnel test lead to characterization of non-dimensional propeller performance curves. These curves were used to give the motor requirements to power this propeller. The motor design space was also opened up to include many types of electric motor designs. The design space was narrowed to a brushless direct current (BLDC) outer rotor motor. Testing of four BLDC motors resulted in being able to predict motor performance of almost any DC motor. The four motors selected were not able to power the vehicle efficiently. A list of 1460 DC motors was used to evaluate the availability of a motor with the propeller's specifications and no suitable match was found. A motor that requires custom manufacturing or the aid of reduction gearing was proposed as solutions. A custom propeller was not suggested because it would require a large investment to purchase and test as well as still require a motor that can spin slow enough to make the propeller efficient (meaning a custom motor as well).

9.2 - Future Work

The intent of this paper was to show the process of motor propeller pairing. The implementation and testing of custom motors for a candidate propeller has not been tested and should be tested. Propeller testing requires the use of a reliable propeller test rig. The torque sensor on the propeller test rig should be modified to have a smaller range of torque to allow for more precise measurements. The tunnel that the propeller test rig was tested in will be removed soon and a new tunnel will take its place. Testing should be done in the new tunnel to remove the vibration due to the motor of the tunnel.

Works Cited

[1] G.T. Reader, "The Evolution of AUV Power Systems," 2002.

[2] P.K. Poole, "A systems approach to autonomous underwater vehicle (AUV) propulsion," 1996.

[3] J.G. Hawley, "A knowledge based aid for the selection of autonomous underwater vehicle (AUV) engergy systems," 1992.

[4] Stanway and Stefanov-Wagner, "Small-diameter ducted contrarotating propulsors for marine robots," 2006.

[5] Dr. Wanye Neu, "Propulsion_notes," 2003.

[6] Lewis, *Principles of Naval Architecture, Resistance, Propulsion, and Vibration*. Jersey City, NJ: The Society of Naval Architects and Marine Engineers, 2005, vol. II.

[7] D. Ray, P. Kinley M.M. Bernitsas, "Kt, Kq, and Efficiency Curves for the Wageningen B-Series Propellers," Ann Arbor, Michigan, May 1981.

[8] M.W.C. and P. Van Oosanen Oosterveld, "Further Computer-Analyzed Data of the Wageningen B-Screw Series," in *IV International Symposium on Ship Automation*, Genova, Italy, Nov. 1974.

[9] Dr. William Devenport. Aerospace and Ocean Engineering at Virginia Tech. [Online]. http://www.aoe.vt.edu/research/facilities/openjet.php

[10] Norval White Conner. (1937, July) Aerospace and Ocean Engineering at Virginia Tech. [Online]. http://www.aoe.vt.edu/~aborgolt/aoe3054/manual/app2/OpenJetTunnelArticle.pdf

[11] Dr. William Devenport. AOE 3054 Experimental Methods Course Manual. [Online]. http://www.aoe.vt.edu/~aborgolt/aoe3054/manual

[12] Wikipedia. [Online]. http://en.wikipedia.org/wiki/Pitot_tube

[13] "Fact Sheet No. 17 - Weather Observations," 2008.

[14] Dr. Sighard Hoerner, *Fluid Dynamic Drag*.: Hoerner Fluid Dynamics, 1993.

[15] Honeywell. [Online]. http://content.honeywell.com/sensing/sensotec/loadcell.asp?category=mini

[16] Vibrac Torque Test Systems. [Online]. http://www.vibrac.com

[17] All e RC. [Online]. http://www.allerc.com/

[19] Sensotec. [Online]. http://www.sensotec.com/pdf/ubp.pdf

[20] Wikipedia. [Online]. http://en.wikipedia.org/wiki/Analog-to-digital_converter

[21] MIT. [Online]. http://web.mit.edu/openprop/www/Welcome.html

[22] Justin E. Kerwin, *Hydrofoils and Propellers*., Jan 2001.

[23] Hsin-Lung Chung, "An Enhanced Propeller Design Program Based on Propeller Vortex Lattice Lifting Line Theory," 2007.

[24] Jessica Jacobson, "Using Single Propeller Performance Data to Predict Counter-Rotating Propeller Performance for a High Speed Autonomous Underwater Vehicle," Blacksburg, 2007.

[25] National Master. [Online]. www.nationmaster.com

[26] William H. Yeadon and Alan W. Yeadon, *Handbook of Small Electric Motors*. New York: McGraw-Hill, 2001.

[27] Christo van der Merwe. Home-Built Brushless Models. [Online]. http://www.bavaria-direct.co.za/models/motor_info.htm

[28] Brian Mulder. Go Brushless. [Online]. http://www.gobrushless.com/kb/index.php?title=Brushless_101_-_Chapter_3

[29] Aircraft World. [Online]. http://aircraft-world.com/prod_datasheets/hp/emeter/emeter.htm

[30] MIT. [Online]. http://lancet.mit.edu/motors/colorTS2.jpg

[31] Joachim Bergmeyer. (2003, February) RC Groups. [Online]. http://www.rcgroups.com/forums/printthread.php?t=185271

[32] Fly Brushless. [Online]. http://www.flybrushless.com/

Appendices

Appendix A – Tabulated Small, Medium, and Large efficiency, diameter, P/D

Small BAR				
RPM	Diameter(m)	J	Eff	P/D
4000	0.0765	0.392157	0.6523	0.6
3800	0.0785	0.40228	0.6582	0.61
3600	0.0805	0.414079	0.6642	0.62
3400	0.0825	0.427807	0.6705	0.63
3200	0.0855	0.438596	0.6772	0.64
3000	0.0885	0.451977	0.6842	0.65
2800	0.0915	0.468384	0.6914	0.67
2600	0.0945	0.4884	0.6991	0.69
2400	0.0985	0.507614	0.7071	0.71
2200	0.1015	0.537394	0.7153	0.74
2000	0.1015	0.591133	0.7197	0.82

Medium BAR				
RPM	Diameter(m)	J	Eff	P/D
4000	0.0715	0.41958	0.6125	0.67
3800	0.0735	0.429646	0.6184	0.67
3600	0.0755	0.441501	0.6245	0.68
3400	0.0775	0.455408	0.6309	0.7
3200	0.0805	0.465839	0.6376	0.7
3000	0.0825	0.484848	0.6447	0.72
2800	0.0855	0.501253	0.6522	0.74
2600	0.0885	0.521512	0.66	0.76
2400	0.0925	0.540541	0.6682	0.77
2200	0.0965	0.565238	0.677	0.8
2000	0.1015	0.591133	0.686	0.82

Large BAR				
RPM	Diameter(m)	J	Eff	P/D
4000	0.0675	0.444444	0.5717	0.73

3800	0.0695	0.454373	0.5775	0.74
3600	0.0715	0.4662	0.5836	0.75
3400	0.0735	0.480192	0.5901	0.76
3200	0.0755	0.496689	0.5968	0.78
3000	0.0785	0.509554	0.6039	0.81
2800	0.0805	0.532387	0.6114	0.81
2600	0.0835	0.552741	0.6193	0.83
2400	0.0875	0.571429	0.6277	0.84
2200	0.0915	0.596125	0.6365	0.86
2000	0.0955	0.628272	0.646	0.9

Appendix B – Uncertainty Analysis of Propeller Testing

Thrust Coefficient

$$K_T(\rho,n,D,T) := \frac{T}{\rho \cdot n^2 \cdot D^4}$$

$$\frac{d}{dT} K_T(\rho,n,D,T) \rightarrow \frac{1}{\rho \cdot n^2 \cdot D^4}$$

$$\frac{d}{d\rho} K_T(\rho,n,D,T) \rightarrow \frac{-T}{\rho^2 \cdot n^2 \cdot D^4}$$

$$\frac{d}{dn} K_T(\rho,n,D,T) \rightarrow (-2) \cdot \frac{T}{\rho \cdot n^3 \cdot D^4}$$

$$\frac{d}{dD} K_T(\rho,n,D,T) \rightarrow (-4) \cdot \frac{T}{\rho \cdot n^2 \cdot D^5}$$

Torque Coefficient

$$K_Q(\rho,n,D,Q) := \frac{Q}{\rho \cdot n^2 \cdot D^5}$$

$$\frac{d}{dQ} K_Q(\rho,n,D,Q) \rightarrow \frac{1}{\rho \cdot n^2 \cdot D^5}$$

$$\frac{d}{d\rho} K_Q(\rho,n,D,Q) \rightarrow \frac{-Q}{\rho^2 \cdot n^2 \cdot D^5}$$

$$\frac{d}{dn} K_Q(\rho,n,D,Q) \rightarrow (-2) \cdot \frac{Q}{\rho \cdot n^3 \cdot D^5}$$

$$\frac{d}{dD} K_Q(\rho,n,D,Q) \rightarrow (-5) \cdot \frac{Q}{\rho \cdot n^2 \cdot D^6}$$

Thrust Coefficient (Measured Terms)

$$K_T(P_o,R,n,D,T_o,Thrust) := \frac{Thrust}{\frac{P_o}{R \cdot T_o} \cdot n^2 \cdot D^4}$$

$$\frac{d}{dThrust} K_T(P_o,R,n,D,T_o,Thrust) \rightarrow \frac{1}{P_o} \cdot R \cdot \frac{T_o}{n^2 \cdot D^4}$$

$$\frac{d}{dP_o} K_T(P_o,R,n,D,T_o,Thrust) \rightarrow \frac{-Thrust}{P_o^2} \cdot R \cdot \frac{T_o}{n^2 \cdot D^4}$$

$$\frac{d}{dT_o} K_T(P_o,R,n,D,T_o,Thrust) \rightarrow \frac{Thrust}{P_o} \cdot \frac{R}{n^2 \cdot D^4}$$

$$\frac{d}{dn} K_T(P_o,R,n,D,T_o,Thrust) \rightarrow (-2) \cdot \frac{Thrust}{P_o} \cdot R \cdot \frac{T_o}{n^3 \cdot D^4}$$

$$\frac{d}{dD} K_T(P_o,R,n,D,T_o,Thrust) \rightarrow (-4) \cdot \frac{Thrust}{P_o} \cdot R \cdot \frac{T_o}{n^2 \cdot D^5}$$

Torque Coefficient (Measrued Terms)

$$K_Q(P_o,R,T,n,D,Q) := \frac{Q}{\frac{P_o}{R \cdot T} \cdot n^2 \cdot D^5}$$

$$\frac{d}{dQ} K_Q(P_o,R,T,n,D,Q) \rightarrow \frac{1}{P_o} \cdot R \cdot \frac{T}{n^2 \cdot D^5}$$

$$\frac{d}{dP_o} K_Q(P_o,R,T,n,D,Q) \rightarrow \frac{-Q}{P_o^2} \cdot R \cdot \frac{T}{n^2 \cdot D^5}$$

$$\frac{d}{dT} K_Q(P_o,R,T,n,D,Q) \rightarrow \frac{Q}{P_o} \cdot \frac{R}{n^2 \cdot D^5}$$

$$\frac{d}{dn} K_Q(P_o,R,T,n,D,Q) \rightarrow (-2) \cdot \frac{Q}{P_o} \cdot R \cdot \frac{T}{n^3 \cdot D^5}$$

$$\frac{d}{dD} K_Q(P_o,R,T,n,D,Q) \rightarrow (-5) \cdot \frac{Q}{P_o} \cdot R \cdot \frac{T}{n^2 \cdot D^6}$$

Advance Ratio

$$J(V_a,n,D) := \frac{V_a}{n \cdot D}$$

$$\frac{d}{dV_a} J(V_a,n,D) \rightarrow \frac{1}{n \cdot D}$$

$$\frac{d}{dn} J(V_a,n,D) \rightarrow \frac{-V_a}{n^2 \cdot D}$$

$$\frac{d}{dD} J(V_a,n,D) \rightarrow \frac{-V_a}{n \cdot D^2}$$

Advance Ratio (Measured Terms)

$$J(\Delta P,R,T_o,P_o,n,D) := \frac{\sqrt{\frac{2\Delta P \cdot R \cdot T_o}{P_o}}}{n \cdot D}$$

$$\frac{d}{d\Delta P} J(\Delta P,R,T_o,P_o,n,D) \rightarrow \frac{1}{2} \cdot \frac{2^{\frac{1}{2}}}{\left(\Delta P \cdot R \cdot \frac{T_o}{P_o}\right)^{\frac{1}{2}} \cdot n \cdot D} \cdot R \cdot \frac{T_o}{P_o}$$

$$\frac{d}{dP_o} J(\Delta P,R,T_o,P_o,n,D) \rightarrow \frac{-1}{2} \cdot \frac{2^{\frac{1}{2}}}{\left(\Delta P \cdot R \cdot \frac{T_o}{P_o}\right)^{\frac{1}{2}} \cdot n \cdot D} \cdot \Delta P \cdot R \cdot \frac{T_o}{P_o^2}$$

$$\frac{d}{dT_o} J(\Delta P,R,T_o,P_o,n,D) \rightarrow \frac{1}{2} \cdot \frac{2^{\frac{1}{2}}}{\left(\Delta P \cdot R \cdot \frac{T_o}{P_o}\right)^{\frac{1}{2}} \cdot n \cdot D} \cdot \Delta P \cdot \frac{R}{P_o}$$

$$\frac{d}{dn} J(\Delta P,R,T_o,P_o,n,D) \rightarrow \left(\frac{-1}{2}\right) \cdot \frac{\left(\Delta P \cdot R \cdot \frac{T_o}{P_o}\right)^{\frac{1}{2}}}{n^2 \cdot D}$$

$$\frac{d}{dD} J(\Delta P,R,T_o,P_o,n,D) \rightarrow \left(\frac{-1}{2}\right) \cdot \frac{\left(\Delta P \cdot R \cdot \frac{T_o}{P_o}\right)^{\frac{1}{2}}}{n \cdot D^2}$$

Efficiency (Measured terms)

$$\eta(\text{Thrust},\Delta P,R,T_o,P_o,Q,n) := \frac{\text{Thrust}}{Q \cdot n \cdot 2 \cdot \pi} \cdot \sqrt{\frac{2\Delta P \cdot R \cdot T_o}{P_o}}$$

$$\frac{d}{d\text{Thrust}} \eta(\text{Thrust},\Delta P,R,T_o,P_o,Q,n) \rightarrow \frac{1}{2 \cdot Q \cdot n \cdot \pi} \cdot 2^{\frac{1}{2}} \cdot \left(\Delta P \cdot R \cdot \frac{T_o}{P_o}\right)^{\frac{1}{2}}$$

$$\frac{d}{d\Delta P} \eta(\text{Thrust},\Delta P,R,T_o,P_o,Q,n) \rightarrow \frac{1}{4} \cdot \frac{\text{Thrust}}{Q \cdot n \cdot \pi} \cdot \frac{2^{\frac{1}{2}}}{\left(\Delta P \cdot R \cdot \frac{T_o}{P_o}\right)^{\frac{1}{2}}} \cdot R \cdot \frac{T_o}{P_o}$$

$$\frac{d}{dT_o} \eta(\text{Thrust},\Delta P,R,T_o,P_o,Q,n) \rightarrow \frac{1}{4} \cdot \frac{\text{Thrust}}{Q \cdot n \cdot \pi} \cdot \frac{2^{\frac{1}{2}}}{\left(\Delta P \cdot R \cdot \frac{T_o}{P_o}\right)^{\frac{1}{2}}} \cdot \Delta P \cdot \frac{R}{P_o}$$

$$\frac{d}{dP_o} \eta(\text{Thrust},\Delta P,R,T_o,P_o,Q,n) \rightarrow \frac{-1}{4} \cdot \frac{\text{Thrust}}{Q \cdot n \cdot \pi} \cdot \frac{2^{\frac{1}{2}}}{\left(\Delta P \cdot R \cdot \frac{T_o}{P_o}\right)^{\frac{1}{2}}} \cdot \Delta P \cdot R \cdot \frac{T_o}{P_o^2}$$

$$\frac{d}{dQ} \eta(\text{Thrust},\Delta P,R,T_o,P_o,Q,n) \rightarrow \frac{-1}{2} \cdot \frac{\text{Thrust}}{Q^2 \cdot n \cdot \pi} \cdot 2^{\frac{1}{2}} \cdot \left(\Delta P \cdot R \cdot \frac{T_o}{P_o}\right)^{\frac{1}{2}}$$

$$\frac{d}{dn} \eta(\text{Thrust},\Delta P,R,T_o,P_o,Q,n) \rightarrow \frac{-1}{2} \cdot \frac{\text{Thrust}}{Q \cdot n^2 \cdot \pi} \cdot 2^{\frac{1}{2}} \cdot \left(\Delta P \cdot R \cdot \frac{T_o}{P_o}\right)^{\frac{1}{2}}$$

Estimated Input Ranges/ Values/ Error

$R := 287 \quad \frac{J}{kg \cdot K}$

$n := 170 \quad RPS$ $\qquad \delta_n := \frac{1}{60} \quad RPS$

$D := .055118\,m$ $\qquad \delta_D := .000005 \quad m$

$P_o := 93010 \quad Pa$ $\qquad \delta_{Po} := 10 \quad pa$

$T_o := 290 \quad Kelvin$ $\qquad \delta_{To} := .1 \quad K$

$\Delta P_o := 20 \quad Pa$ $\qquad \delta_{\Delta Po} := \Delta P_o \cdot 1\%$ $\qquad \delta_{\Delta Po} = 0.2 \quad Pa$

$\rho := \frac{P_o}{R \cdot T_o}$

$J(\Delta P_o, R, T_o, P_o, n, D) = 0.639$

$J_1 := J(\Delta P_o, R, T_o, P_o, n, D)$

$Thrust := \left(0.1486 \cdot J_1^{\,3} - 0.2762 \cdot J_1^{\,2} - 0.2836 \cdot J_1 + 0.5001\right) \cdot \rho \cdot n^2 \cdot D^4$

$Q := \frac{\left(0.4171 \cdot J_1^{\,3} - 0.9068 \cdot J_1^{\,2} - 0.2116 \cdot J_1 + 0.9436\right) \cdot \rho \cdot n^2 \cdot D^5}{10}$

$\rho(P, T) := \frac{P}{R \cdot T}$ $\qquad U_{inf}(\Delta P, P, T) := \sqrt{\frac{2 \Delta P \cdot R \cdot T}{P}}$

$\rho(P_o, T_o) = 1.118 \quad \frac{kg}{m^3}$ $\qquad U_{inf}(\Delta P_o, P_o, T_o) = 5.983 \quad \frac{m}{s}$

$Thrust = 0.073 \quad N$ $\qquad Q = 8.993 \times 10^{-4} \quad N*m$

$\delta_{Thrust} := Thrust \cdot 1\%$ $\qquad \delta_Q := Q \cdot 1.5\%$

$\delta_{Thrust} = 7.306 \times 10^{-4}$ $\qquad \delta_Q = 1.349 \times 10^{-5}$ $\qquad \eta(Thrust, \Delta P_o, R, T_o, P_o, Q, n) = 0.455$

Ranges
Uinf =0:6 m/s
n = 60:160 RPS
D = 0.055:0.12 in

Z55 Case
Uinf = 5 m/s
n = 120 RPS
D = .055 in

$$X := \begin{pmatrix} \frac{d}{dP_o} J(\Delta P_o, R, T_c, P_o, n, D) & \frac{d}{dT_o} J(\Delta P_o, R, T_o, P_o, n, D) & \frac{d}{d\Delta P_o} J(\Delta P_o, R, T_c, P_o, n, D) & \frac{d}{dn} J(\Delta P_c, R, T_c, P_o, n, D) & \frac{d}{dD} J(\Delta P_o, R, T_c, P_o, n, D) & 0 & 0 \\ \frac{d}{dP_o} K_T(P_o, R, n, D, T_o, Thrust) & \frac{d}{dT_o} K_T(P_o, R, n, D, T_c, Thrust) & 0 & \frac{d}{dn} K_T(P_o, R, n, D, T_o, Thrust) & \frac{d}{dD} K_T(P_o, R, n, D, T_o, Thrust) & \frac{d}{dThrust} K_T(P_o, R, n, D, T_o, Thrust) & 0 \\ \frac{d}{dP_o} K_Q(P_o, R, T_o, n, D, Q) & \frac{d}{dT_o} K_Q(P_o, R, T_o, n, D, Q) & 0 & \frac{d}{dn} K_Q(P_o, R, T_o, n, D, Q) & \frac{d}{dD} K_Q(P_o, R, T_o, n, D, Q) & 0 & \frac{d}{dQ} K_Q(P_o, R, T_o, n, D, Q) \\ \frac{d}{dP_o} \eta(Thrust, \Delta P_o, R, T_o, P_o, Q, n) & \frac{d}{dT_o} \eta(Thrust, \Delta P_o, R, T_o, P_o, Q, n) & \frac{d}{d\Delta P_o} \eta(Thrust, \Delta P_o, R, T_o, P_o, Q, n) & \frac{d}{dn} \eta(Thrust, \Delta P_o, R, T_o, P_o, Q, n) & 0 & \frac{d}{dThrust} \eta(Thrust, \Delta P_o, R, T_o, P_o, Q, n) & \frac{d}{dQ} \eta(Thrust, \Delta P_o, R, T_o, P_o, Q, n) \end{pmatrix} \xrightarrow[float, 4]{\text{simplify}} \begin{pmatrix} -3432e\text{-}5 & .1101e\text{-}2 & .1596e\text{-}1 & -3756e\text{-}2 & -11.58 & 0 & 0 \\ -2635e\text{-}5 & 8452e\text{-}3 & 0 & -2884e\text{-}2 & -17.79 & 3.355 & 0 \\ -5885e\text{-}6 & 1888e\text{-}3 & 0 & -6440e\text{-}3 & -4.965 & 0 & 60.87 \\ -2446e\text{-}5 & 7845e\text{-}3 & .1135e\text{-}1 & -2577e\text{-}2 & 0 & 6.223 & -506.0 \end{pmatrix}$$

$$\delta_i := \begin{pmatrix} \delta_{Pc} \\ \delta_{Tc} \\ \delta_{\Delta Pc} \\ \delta_n \\ \delta_D \\ \delta_{Thrust} \\ \delta_Q \end{pmatrix} \qquad \delta_i = \begin{array}{|c|c|} \hline & 0 \\ \hline 0 & 10 \\ 1 & 0.1 \\ 2 & 0.2 \\ 3 & 0.017 \\ 4 & 5\cdot10^{-6} \\ 5 & 7.306\cdot10^{-4} \\ 6 & 1.349\cdot10^{-5} \\ \hline \end{array}$$

$$X = \begin{array}{|c|c|c|c|c|c|c|c|} \hline & 0 & 1 & 2 & 3 & 4 & 5 & 6 \\ \hline 0 & -3.432E\text{-}006 & 1.101E\text{-}003 & 15.96E\text{-}003 & -3.756E\text{-}003 & -11.58E+000 & 0E+000 & 0E+000 \\ 1 & -2.635E\text{-}006 & 845.2E\text{-}006 & 0E+000 & -2.884E\text{-}003 & -17.79E+000 & 3.355E+000 & 0E+000 \\ 2 & -588.5E\text{-}009 & 188.8E\text{-}006 & 0E+000 & -644E\text{-}006 & -4.966E+000 & 0E+000 & 60.87E+000 \\ 3 & -2.446E\text{-}006 & 784.5E\text{-}006 & 11.38E-003 & -2.677E-003 & 0E+000 & 6.228E+000 & -506E+000 \\ \hline \end{array}$$

$$\delta_J := \sqrt{\sum \left[\left[\left(X^T \right)^{\langle 0 \rangle} \cdot \delta_i \right]^2 \right]} \qquad \delta_{Kt} := \sqrt{\sum \left[\left[\left(X^T \right)^{\langle 1 \rangle} \cdot \delta_i \right]^2 \right]} \qquad \delta_{Kq} := \sqrt{\sum \left[\left[\left(X^T \right)^{\langle 2 \rangle} \cdot \delta_i \right]^2 \right]} \qquad \delta_\eta := \sqrt{\sum \left[\left[\left(X^T \right)^{\langle 3 \rangle} \cdot \delta_i \right]^2 \right]}$$

$$\left[\left(X^T \right)^{\langle 0 \rangle} \cdot \delta_i \right] = \begin{pmatrix} -3.432 \times 10^{-5} \\ 1.101 \times 10^{-4} \\ 3.192 \times 10^{-3} \\ -6.26 \times 10^{-5} \\ -5.79 \times 10^{-5} \\ 0 \\ 0 \end{pmatrix} \qquad \left[\left(X^T \right)^{\langle 1 \rangle} \cdot \delta_i \right] = \begin{pmatrix} -2.635 \times 10^{-5} \\ 8.452 \times 10^{-5} \\ 0 \\ -4.807 \times 10^{-5} \\ -8.895 \times 10^{-5} \\ 2.451 \times 10^{-3} \\ 0 \end{pmatrix}$$

$$\left[\left(X^T \right)^{\langle 2 \rangle} \cdot \delta_i \right] = \begin{pmatrix} -5.885 \times 10^{-6} \\ 1.888 \times 10^{-5} \\ 0 \\ -1.073 \times 10^{-5} \\ -2.483 \times 10^{-5} \\ 0 \\ 8.211 \times 10^{-4} \end{pmatrix} \qquad \left[\left(X^T \right)^{\langle 3 \rangle} \cdot \delta_i \right] = \begin{pmatrix} -2.446 \times 10^{-5} \\ 7.845 \times 10^{-5} \\ 2.276 \times 10^{-3} \\ -4.462 \times 10^{-5} \\ 0 \\ 4.55 \times 10^{-3} \\ -6.826 \times 10^{-3} \end{pmatrix}$$

$$\delta_J = 0.00320 \qquad \delta_{Kt} = 0.00245 \qquad \delta_{Kq} = 0.00082 \qquad \delta_\eta = 0.009$$

$$\frac{\delta_J}{J(\Delta P_c, R, T_c, P_o, n, D)} = 5.004 \times 10^{-3} \qquad \frac{\delta_{Kt}}{K_T(P_o, R, n, D, T_o, Thrust)} = 0.01 \qquad \frac{\delta_{Kq}}{K_Q(P_o, R, T_o, n, D, Q)} = 0.015 \qquad \frac{\delta_\eta}{\eta(Thrust, \Delta P_o, R, T_c, P_o, Q, n)} = 0.019$$

Appendix C – Expanded Blade Area of Octura 0977 and Octura 1462

Octura 0977 Expanded Area		
Left(mm)	Right(mm)	Rad(mm)
-10.04	9.02	0
-10.5	11.79	3
-10.98	14.18	6
-11.77	15.49	8.9
-11.97	15.52	11.8
-12.16	15.5	14.4
-12.43	15.28	17.4
-12.63	14.69	20.2
-12.22	13.5	23
-11	11.98	25.5
-9.31	9.85	28.3
-6.86	6.72	30.65
0	0	33
Octura 1462 Expanded Area		
Left(mm)	Right(mm)	Rad(mm)
11.28	-9.03	0
15.77	-11.86	2.9
18.43	-14	5.5
19.17	-16.24	8.5
18.51	-18.75	11.8
16.22	-20.24	15.1
11.27	-20.32	18.6
8.86	-19.28	20.6
0.91	-16	24.2
-8.41	-8.41	25.5

Appendix D - Motor performance values as torque increases (Custom motor)

PWM	V	I	RPM	Torque (in-oz)	Pin (W)	Pout (W)	Eff
8.75	15.26	0.12	2879	0.045	1.8312	0.096	0.052
	15.25	0.14	2868	0.142	2.135	0.301	0.141
	15.25	0.17	2834	0.375	2.5925	0.786	0.303
	15.25	0.2	2805	0.577	3.05	1.197	0.392
	15.25	0.23	2782	0.782	3.5075	1.609	0.459
	15.23	0.29	2730	1.18	4.4167	2.382	0.539
	15.23	0.33	2698	1.49	5.0259	2.973	0.591
	15.23	0.4	2660	1.88	6.092	3.698	0.607
	15.22	0.49	2609	2.45	7.4578	4.727	0.634
	15.22	0.53	2573	2.826	8.0666	5.377	0.667
	15.22	0.62	2535	3.18	9.4364	5.961	0.632
	15.2	0.67	2501	3.54	10.184	6.547	0.643
	15.18	0.69	2467	3.94	10.4742	7.188	0.686
	15.18	0.75	2440	4.25	11.385	7.668	0.674
	15.16	0.81	2380	4.9	12.2796	8.624	0.702
PWM							
7.5	15.22	0.11	2613	0.09	1.6742	0.174	0.104
	15.23	0.12	2551	0.155	1.8276	0.292	0.160
	15.22	0.15	2343	0.504	2.283	0.873	0.382
	15.22	0.17	2259	0.652	2.5874	1.089	0.421
	15.22	0.19	2098	0.86	2.8918	1.334	0.461
	15.22	0.21	2064	0.963	3.1962	1.470	0.460
	15.22	0.22	1940	1.2	3.3484	1.722	0.514
	15.22	0.25	1785	1.57	3.805	2.072	0.545
	15.2	0.29	1643	2	4.408	2.430	0.551
	15.2	0.33	1540	2.5	5.016	2.847	0.568
	15.2	0.38	1479	3.05	5.776	3.336	0.578
	15.2	0.43	1442	3.47	6.536	3.700	0.566
	15.18	0.47	1404	3.9	7.1346	4.049	0.568
	15.18	0.57	1216	5	8.6526	4.496	0.520
	15.16	0.645	1141	5.8	9.7782	4.894	0.500
PWM							
6.4	15.2	0.09	2070	0.101	1.368	0.155	0.113
	15.2	0.14	1333	0.807	2.128	0.795	0.374
	15.2	0.21	735	2.313	3.192	1.257	0.394

Appendix E – Motor performance values as torque increases (Hyperion Z2213-24)

PWM	V	A	RPM	Q(in-oz)	Pin(W)	Pout(W)	Eff
5.9	15.07	0.58	8080	0.097	8.7406	0.579578	0.066309
	15.06	0.68	7160	0.435	10.2408	2.303196	0.224904
	15.06	0.78	6200	0.795	11.7468	3.644916	0.31029
	15.04	0.86	5255	1.22	12.9344	4.740905	0.366535
	15.02	0.95	4550	1.575	14.269	5.299326	0.371387
	15	1.08	3280	2.425	16.2	5.881854	0.363077
	14.99	1.15	2750	2.83	17.2385	5.755033	0.333848
	14.99	1.2	2100	3.59	17.988	5.574968	0.309927
	14.97	1.31	1320	4.69	19.6107	4.577996	0.233444
	14.97	1.35	1030	5.27	20.2095	4.013992	0.198619
PWM							
5.7	15.04	0.41	6193	0.082	6.1664	0.375529	0.060899
	15.02	0.46	5450	0.3	6.9092	1.209056	0.174992
	15.02	0.53	3854	0.808	7.9606	2.302776	0.289272
	15.02	0.59	2635	1.388	8.8618	2.704573	0.305195
	15	0.67	1600	2.22	10.05	2.626646	0.261358
	15	0.685	690	2.71	10.275	1.382761	0.134575

Appendix F – Experimental and Empirical data from "custom" motor

V	I	Q(in-oz)	RPM
15.06	0	0	0
15.05	0.11	0.018	2924
15.04	0.205	0.658	2869
15.02	0.29	1.088	2829
15.02	0.405	1.829	2761
15	0.5	2.45	2705
14.99	0.62	3.1	2645
14.99	0.775	4.1	2552
14.97	0.875	4.75	2488
14.95	0.98	5.42	2428

Empirical Q(in-oz)	Empirical RPM
0	0
0	2926.942
0.593451	2872.722
1.124433	2822.015
1.842821	2758.783
2.436272	2702.578
3.185894	2634.611
4.154156	2549.385
4.778841	2490.431
5.434761	2428.727